

Université Fédérale



Toulouse Midi-Pyrénées

# THÈSE

en vue de l'obtention du

## DOCTORAT DE L'UNIVERSITÉ DE TOULOUSE

*délivré par*

*IMT – École Nationale Supérieure des Mines d'Albi-Carmaux*

*En cotutelle internationale avec l'École Polytechnique de l'Université de Sao Paulo*

---

**présentée et soutenue par**

**Marcio Wagner Batista dos SANTOS**

**le 09 octobre 2017**

INVESTIGATION OF THE MECHANICAL BEHAVIOUR AND  
MICROSTRUCTURE EVOLUTION OF TITANIUM ALLOYS UNDER  
SUPERPLASTIC AND HOT FORMING CONDITIONS

---

**École doctorale et discipline ou spécialité :**

ED MEGEP : École Doctorale Mécanique, Énergétique, Génie civil & Procédés

**Unité de recherche :**

Institut Clément Ader (ICA), UMR CNRS 5312, Mines Albi

**Directeur(s) de Thèse :**

Mr. Gilmar Ferreira BATALHA, Professeur, USP, Brésil

Mr. Gérard BERNHART, Professeur, IMT Mines Albi

**Autres membres du jury :**

Mr. Jean-Jacques BLANDIN, Directeur de recherche CNRS, INP Grenoble, France (*Rapporteur*)

Mr. Luciano Pessanha MOREIRA, Professeur, UFF, Brésil (*Rapporteur*)

M<sup>me</sup>. Maria H. ROBERT, Professeur, UNICAMP, Brésil (*Examinatrice*)

Mr. Vincent VELAY, Maître Assistant, IMT Mines Albi, (*Encadrant*)



MARCIO WAGNER BATISTA DOS SANTOS

**INVESTIGATION OF THE MECHANICAL BEHAVIOUR AND MICROSTRUCTURE  
EVOLUTION OF TITANIUM ALLOYS UNDER SUPERPLASTIC AND HOT  
FORMING CONDITIONS**

**São Paulo  
2017**

**MARCIO WAGNER BATISTA DOS SANTOS**

**Investigation of the mechanical behaviour and microstructure evolution of  
Titanium alloys under superplastic and hot forming conditions**

Thesis Submitted to the Faculty of the  
Graduate School of Sao Paulo University  
and IMT - École des Mines d'Albi-Carmaux  
in partial fulfilment of the requirements for  
the degree of Doctor of science in  
Mechanical Engineering

Advisor: Prof. Dr. Gilmar Ferreira Batalha.

Co-Advisor: Prof. Dr. Gérard Bernhart

**São Paulo  
2017**

**MARCIO WAGNER BATISTA DOS SANTOS**

**Investigation of the mechanical behaviour and microstructure evolution of  
Titanium alloys under superplastic and hot forming conditions**

Thesis Submitted to the Faculty of the  
Graduate School of Sao Paulo University  
and IMT - École des Mines d'Albi-Carmaux  
in partial fulfilment of the requirements for  
the degree of Doctor of science in  
Mechanical Engineering

Graduate program in Mechanical  
Engineering

Advisor: Prof. Dr. Gilmar Ferreira Batalha.

Co-Advisor: Prof. Dr. Gérard Bernhart

**São Paulo  
2017**

Este exemplar foi revisado e alterado em relação à versão original, sob responsabilidade única do autor e com anuência de seu orientador.

São Paulo, 11 de dezembro de 2017

Assinatura do autor: Marcio Wagner B. Santos

Assinatura do orientador: Gilmar Ferreira Batalha

### Catologação-na-publicação

Santos, Marcio Wagner Batista dos

Investigation of the mechanical behaviour and microstructure evolution of titanium alloys under superplastic and hot forming conditions. / M. W. B.

Santos -- versão corr. -- São Paulo, 2017.

149 p.

Tese (Doutorado) - Escola Politécnica da Universidade de São Paulo.  
Departamento de Engenharia Mecatrônica e de Sistemas Mecânicos.

1.Conformação mecânica 2.Processo de fabricação 3.Titânio  
4.Comportamento mecânico 5.Evolução microestrutural I.Universidade de São Paulo. Escola Politécnica. Departamento de Engenharia Mecatrônica e de Sistemas Mecânicos II.t.

To my parents, Maria José and Marcelino Pedro, my family, and Helenice Menezes.

## ACKNOWLEDGEMENTS

First all, I would like to express my sincere gratitude to my advisors Prof. Dr. Gilmar Batalha and Prof. Dr. Gérard Bernhart

I am also grateful to the following École des Mines d'Albi-Carmaux staff: Mr. Vincent Velay and Mrs. Vanessa Vidal for their unfailing support and assistance at the Institut Clément Ader (ICA) for funding the PhD research.

I very much acknowledge Hiroki MATSUMOTO, Associate Professor at faculty Engineering of Kagawa University in Japan, for conducting a part of the tensile tests used in the present research work.

A very special gratitude goes out to all down at CAPES Foundation and “Ciência Sem Fronteira” Found for helping and providing the funding for that work.

With a special mention to Erick Petta Marinho, Felipe Toloczko, Adalto de Farias (USP) and Serge Tovar (ICA), the pilot plant team, also CNPEM and USP in general. It was fantastic to have the opportunity to work majority of my research in your facilities. What a cracking place to work!

And finally, last but by no means least, also to everyone in the impact hub; it was great sharing laboratory with all of you during almost five years.

Thanks for all your encouragement!

Merci à tous et toutes pour vos encouragements!

Muito obrigado a todos pelo incentivo!

## ABSTRACT

This thesis was developed in the frame of a Brazil-France cooperation agreement between the École des Mines d'Albi-Carmaux and the Polytechnic School of Engineering of the University of Sao Paulo (EPUSP). It aims to contribute to the study of the mechanical behaviour of Ti6Al4V alloys especially in terms of superplastic forming. The general objective of this research is to develop non-conventional forming processes for new titanium alloys applied to aerospace components. Therefore, in accordance of the equipment's available in the two groups, the work will be conducted either at the Ecole des Mines d'Albi-Carmaux and either at EPUSP. This thesis aims to answer questions such as what are the implications in relation to the microstructural and mechanical behaviour of these alloys during superplastic and hot forming in order to establish a behaviour law for these alloys based on titanium. This requires a good knowledge of the properties of materials used in the superplastic and hot forming domain to control the parameters governing the phenomenon of superplasticity or high temperature plasticity. For this, a testing strategy and characterization methodology of those new titanium alloys was developed. The tests include high temperature uniaxial tensile tests on several Ti6Al4V alloys showing different initial grain sizes. Special focus was made on the microstructural evolution prior to testing (i.e. during specimen temperature increase and stabilization) and during testing. Testing range was chosen to cover the hot forming and superplastic deformation domain. Grain growth is depending on alloy initial microstructures but also on the duration of the test at testing temperature (static growth) and testing strain rate (dynamic growth). After testing microstructural evolutions of the alloys will be observed by optical micrograph or SEM and results are used to increase behaviour model accuracy. Advanced unified behaviour models were introduced in order to cover the whole strain rate and temperature range: kinematic hardening, strain rate sensitive and grain growth features are included in the model. In order to get validation of the behaviour model, it was introduced in ABAQUSR numerical simulation code and model predictions (especially macroscopic deformation and local grain growth) were compared, for one of the material investigated, to axisymmetric inflation forming tests of sheet metal parts, also known as bulge test. To obtain a simple control cycle, tests performed at IPT/LEL laboratory in San José Dos Campos in Brazil were operated with a constant strain rate. Results show a very good correlation with predictions and allows to conclude on an accuracy of the behaviour models of the titanium alloys in industrial forming conditions.

**Keywords:** Hot forming. Superplasticity. Superplastic forming. Microstructural evolution. Behavioural modelling.

## RÉSUMÉ

Cette thèse s'est déroulée dans le cadre d'une cotutelle internationale entre l'IMT - École des Mines d'Albi-Carmaux et l'École Polytechnique de l'Université de Sao Paulo (EPUSP). Elle a pour but de contribuer à l'étude du comportement mécanique des alliages de titane Ti6Al4V, et plus spécialement dans le domaine du formage superplastique et du formage à chaud. L'objectif général de ce doctorat est de contribuer au développement de procédés de formages non conventionnels des alliages de titane pour applications aéronautiques. C'est pourquoi, en fonction des équipements disponibles sur les deux sites, les travaux de recherche se sont déroulés soit à l'École des Mines soit à l'EPUSP. Cette thèse adresse la problématique scientifique des interactions entre le comportement mécanique dans le domaine du formage superplastique et de formage à chaud d'une part et la microstructure initiale et son évolution dans le domaine de sollicitation d'autre part. Pour cela une stratégie d'essais et de caractérisation a été développée et suivie. Les essais incluent des essais mécaniques uniaxiaux à haute température sur différents alliages Ti6Al4V présentant des microstructures initiales différentes (taille de grain 0,5; 3,0 et 4,9  $\mu\text{m}$ ). Une attention particulière a été portée à l'évolution microstructurale avant essai - c'est-à-dire durant sa montée en température et la stabilisation thermique de l'échantillon – et durant l'essai. Les conditions d'essai ont été choisies de façon à couvrir le domaine du formage à chaud et du formage superplastique, température de 700 °C à 950 °C et vitesse de déformation entre  $10^{-1} \text{ s}^{-1}$  et  $10^{-4} \text{ s}^{-1}$ . La croissance de grain dépend de la microstructure initiale mais aussi de la durée de l'essai en température (croissance statique) et de la vitesse de déformation (croissance dynamique). Afin d'améliorer la validité du modèle des observations microstructurales de taille de grain sont effectués après les essais mécaniques par micrographie optique et Microscope Electronique à Balayage. Un modèle de comportement unifié a été introduit de façon à être capable de couvrir toute la plage de température et de vitesse de déformation : écrouissage cinématique non linéaire, sensibilité à la vitesse de déformation et loi de croissance de la taille des grains sont inclus dans le modèle. Afin de pouvoir valider le modèle, il a été introduit dans le code de simulation ABAQUS®. Les résultats des simulations (en particulier déformation macroscopique et taille de grain locale) ont été comparés, pour l'un des matériaux de l'étude, aux résultats d'un essai de gonflage axisymétrique de tôle. Pour obtenir un cycle de contrôle simple, les essais effectués au laboratoire de l'IPT/LEL à Sao José dos Campos au Brésil ont été opérés à vitesse de déformation constante. Les résultats montrent une très bonne corrélation avec les prédictions et permettent de conclure à une validation du modèle de comportement développé dans la thèse dans des conditions industrielles de formage de l'alliage de titane.

**Mots-clés:** formage à chaud, formage superplastique, microstructure, croissance de grain, modèle de comportement

## RESUMO

Esta tese desenvolvida dentro do acordo de cooperação internacional celebrado entre a Escola Politécnica da Universidade de São Paulo (EPUSP) e a École des Mines d'Albi-Carmaux tem como tema principal a análise da influência da evolução microestrutural sobre o comportamento mecânico de chapa de liga de titânio - Ti-6Al-4V sob condições superplásticas e trabalho a quente. O objetivo desta pesquisa é contribuir para o desenvolvimento de processos de conformação não convencional de chapas de ligas a base de titânio utilizadas na manufatura de componentes metálicos. Como objetivo específico, estabelecer uma correlação entre comportamento mecânico e a mudança microestrutural a partir de três tipos de ligas com diferentes tamanhos de grão iniciais (0.5, 3.0 e 4.9  $\mu\text{m}$ ). Os testes foram realizados na faixa de temperatura de 700 a 950 °C combinados às taxas de deformação na faixa de  $10^{-1} \text{ s}^{-1}$  a  $10^{-4} \text{ s}^{-1}$ . Para a metodologia, estabeleceu-se uma estratégia de ensaios mecânicos capaz de testar as hipóteses sobre o comportamento do material formuladas no início desta pesquisa. Em seguida, os ensaios mecânicos foram divididos em três partes. Na primeira, utilizou-se um simulador termomecânico modelo Gleeble 3800 para os ensaios a quente variando-se a taxa de deformação ( $\dot{\epsilon}$ ) entre  $10^{-1} \text{ s}^{-1}$  a  $10^{-3} \text{ s}^{-1}$  e temperaturas da ordem de 700 °C a 850 °C. Na segunda parte dos testes, priorizou-se taxas de deformação mais lentas ( $10^{-2} \text{ s}^{-1}$  –  $10^{-4} \text{ s}^{-1}$ ) e temperaturas mais elevadas (800 °C – 950 °C) objetivando atingir as deformações superplásticas do material, nesta etapa utilizou-se como equipamento uma máquina de tração modelo MTS 50kN com câmara de aquecimento acoplada. A terceira parte dos ensaios experimentais envolveu a conformação na condição superplástica por pressão hidrostática (Bulge test) realizadas no LEL-IPT de São José dos Campos. A partir da análise dos dados experimentais levantou-se os parâmetros introduzidos no modelo numérico de comportamento mecânico baseado na evolução da microestrutura da chapa testada permitindo a calibração do modelo numérico a partir das equações constituintes e finalmente introduzido no software de elementos finitos (ABAQUS 6.12) e construído a simulação numérica da conformação superplástica por pressão hidrostática. Os principais resultados indicaram uma forte correlação entre microestrutura inicial da conformação superplástica e a quente de onde se pode observar que tanto menor a microestrutura inicial maior será a quantidade do crescimento de grão. Os resultados da conformação superplástica de expansão multiaxial do domo hemisférico foram, então, comparados à simulação numérica permitindo confrontar os dados do modelo numérico do comportamento mecânico com a lei de comportamento estudada, o que possibilitou um melhor entendimento dos mecanismos da conformação plástica em condições de superplasticidade e também de trabalho a quente do material.

**Palavras-chave:** Conformação a quente. Conformação superplástica. Microestrutura modelo de comportamento.

## LIST OF FIGURES

Figure 1-1 - Titanium alloys at domains applications.....	3
Figure 1-2 - Resumed flowchart of the experimental test and theoretical modelling approach. ....	5
Figure 2-1 – Allotropic transformation between body centred cubic - bcc $\beta$ and hexagonal compact - hcp $\alpha$ . The stacking A and B are representing by cubic lattice in red and blue (REVIL-BAUDARD, 2010). ....	10
Figure 2-2 The Ti-Al phase diagram (Adapted from SURAND, 2013) .....	15
Figure 2-3 – The Ti-V phase diagram (Adapted from SURAND, 2013).....	15
Figure 2-4 Three basic microstructure types in Ti-6Al-4V: a) lamellar; b) bimodal and c) equiaxed. Adapted From (DONACHIE, 2000). ....	16
Figure 2-5 - The microstructure of Ti-6Al-4V for different cooling processes adapted from Donachie (2000).....	17
Figure 2-6 - Time-Temperature-Transformation (TTT) diagram for Ti-6Al-4V. The alloy was solution annealed at 1020 °C, and quenched to a given temperature where the transformation was observed (DONACHIE, 2000). ....	18
Figure 2-7 Ternary phase diagram, adapted from (BABU, 2008) .....	19
Figure 2-8 - Tensile specimens in superplastic state for polycrystalline materials: a) Pearson's famous test of a Bi-Sn alloy that undergone 1950 %. b) The structure extruded of titanium-lead eutectic alloy after superplastic strain of nearly 50% showing grain boundary offset (arrowed) (PEARSON, 1934). ....	23
Figure 2-9 Some components based on titanium alloy: (a) automobile parts (b) prosthesis (c) blow test adapted from (Adapted from Bonet et al. 2006) .....	23
Figure 2-10 – Logarithmic plot of the dependence stress and strain rate for material with and without superplastic abilities (HAMILTON, 1984). ....	26
Figure 2-11 The region different deformation types adapted from Rhaipu (2000). ....	27

Figure 2-12 - Microstructure and texture evolution during strain increase (CHANDRA, 2002). .....	28
Figure 2-13 – True stress-true plastic strain curves of Ti-6Al-4V flat specimens tested between 750 °C and 950 °C and a strain of $5 \cdot 10^{-4} \text{ s}^{-1}$ (VANDERHASTEN, 2008).....	29
Figure 2-14 – True stress-true plastic strain of Ti-6Al-4V flat specimens tested at 800 °C and at strain rate between $5 \cdot 10^{-2} \text{ s}^{-1}$ and $5 \cdot 10^{-4} \text{ s}^{-1}$ (VANDERHASTEN, 2008) ...	30
Figure 2-15 (a) Conventionally fabricated ‘old design’ and (b) SPF Ti-6Al-4V new design first superplastic formed commercial titanium application (1981) (Adapted from Barnes, 2007).....	33
Figure 2-16 Evolution of $m$ with respect to strain rate and testing temperature (Aksenov, S.; Chumachenko, E.; Logashima 2012) .....	39
Figure 2-17 - Stepped strain test and determination of strain-rate sensitivity index ( $m$ ) value (COMLEY, 2007c). .....	39
Figure 3-1 - Grain Size Starting microstructure: 0.5 $\mu\text{m}$ ultra-fined-grained (a); fined-grain 3.0 $\mu\text{m}$ and (b) and fined-grain 4.9 $\mu\text{m}$ (c).....	41
Figure 3-2: Technical draw of specimen for thermomechanical test (a) and machined specimen aspect (b) .....	42
Figure 3-3 – Specimen for superplastic test at high temperature: and specimen technical draw (a) machined specimen (a).....	42
Figure 3-4: Gleeble 3800 MCU for tensile test – (LNLS- Brazil courtesy) .....	43
Figure 3-5 – Thermal cycle for tensile test planning with values for strain rate thermomechanical parameters for testing time vs temperature and sample specimen. ....	44
Figure 3-6: Setup for uniaxial tensile test at Gleeble® 3800: welder machine (a); Thermocouple wire type S (Platinum (–) vs. Platinum 10% Rhodium (+)) (b); the specimen position in detail (c) and chamber test; test execution.....	45
Figure 3-7: MTS 50 kN machine with furnace equipped used at superplastic test. ....	47
Figure 3-8 – Nabertherm® furnace using in annealing tests. ....	49

Figure 3-9 – Thermal cycle of the heat treatment named “static test” .....	49
Figure 3-10 - SimpliMet 3000 Automatic Mounting Press Buehler© machine (a). circular saw model IsoMet 5000 Linear Precision Saw (b). .....	50
Figure 4-1 - The curves obtained at high strain rate are more noisy, due to the high forces involved compared to the testing machine cell capacity. ....	53
Figure 4-2 - Variation of elongation with initial strain rate at different temperatures for $10^{-1} \text{ s}^{-1}$ strain rate. ....	54
Figure 4-3 – The specimen for thermomechanical test and (a) the true stress-strain curves obtained via the uniaxial tensile tests (b) .....	54
Figure 4-4 – Tensile test stress-strain curves at 850 °C and a strain rate from $10^{-3} \text{ s}^{-1}$ to $10^{-1} \text{ s}^{-1}$ . ....	55
Figure 4-5 – Tensile test stress-strain curves at 950 °C and strain rate from $10^{-3} \text{ s}^{-1}$ to $10^{-1} \text{ s}^{-1}$ . ....	56
Figure 4-6 – Microstructure after Gleeble thermomechanical deformation process at 700 °C and 850 °C for a strain rate from $10^{-3} \text{ s}^{-1}$ to $10^{-1} \text{ s}^{-1}$ . Two magnifications: 2000x and 5000x. ....	57
Figure 4-7 – Microstructure with selected area of $\alpha$ -phase and $\beta$ -phase sample tested at 950 °C – strain rate: $10^{-3} \text{ s}^{-1}$ . ....	58
Figure 4-8- True strain-stress curves for the same temperature level and two different grain sizes: 4.9 (a) and 0.5 (b) $\mu\text{m}$ . ....	59
Figure 4-9– Mechanical behaviour at 750: initial microstructure 0.5 $\mu\text{m}$ a) and initial microstructure 3.0 $\mu\text{m}$ b) .....	60
Figure 4-10 – Mechanical behaviour for initial microstructure 3.0 $\mu\text{m}$ and strain rate $10^{-2} \text{ s}^{-1}$ .....	61
Figure 4-11- The micrographics show dynamic grain growth evolution for tensile tests at temperature range from 800 °C to 950°C and strain rate from $10^{-2} \text{ s}^{-1}$ to $10^{-4} \text{ s}^{-1}$ for an initial grain size of 4.9 $\mu\text{m}$ . ....	62

Figure 4-12- FEGSEM BSE mode micrographs of samples heat treated at 800°C(a,c,e) and 850°C (b,d,f) and 870 °C water quenched (a,b), 950 °C cooled in air (c,d) and cooled in furnace (e,f).....	64
Figure 4-13 - Measurements of the static grain growth for different heat-treating times.....	65
Figure 4-14 – Grain growth evolution observed by SEM micrographs (BSE mode) in the case of the static tests at T =840 1C and several temperature exposure times t =1000 s (a), t =5000 s (b), t =10 000 s (c) and t =30 000 s (d) (VELAY et al., 2016).	66
Figure 5-1 - Dual-phase polycrystalline model based on the self-consistent relation (DANG; CHANDRA, 1998).....	67
Figure 5-2 - Identification of the coarsening rate constants based on the values provided by Semiatin et al. at 775 °C and 815 °C and extrapolation from 700 °C to 920 °C (adapted from Semiatin & Sargent (2010)).....	70
Figure 5-3 - Identification of the coarsening rate constants based on the values provided by (SEMIATIN et al., 2010) at 775 °C and 815 °C and $\epsilon=10^{-4} \text{ s}^{-1}$ ; $10^{-3} \text{ s}^{-1}$ and extrapolation from 700 °C to 920 °C.....	71
Figure 5-4 - Comparison of computed grain growth-time (a,c) and computed grain growth-strain (b,d) curves using the evolution law identified with the coarsening rate constants by Semiatin et al and experimental measurements performed in the present work at 920 °C and $d_0= 3\mu\text{m}$ (a,b); at 800 °C and $d_0= 4.9 \mu\text{m}$ (c,d).....	73
Figure 5-5 - Computed true strain - true stress data vs Experimental results at a temperature of 700 °C and initial grain size of $d_0=0.5 \mu\text{m}$ (a) and $4.9 \mu\text{m}$ (b).....	78
Figure 5-6 - Computed Strain-Stress data vs Experimental: results at a temperature of 840 °C and initial grain size of $d_0=0.5 \mu\text{m}$ .....	79
Figure 5-7 - Computed Stress-strain data vs Experimental results at a temperature of 840 °C and initial grain size of $d_0=3.0 \mu\text{m}$ .....	79
Figure 5-8 - Computed Strain-Stress data vs Experimental results at a temperature of 840 °C and initial grain size of $d_0=4.9 \mu\text{m}$ .....	80
Figure 6-1 – Ti-6Al-4V sheet Blank .....	82

Figure 6-2 – IPT Lightweight Structures Laboratory’s superplastic forming machine	83
Figure 6-3 – Blow forming bulge testing tooling parts: bottom-die (a) and top die (b)	83
Figure 6-4 – Schematic superplastic press and forming process .....	84
Figure 6-5 – Typical thermal cycle for one of the superplastic forming process .....	85
Figure 6-6 – Pressure control: pressure target vs real pressure.....	88
Figure 6-7 – Effective strain versus time in the hemispherical dome for the two models.....	88
Figure 6-8 – Numerical simulation results of behaviour law with ABAQUS software.	89
Figure 6-9 – Thickness measurement by digital image correlation.....	90
Figure 6-10 – Position of tool measure for thickness evaluation. ....	91
Figure 6-11 - Ultrasound inspection equipment and measured points in detail. ....	92
Figure 6-12 - Ultrasound inspection (a) results, and comparison with numerical data (b).....	92
Figure 6-13 – The average value of grain growth size distribution at 840 in the superplastic bulge forming °C was about $6.0 \pm 0.35 \mu\text{m}$ .....	93
Figure 6-14 – Comparison between experiment and numerical simulation at 840 °C (a) and in red, region where the shows measurement is performed region on piece (b).....	94
Figure 6-15 – FEGSEM BSE mode micrographs of Ti-6Al-4V alloy microstructure post-mortem samples experimental test at 840 °C: microstructure aspect showing equiaxed grains after bulge test (a) and (b); in detail can see ultra fined lamellae structure formed during colling (c) and (d); The white structure deposited by metallographic procedure (e) and (f). ....	95
Figure 8-1 – Numerical integration .....	118
Figure 8-2 – Type shell membrane S4R nodes reduced integration element.....	123
Figure 8-3 - Detailed flow of ABAQUS/Standard (PHAM, 2007). ....	125
Figure 8-4 - The interface to user subroutine CREEP .....	126



## LIST OF TABLES

Table 2-1 – Physical properties of unalloyed Titanium (JOSHI, 2006) .....	8
Table 2-2 Titanium alloys with SPF behaviour (LEYENS; PETERS, 2003).....	13
Table 2-3 – Strain rate sensitivity and activation of Ti-6Al-4V (ROY; SUWAS, 2013). .....	32
Table 2-4 - summary of superplastic behaviour evolution models.....	37
Table 3-1: Chemical composition (wt. %) for each Ti-6Al-4V sheet as-received.....	40
Table 3-2: Matrix for hot work (HW) test at high temperature.....	46
Table 3-3: Experimental Matrix - superplastic (SP) test at temperature - 3 grain size. .....	48
Table 4-1 - Dynamic Grain growth size ( $d_{dyn}$ ) measurements ( $\mu\text{m}$ ) (MTS). .....	63
Table 5-1 - Parameters of the grain growth evolution with the temperature .....	72
Table 5-2 – Temperature evolution of the identified parameters for the mechanical behaviour model (VELAY et al., 2016) .....	77

## LIST OF SYMBOLS AND ABBREVIATIONS

### Latin symbols and abbreviations

<b>Å</b>	Angstrom	$10^{-10}$ m
<b>BCC</b>	Body cubic center	
<b>CTA</b>	Centro Técnico Aeroespacial	
<b>DEGG</b>	Deformation-Enhanced Dynamic Grain Grown	
<b>DGG</b>	Dynamic Grain Grown	
<b>DNPM</b>	Departamento Nacional Produção Mineral	
<b>DRX</b>	Dynamic Recrystallization	
<b>EDS</b>	Energy dispersive spectroscopy	
<b>FEM</b>	Finite Element Method	
<b>FSS</b>	Fine Structure Superplasticity	
<b>GBS</b>	Grain boundary sliding	
<b>HCP</b>	hexagonal closed packed - Hexagonal	
<b>ISS</b>	Internal-stress Superplasticity	
<b>LEL-IPT</b>	Laboratório de Estruturas Leves - Parque Tecnológico de São José	
<b>MBD</b>	Mukherjee-Bird-Dorn	
<b>PCBN</b>	Polycrystalline cubic boron nitride	
<b>SGG</b>	Static Grain Grown	
<b>SPF</b>	Superplastic Forming	
<b>USGS</b>	United State Geological Survey	
<b>E</b>	Elastic modulus	GPa
<b>F</b>	force	N
<b>K</b>	Kelvin	K
<b>T<sub>β</sub></b>	Transus temperature	

**Greek symbols**

$\alpha$	Hexagonal close-packed phase of titanium alloys
$\alpha'$	Primary $\alpha$ -phase
$\alpha''$	Secondary $\alpha$ -phase
$\alpha_w$	$\alpha$ -phase Widmanstätten
$\alpha_{WGB}$	Widmanstätten $\alpha$ -phase grain boundary
$\alpha_{GB}$	$\alpha$ -phase at grain boundary
$\beta$	Body-centered cubic phase of titanium
$\beta_m$	B phase metastable
$\varepsilon$	Technical Strain
$\nu$	Poisson coefficient
$\tau$	Shear stress

## TABLE OF CONTENTS

<b>1. INTRODUCTION</b> .....	<b>1</b>
1.1. OBJECTIVES.....	4
1.1.1. <b>General objective</b> .....	<b>4</b>
1.1.2. <b>Specific objectives</b> .....	<b>4</b>
1.2. THESIS ORGANIZATION.....	6
<b>2. LITERATURE REVIEW</b> .....	<b>7</b>
2.1. TITANIUM .....	7
2.2. TITANIUM ALLOYS .....	9
2.2.1. <b>Alloying elements of titanium</b> .....	<b>9</b>
2.2.1. <b>Types of Titanium alloys</b> .....	<b>11</b>
2.2.2. <b>Superplastic Titanium alloys</b> .....	<b>13</b>
2.3. TITANIUM ALLOY – Ti-6Al-4V.....	14
2.3.1. <b>Ti-6Al-4V microstructure</b> .....	<b>16</b>
2.3.2. <b>Evolution Phase in the Ti-6Al-4V alloys</b> .....	<b>18</b>
2.3.3. <b>Mechanical properties of Ti-6Al-4V</b> .....	<b>20</b>
2.3.4. <b>Elevated temperature strength of Ti-6Al-4V</b> .....	<b>21</b>
2.4. SUPERPLASTICITY IN MATERIAL.....	22
2.4.1. <b>Generality on superplasticity</b> .....	<b>22</b>
2.4.2. <b>Deformation mechanism</b> .....	<b>25</b>
2.4.3. <b>Superplastic behaviour of Ti-6Al-4V</b> .....	<b>29</b>
2.4.4. <b>Industrial applications</b> .....	<b>31</b>
2.5. SUPERPLASTIC BEHAVIOUR MODELLING.....	34
2.5.1. <b>Classical models and evolution</b> .....	<b>34</b>
2.5.2. <b>Testing procedures</b> .....	<b>38</b>
<b>3. MATERIAL, EQUIPMENT AND EXPERIMENTAL PROCEDURE</b> .....	<b>40</b>
3.1. MATERIALS.....	40

3.2.	TENSILE TESTS AT HIGH TEMPERATURE .....	41
3.2.1.	<b>Samples .....</b>	<b>41</b>
3.2.2.	<b>Mechanical Tests on the Gleeble equipment .....</b>	<b>43</b>
3.2.2.1	<b>The Gleeble .....</b>	<b>43</b>
3.2.2.2	<b>Tensile tests conditions (Geeble).....</b>	<b>46</b>
3.2.3.	<b>Mechanical tests on the Servo-machine MTS 50 kN.....</b>	<b>46</b>
3.2.3.1	<b>The MTS 50 kN .....</b>	<b>46</b>
3.2.3.2	<b>Tensile tests in superplastic conditions (MTS 50 kN).....</b>	<b>48</b>
3.3.	STATIC TESTS AT HIGH TEMPERATURE CONDITION .....	48
3.4.	MICROSTRUCTURAL INVESTIGATION.....	50
3.4.1	<b>Sample preparation .....</b>	<b>50</b>
3.4.1.	<b>Sample observation and grain size measurement.....</b>	<b>51</b>
4.	<b>MECHANICAL TEST .....</b>	<b>52</b>
4.1.	DYNAMIC TESTS RESULTS.....	52
4.1.1.	<b>Gleeble 3800 test results.....</b>	<b>52</b>
4.1.2.	<b>Mechanical results.....</b>	<b>52</b>
4.1.3.	<b>Microstructural Analysis after mechanical testing .....</b>	<b>56</b>
4.1.4.	<b>Test results on samples tested on MTS 50kN equipment.....</b>	<b>58</b>
4.1.5.	<b>Mechanical behaviour .....</b>	<b>58</b>
4.1.6.	<b>Microstructure analysis after mechanical testing.....</b>	<b>61</b>
4.2.	STATIC GRAIN GROWTH.....	63
5.	<b>BEHAVIOUR MODELLING .....</b>	<b>67</b>
5.1.	LITERATURE REVIEW .....	67
5.2.	GRAIN GROWTH MODELLING .....	69
5.2.1.	<b>Static condition.....</b>	<b>69</b>
5.2.2.	<b>Dynamic Condition .....</b>	<b>71</b>
5.2.1.	<b>Results and discussions.....</b>	<b>72</b>

5.3.	MECHANICAL BEHAVIOUR MODELLING.....	73
5.3.1.	Constitutive equations .....	74
5.3.2.	Introduction of grain growth effect on the viscosity and the hardening law .....	75
5.3.3.	Results and discussions.....	76
6.	<b>SUPERPLASTIC BLOW FORMING.....</b>	<b>81</b>
6.1.	EXPERIMENTAL PROCEDURE.....	81
6.1.1.	Press Machine.....	82
6.2.	RESULTS OF SUPERPLASTIC FORMING.....	85
6.3.	MEASUREMENT THICKNESS ANALYSIS .....	90
6.3.1.	ATOS ScanBox®.....	90
6.3.2.	Ultra Sound Inspection .....	91
6.4.	EXPERIMENTAL GRAIN SIZE DISTRIBUTION .....	93
7.	<b>CONCLUSIONS AND PERSPECTIVES.....</b>	<b>96</b>
8.	<b>APPENDIX.....</b>	<b>108</b>
8.1.1.	IMPLICIT AND EXPLICIT ANALYSIS .....	117
8.1.2.	SURFACE MODELING AND MESH GENERATION .....	121
8.1.3.	Loading and Boundery conditions.....	124

## 1. INTRODUCTION

The processing costs and high acquisition of titanium and its alloys previously limited its widespread use. However, there are promising innovative technology that emerges to lower these costs, titanium is steadily gaining popularity as a material of choice for diverse structural applications.

In aeronautical industry, introduction of carbon fibre reinforced material in primary structures, like wings and fuselage, has pushed in a concomitant way the increase of titanium alloys in aircraft. As a matter of fact, titanium alloys are the preferred metal alloy for assembly with composites due to their lower thermal expansion coefficient and closer rigidity when compared to aluminum alloys. In the last generation aircrafts (Airbus 350 and Boeing 787) the weight percentage of titanium in the structure was increased from 7% to 15%. In order to decrease machining costs and scraps, more and more parts are hot formed as this process is less energy consuming and shortens the processing times. On the other hand, superplastic formed parts are still manufacturing for complex shaped parts.

Design and process engineers have to choose early in the designing stage either to use hot forming or superplastic forming. Important inputs are the high temperature properties and behaviour models as the process definition parameters and mould design are closely linked. More and more titanium part manufacturer and mould designer use process modelling in order to choose the optimal conditions for sheet material structure and properties but also to lower the cost; for example, lower temperature forming allows the use of cheaper forming die alloys.

Novo days if many titanium alloys have been characterized in superplastic forming range (820°C - 950°C) there is a lack in the hot forming range (650°C – 820°C). Moreover, unified and robust behaviour models, that could be used over a so broad range of temperature and strain rates as experienced by the titanium sheets during hot forming and superplastic forming, are still lacking.

From that idea comes up a proposal of this thesis focus on study of the mechanical behaviour and its microstructural evolution. Then, the international cooperation between institutes *Escola Politécnica da Universidade de São Paulo* (USP) and the *Institut Clément Ader of École Mines Albi-Carmaux* in France comes up

aims this research to develop the knowledge in the domain of manufacture process and its application of Ti-6Al-4V.

During hot and superplastic forming processes, the sheet forming capabilities depend on the selected alloy (microstructural properties and chemical composition) and on the process parameters (temperature and strain rate). The Ti-6Al-4V alloy is a typical  $\alpha + \beta$  titanium alloy, wherein the element Aluminum acts as an  $\alpha$  phase (HCP) stabilizer and the element Vanadium acts as a  $\beta$  phase (BCC) stabilizer

The attractive properties such as high strength to weight ratio, good fatigue properties and excellent corrosion resistance, have made Ti-6Al-4V a leading option for manufacturing aerospace and biomedical components. The development of the superplastic forming technology significantly contributes to manufacturing titanium alloy products of high performance with low cost and short cycle. In the hot forming process of titanium alloys, temperature control is essential due to the phase transformations that may cause degradation of the mechanical properties or even the embrittlement formed in the temperature range 940 - 980 °C.

In the present work, tensile tests performed on flat specimens in Ti-6Al-4V alloy at different temperatures and strain rates, were conducted by using a MTS hydraulic test machine. The thermo-mechanical behaviour was analyzed under hot forming conditions with a temperature range from 700 °C to 950 °C and a strain rate ( $\dot{\epsilon}$ ) from  $10^{-1} \text{ s}^{-1}$  to  $10^{-4} \text{ s}^{-1}$ . A unified behaviour model is formulated and the constitutive parameters were identified from the previous tests. It allows the prediction of both microstructural evolutions and strain-stress curves under variant temperature and strain rate conditions. Material sample tests and bulge forming results show that comparison between experiment and modelling as well as the microstructural evolution model are in a good agreement.

The formed microstructures open the need for further examination and understanding of the behaviour of the material, as well as how to model it. In order to reach that goal, it's usually necessary:

- that the alloy shows fine and equiaxed grain size, usually less than 10  $\mu\text{m}$ , that is stable during deformation;
- that forming temperature is greater than approximately half the absolute melting temperature of the subject material.

According to Peters (2003), there are more of 100 titanium alloys are known, but only of 20 to 30 have reached commercial status. The Figure 1-1 illustrates some of the titanium alloys applications for different domains.

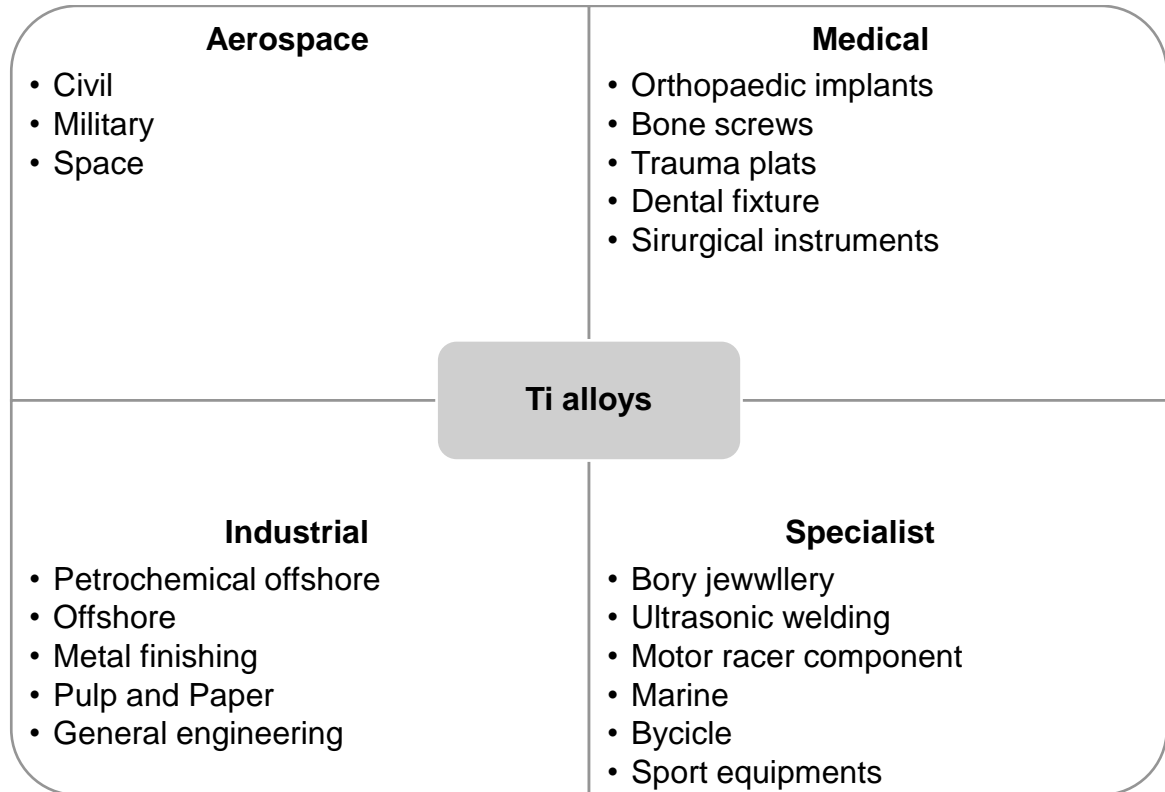


Figure 1-1 - Titanium alloys at domains applications.

## 1.1.OBJECTIVES

The main objective of this thesis is give a contribution to titanium alloys study applied to manufacturing process.

### 1.1.1. General objective

The general aim of this thesis is to address the forming behaviour of Ti-6Al-4V titanium alloys, applied to aeronautical components, in both hot forming and superplastic domain in order bridge the gap between this today separate forming conditions.

Figure 1-2 shows the general work logic that has been followed, integrating experimental test and numerical behaviour modelling research activities.

### 1.1.2. Specific objectives

- Mechanical behaviour analyses for three different sheets within initials grain sizes of commercial Ti-6Al-4V alloy.
- Improve the behaviour model based on the microstructure evolution to Ti-6Al 4V alloy based on the microstructural evolution.
- Numerical modelling analyses on ABAQUS 6.12 at high temperature tensile test on bulge forming.
- Correlate the Ti-6Al-4V alloy microstructure evolution with experimental forming.

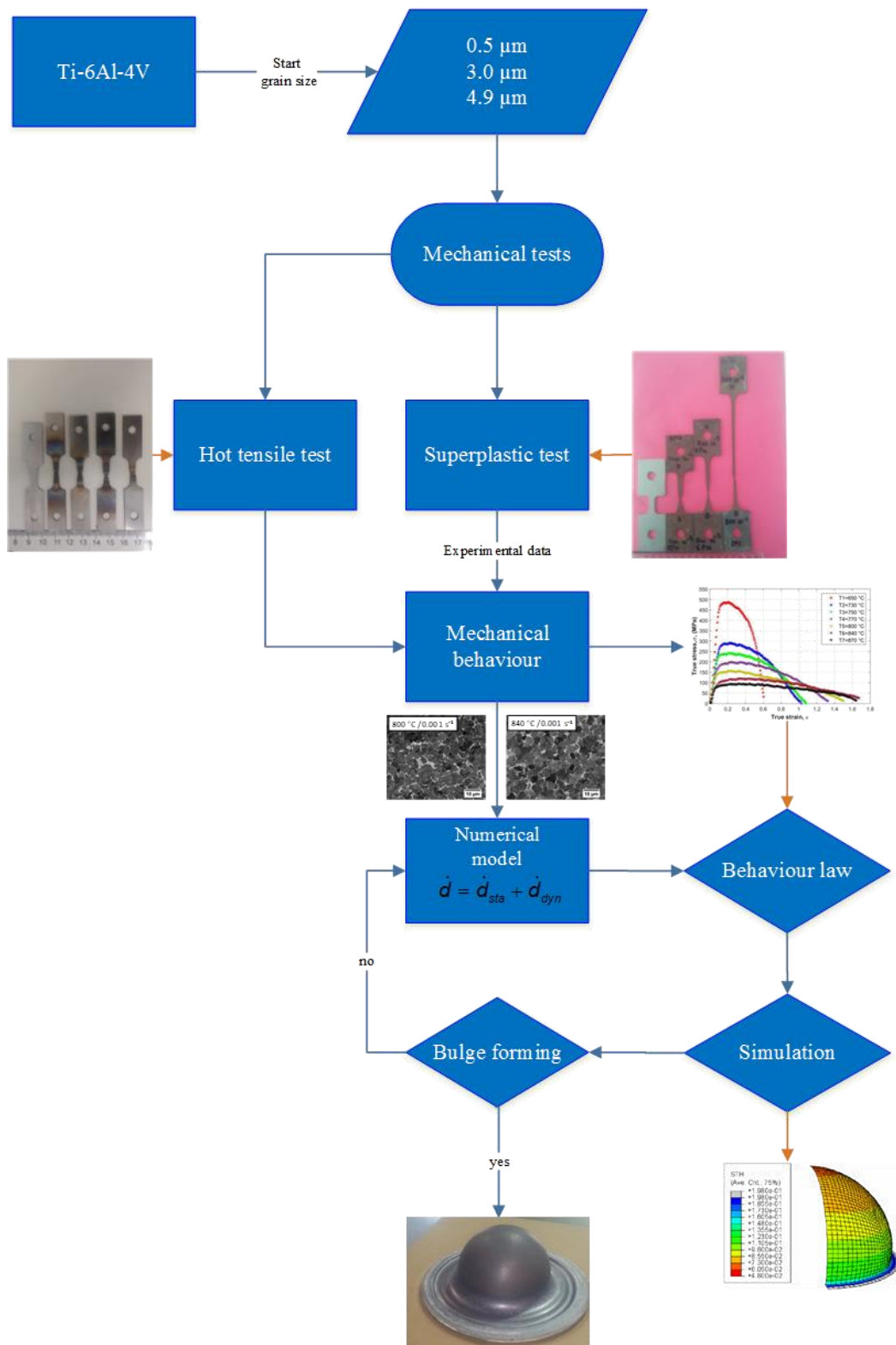


Figure 1-2 - Resumed flowchart of the experimental test and theoretical modelling approach.

## 1.2. THESIS ORGANIZATION

### **Chapter 2**

This chapter is dedicated to bibliography review about relevant Titanium research and its metallurgical properties. The titanium alloys and specially Ti-6Al-4V alloy which is object for this work are presented. The principle features of the superplastic behaviour are explained and general basic material behaviour models are listed.

### **Chapter 3**

The three titanium alloy materials investigated in this thesis are first presented. Then testing methods for the experimental campaign are described. Mechanical test equipment's (Gleeble and servo-hydraulic) and test campaigns are presented the static ageing test method as well. Finally, microstructural investigation procedure for grain size measurement is explained.

### **Chapter 4**

This chapter presents all the stress-strain curves at various temperatures obtained with the two-mechanical test equipment's at different stress rates. Microstructures of the samples after mechanical testing but also after only static ageing are shown and discussed.

### **Chapter 5**

This chapter provides an introduction about the constitutive equations and its formulation used in present thesis. Based on experimental results gained previously, a unified constitutive behaviour model is formulated. It includes kinematic hardening, strain rate sensitivity and grain growth. Model parameters are identified and model prediction results are compared to experimental curves.

### **Chapter 6**

In this chapter, the bulge forming test performed at Light Structure Labs (IPT-LEL) is presented. Models developed in previous chapter were implemented in a FEM code and simulations were compared to the experimental results. Finally, work is summarized and possible areas of future research involving optimization of hot and superplastic forming are suggested.

## 2. LITERATURE REVIEW

An approach about titanium and its alloys is presented as main materials study of that thesis and specifically Ti-6Al-4V alloy. Others important subjects are explained such as superplasticity in materials and superplastic behaviour modelling.

### 2.1. TITANIUM

About the Titanium's genesis history. In 1791 Sir William Gregor, the British reverend, mineralogist, and chemist discovered titanium. He examined the magnetic sand from the local river, Helford, in the Manechan Valley in Cornwall, England, and isolated "black sand", now known as "ilmenite". By removing the iron with magnet and treating the sand with hydrochloric acid Sir Gregor produced the impure oxide of a new element and it named "mechanite" (PETERS, M., 2003).

At around the same time, Franz Joseph Muller also produced a similar substance, but could not identify it. The element was independently rediscovered several years later by German chemist Martin Heinrich Klaproth in rutile ore. Klaproth confirmed it as a new element and in 1795 he named it after the Latin word for Earth, also the name of the Titans of Greek mythology. Rutile is naturally occurring in Australia, USA, India and South Africa after location (DEARNALEY; WATKINS, 1984; DONACHIE, 2000; RTI INTERNATIONAL METALS, 2013).

In 1910 at Rensselaer Polytechnic Institute in Troy, New York, Matthew Hunter could isolate the metal by heating titanium tetrachloride ( $\text{TiCl}_4$ ) with sodium in a steel bomb. Finally, Wilhelm Justin Kroll from Luxemburg was recognized as father of the titanium industry process (PETERS, 2003). The titanium unalloyed properties values are listed in the Table 2-1.

Titanium has two allotropic forms: Ti- $\beta$  with hexagonal close packed (hcp) Crystal structure (up to 882.5 °C) and Ti- $\alpha$  with body centred cubic (bcc) crystal structure (between 882.5 and 1662 °C). Each of the allotropes exhibit different plasticity resulting from its crystal structure and different number of the slip systems.

Titanium is not actually a rare substance as it ranks as the ninth most plentiful element and the fourth most abundant structural metal in the Earth's crust exceeded only by aluminium, iron, and magnesium. Unfortunately, it is seldom found in high concentrations and never found in a pure state. Thus, the difficulty in processing the

metal makes it expensive. Even today it is produced only in a batch process, and no continuous process exists as for other structural metals. Titanium usually occurs in mineral sands containing ilmenite ( $\text{FeTiO}_3$ ), found in the Ilmen mountains of Russia, or rutile ( $\text{TiO}_2$ ), from the beach sands in Australia, India, and Mexico. Titanium dioxide is a very versatile white pigment used in paint, paper, and plastic, and consumes most of world production (DNPM, 2015).

Regarding all the 118 chemical elements in the periodic system known nowadays, about 85% are metals or metalloids. There are various ways to classify the metals, such as ferrous or non-ferrous metals, ingot or sintered metals, light or heavy metals. Titanium is classified as a non-ferrous and light metal (ZIMMERMANN, 2008).

Table 2-1 – Physical properties of unalloyed Titanium (JOSHI, 2006)

Property	Value
Atomic number	22
Atomic Weight	47.9 u
Cristal structure	
$\alpha$ -hcp	c= 4.6832 $\pm$ 0.0004 Å a=2.9504 $\pm$ 0.0004 Å c/a= 15.873 $\pm$ 0.003 Å
$\beta$ -bcc	a = 3.28 $\pm$ 0.003 Å
Density	4507 kg/m <sup>3</sup>
Coefficient. of thermal expansion at 20 °C	8.4 x 10 <sup>-6</sup> K <sup>-1</sup>
Thermal conductivity	21.9 W/ (m.K)
Specific heat	520 J/(Kg.K)
$\alpha$ to $\beta$ transus temperature	882 °C
Latent heat of transformation	1050 Cal/mole
Heat of fusion	5020 Cal/mole
Melting point	1668 °C
Heat of vaporization	112,500 Cal/mole
Boiling point	3260°C
Electrical resistivity:	
High purity	420 $\mu\Omega$ -m
Commercial purity	55 $\mu\Omega$ -cm
Modulus of elasticity	116 GPa
Shear Modulus	44 GPa
Poisson Ratio	0.32

## 2.2. TITANIUM ALLOYS

The titanium alloys can be classified according to their microstructure in determined state. It must be emphasized that this classification is questionable, because phase transformations in alloys with transition elements proceed so slowly, that very often the microstructure consistent with phase equilibrium diagram cannot be obtained at room temperature. According to widely accepted classification of the alloys in normalized state following types of titanium alloys can be distinguished (Peters 2003). The properties of titanium alloys are essentially determined by two factors: the chemical composition and their microstructures.

### 2.2.1. Alloying elements of titanium

Two phase titanium alloys most often are hot deformed, mainly by open die or close-die forging. Desired mechanical properties can be achieved in these alloys by development of proper microstructure in plastic working and heat treatment processes. Irreversible microstructural changes caused by deformation at the temperature in  $\alpha + \beta \leftrightarrow \beta$  phase transformation range quite often cannot be eliminated or reduced by heat treatment and therefore required properties of products cannot be achieved. Some of the properties of titanium alloys, such as: high chemical affinity to oxygen, low thermal conductivity, high heat capacity and significant dependence of plastic flow resistance on strain rate, make it very difficult to obtain finished products having desired microstructure and properties by hot working. Differences in temperature across the material volume, which result from various deformation conditions (local strain and strain rate) lead to formation of zones having various phase composition (equilibrium  $\alpha$  and  $\beta$  phases, martensitic phases  $\alpha'$ ( $\alpha''$ )), morphology (equiaxial, lamellar, bi-modal) and dispersion (fine - or coarse-grained) and therefore various mechanical properties (TILEY, 2002).

Titanium alloys can exhibit a wide of variety of microstructure depending upon alloy chemistry, processing and heat treatment. This is made possible because titanium and its alloys exhibit a broad range of phase transformations. Some of these transformations are related to the  $\alpha$  to  $\beta$  allotropic transformations, while others are precipitations reactions. For illustrate these allotropic transformations see Figure 2-1.

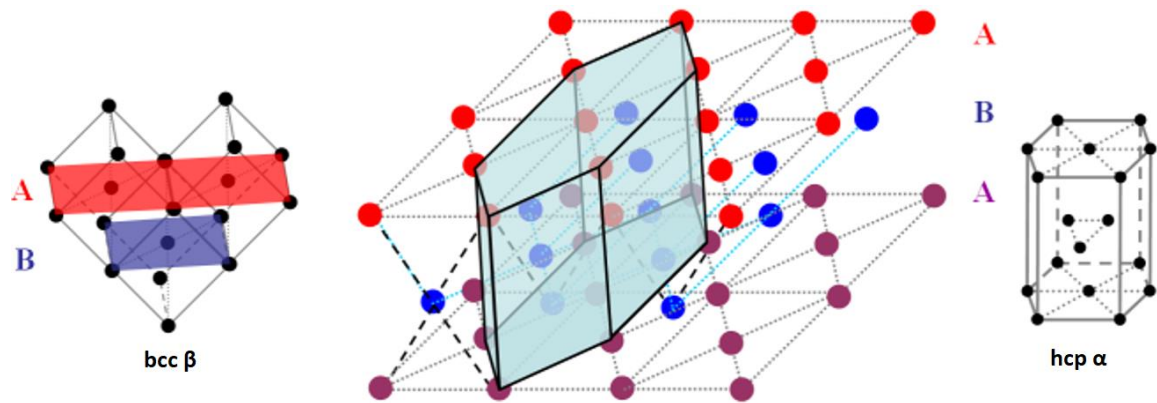


Figure 2-1 – Allotropic transformation between body centred cubic - bcc  $\beta$  and hexagonal compact - hcp  $\alpha$ . The stacking A and B are representing by cubic lattice in red and blue (REVIL-BAUDARD, 2010).

Titanium has an incomplete shell in its electronic structure, which enables the formation of solid solutions with most substitutional elements having a size factor within  $\pm 20\%$ . Elements like carbon, oxygen, etc. form interstitials. The stabilization of  $\alpha$  or  $\beta$  phase depends on the number of electrons per atom of the alloying element (or the group number). Alloying elements with an electron/atom (e/a) ratio of less than 4 stabilize the  $\alpha$  phase, and elements having a ratio greater than 4 stabilize the  $\beta$  phase.

The alloying elements can be classified the elements in the periodic chart into four major groups, depending on their interaction with titanium (RTI INTERNATIONAL METALS, 2013).

- Continuous solid-solution-forming elements with  $\alpha$  or  $\beta$  titanium: Zirconium and hafnium have an outer-shell electronic configuration identical to that of titanium. The structure is also isomorphic to titanium. Thus, the phase diagrams with these elements show continuous  $\alpha$  and  $\alpha$  solid solutions. Vanadium, niobium, tantalum, and molybdenum are isomorphic to  $\alpha$ -titanium and form a continuous solid solution with the  $\beta$  allotrope of titanium. These elements have limited solubility in  $\alpha$  phase.
- Limited solid-solution-forming elements with  $\alpha$  and  $\beta$  titanium: Chromium, manganese, iron, cobalt, nickel, and copper undergo eutectoid transformation and lower the  $\beta$  transus. With the increase in the group number, the maximum solubility in  $\beta$  titanium decreases and eutectoid temperature increases. Aluminium, gallium, and indium show a peritectoid reaction and raise the  $\beta$  transus. These elements have higher solubility in  $\alpha$  titanium.

- Ionic and covalent compound-forming elements: Fluorine, chlorine, bromine, iodine, Sulphur, selenium, tellurium, and phosphorous form ionic and covalent compounds with titanium. They do not go into solid solution in  $\alpha$  or  $\beta$  titanium.
- Elements not interacting with titanium: Except beryllium, which has limited solubility in  $\beta$  titanium, no other alkali or alkaline earth metal interacts with titanium.

### 2.2.1. Types of Titanium alloys

Titanium has two allotropic modifications:  $\alpha$ , which has a closely packed hexagonal structure (hcp), and  $\beta$ , having a body-centred cubic (bcc) structure. Various elements forming solid solution with titanium are classified based on their effect on the solubility of  $\alpha$  or  $\alpha$  phases. Elements stabilizing  $\alpha$ -phase are known as  $\alpha$  stabilizers (Al, Ga, O, N, C), and elements stabilizing  $\beta$ -phase are known as  $\beta$  stabilizers (V, Mo, Nb, Fe, Cr, Ni, etc.). Some of the elements like Sn and Zr are neutral, as they do not stabilize either  $\alpha$  or  $\beta$  phase, though they enter solid solution with titanium.

Aluminum is the only  $\alpha$  stabilizer of commercial importance and forms a constituent of most of the commercial titanium alloys. The aluminum content is normally restricted to 7% or aluminum equivalent to 9% in the commercial titanium alloys to avoid precipitation of  $Ti_3Al$  phase, which leads to severe embrittlement. Aluminum equivalent (Rosenberg criterion) =  $Al + Sn/3 + Zr/6 + 10(O+C+N)$ .

Recent developments in Titanium alloys exploit the high temperature properties of intermetallic  $Ti_3Al$  ( $\alpha_2$ ) and  $TiAl$  ( $\gamma$ ). Molybdenum, Vanadium, Niobium, and Tantalum (isomorphs with titanium), which are the  $\beta$ -stabilizing elements, are generally the preferred alloying additions in commercial titanium alloys. Iron and chromium are also added in limited amounts, although they are eutectoid-forming  $\beta$  stabilizers. Based on the alloying additions and phases present in the microstructures, titanium alloys are classified as follows (Joshi 2006):

- **Alpha( $\alpha$ ) alloys:**

These are single-phase alloys, solid solution strengthened by the addition of  $\alpha$  stabilizers or neutral alloying elements. Alpha alloys have good stability and good high temperature properties but are not amenable to heat treatment for microstructural property modifications.

- **Near  $\alpha$  alloys:**

Small additions (1 to 2%) of  $\beta$  stabilizers improve the strength and workability and are a good compromise between the higher strength of  $\alpha+\beta$  alloys and the creep resistance of simple  $\alpha$  alloys. The most widely used commercial high-temperature titanium alloys for aero-engine application belong to this class. They are primarily  $\alpha$  alloys containing some amount of retained  $\beta$  in the final microstructure.

- **$\alpha+\beta$  alloys:**

These alloys contain larger amounts of beta stabilizers (4 to 6%). Beta alloys can be heat-treated to develop a variety of microstructures and mechanical property combinations. Ti-6Al-4V, the most widely used alloy, belongs to this class.

- **Metastable  $\beta$  alloys:**

In alloys containing 10 to 15% of  $\beta$  stabilizers,  $\beta$ -phase is retained at room temperature in a metastable condition. This metastable  $\beta$  can be aged to form very fine Widmanstätten  $\alpha$  in the matrix of enriched  $\beta$ . These alloys have high strength, toughness, excellent hardenability, and forgeability over a wide range of temperatures. These alloys contain small amounts of  $\alpha$ -stabilizing elements as strengthening agents. Beta and near- $\beta$ -alloys offer increased fracture toughness over  $\alpha + \beta$  alloys at a given strength level. They are finding increasing use in aircraft structural applications.

- **Beta ( $\beta$ ) alloys:**

Very large addition (30%) of  $\beta$  stabilizers results in retaining  $\beta$  as a stable phase at room temperature. Beta alloys resemble refractory metals in their high densities and poor ductility and are used for highly specialized burn-resistance and corrosion-resistance applications.

- **Titanium aluminides:**

Several attractive intermetallic alloys have been developed with useful ductility and strength. These alloys are based on the intermetallic compounds  $Ti_3Al$  ( $\alpha_2$ ) and  $TiAl$  ( $\gamma$ ). The alloys based on  $Ti_3Al$  usually contain a large amount of Nb additions and other  $\beta$  stabilizers (10–25 at. %, 20–45 wt.%). They consist of  $\beta$  phase or B2 phase to improve their ductility. The  $TiAl$  is also alloyed with  $\beta$

stabilizers such as Nb, V, Mn, and Cr in limited amounts. Recently, alloys based on compound  $Ti_2AlNb$  are also under evaluation. All these alloys possess excellent high-temperature properties and good oxidation resistance but have poor ductility and fracture toughness. This has limited their use in commercial applications.

### 2.2.2. Superplastic Titanium alloys

Titanium alloys together with aluminium alloys belong to the largest group of superplastic materials used in industry. Their main advantages are good superplasticity combined with relatively high susceptibility to diffusion bonding. Among them two-phase  $\alpha + \beta$  Ti-6Al-4V alloy has been the most popular for many years as it exhibits superplasticity even after application of conventional plastic working methods.

Several titanium alloys showing superplastic behaviour are listed in Table 2-2; strain rate sensitivity ( $m$ ) and typical optimal strain rates and maximum elongation are indicated.

Table 2-2 Titanium alloys with SPF behaviour (LEYENS; PETERS, 2003)

Alloy	Temperature [°C]	Strain rate ( $\dot{\epsilon}$ ) [ $s^{-1}$ ]	$m$	A [%]
Ti-6Al-4V	880	$2 \times 10^{-4}$	0.8	1000
Ti-6Al-4V	930	$2 \times 10^{-4}$	0.9	800
Ti-6Al-4V	840 to 940	$10^{-4}$ to $10^{-3}$	0.7 to 0.8	700 to 1200
Ti-6Al-5V	850	$8 \times 10^{-4}$	0.7	1100
Ti-6Al-2Sn-4Zr-2Mo	900	$2 \times 10^{-4}$	0.7	600
Ti-4Al-4Mo-2Sn-0.5Si	850 to 920	$10^{-4}$ to $10^{-3}$	0.7	1230
Ti-6Al-4V-1Co	835	$10^{-4}$	-	1090
Ti-6Al-4V-2Ni	815	$2 \times 10^{-4}$	0.8	700
Ti-6Al-4V-2Co	815	$2 \times 10^{-4}$	0.5	700
Ti-6Al-4V-2Fe	815	$2 \times 10^{-4}$	0.5	1090
Ti-6Al-4V-1Fe-1Co	815	$2 \times 10^{-4}$	0.7	500
Ti-6Al-4V-1Fe-1Ni	835	$2 \times 10^{-4}$	0.7	550
Ti-3.9Al-3.7V-3Mo-1Fe	750			2000
Ti-5Al-2Sn-4Mo-2Cr-1Fe	700 to 775	$10^{-4}$ to $10^{-3}$	0.4 to 0.5	1000

### 2.3. TITANIUM ALLOY – Ti-6Al-4V

Ti-6Al-4V is the most used titanium alloy in industry such as aerospace, aeronautic, automobile and medical prosthesis and: by itself it represents 45% of the titanium consumption. This is mainly because Ti-6Al-4V combines a quite easy processing and good properties (Vanderhastan, Rabet, and Verlinden 2008).

There are several reasons for the extensive application of Ti-6Al-4V:

- It is both heat treatable and weldable.
- It can be produced in all shapes such as sheet, plate, tube, bar, pipe and wire
- Its mechanical and chemical properties and fabrication procedures became fully characterized.
- Mill scrap could be recycled.

Ti-6Al-4V has a high specific strength, stability at temperature up to 400°C and good corrosion resistance but unfortunately is very expensive. It will thus only be used when weight and corrosion are critical considerations. The aerospace industry uses essentially wrought Ti-6Al-4V in gas turbine engines (compressor blades, discs and wheels) and for airframe applications. In addition, fine equiaxed grains grade of this alloy show superplastic behaviour and are exploited to produce very complex structures together with diffusion bonding as a joining technique.

According to (PETERS, 2003a; SURAND, 2013), the Aluminium (Al) is the element known as  $\alpha$ -stabilizers is one of the most important element for Titanium. In addition to extending the  $\alpha$ -phase field to higher temperatures, the  $\alpha$ -stabilizers develop a two-phase  $\alpha+\beta$  field. The system Ti-Al is the most relevant and by far most intensively investigated titanium phase diagram is Figure 2-2. The  $\beta$ -stabilizing elements shift the  $\beta$  phase field to lower temperatures as shown in Figure 2-3.

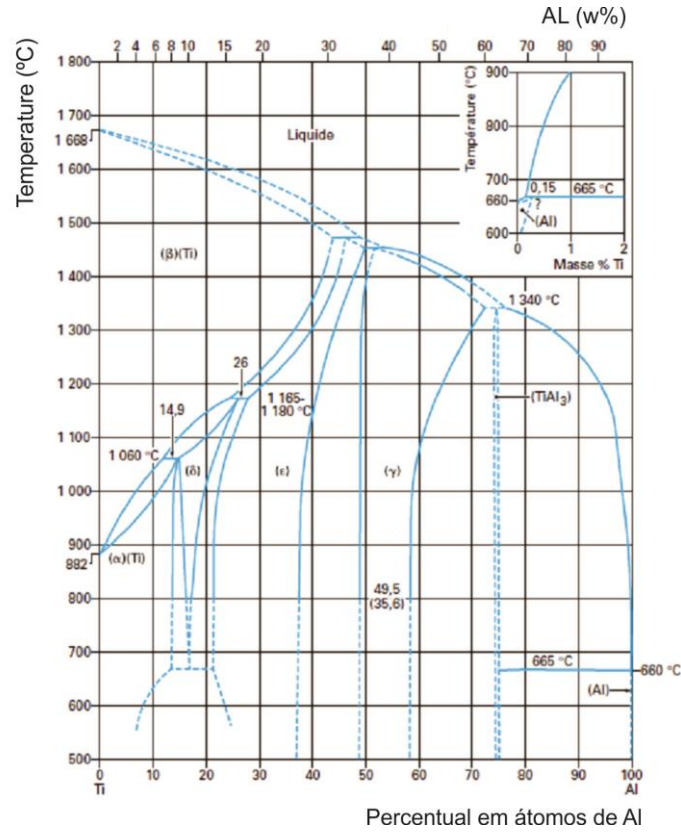


Figure 2-2 The Ti-Al phase diagram (Adapted from SURAND, 2013)

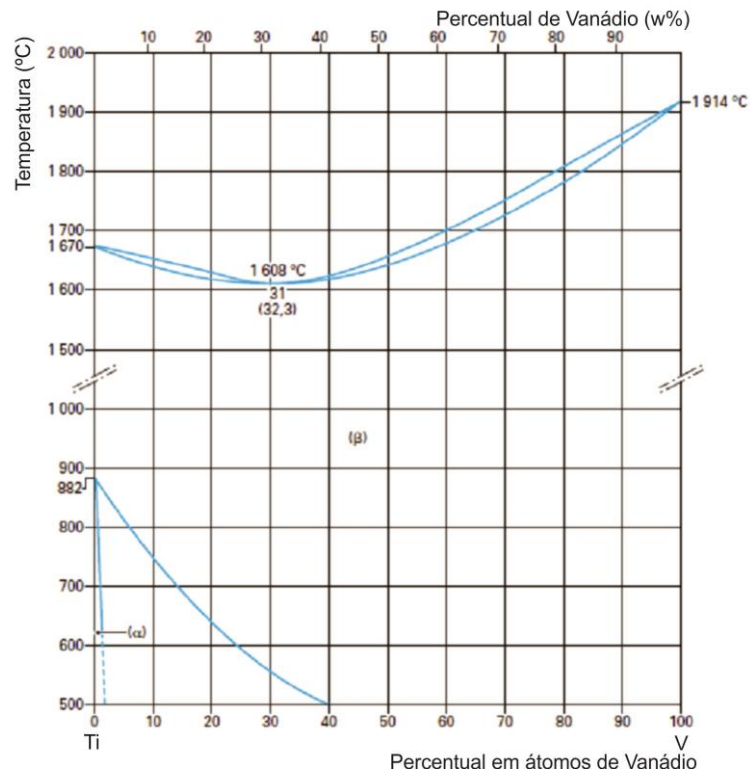


Figure 2-3 – The Ti-V phase diagram (Adapted from SURAND, 2013)

### 2.3.1. Ti-6Al-4V microstructure

As an  $\alpha+\beta$  alloy, Ti-6Al-4V contains a certain proportion of  $\beta$ -phase at room temperature. This proportion is function of the thermal treatment and of the interstitial content, particularly of the O fraction. To be stable at room temperature the  $\beta$ -phase needs at least 15% of vanadium. This can be achieved when the alloy is slowly cooled in furnace or annealed below 750 °C (VANDERHASTEN, RABET, and VERLINDEN 2008).

Air cooling results in a needle-like  $\alpha$ -phase (acicular  $\alpha$ ). According (DONACHIE, 2000), different varieties of phase morphologies form depending on the temperature history of the Ti-6Al-4V alloy.

Three basic and typical micro-structures are shown in Figure 2-4 : Intermediate cooling develops Widmanstätten microstructures. Quenching from temperatures greater than 900 °C results in a needle-like hcp martensite ( $\alpha'$ ), while quenching from 750-900 °C produces an orthorhombic martensite ( $\alpha''$ ) (JOSHI, 2006).

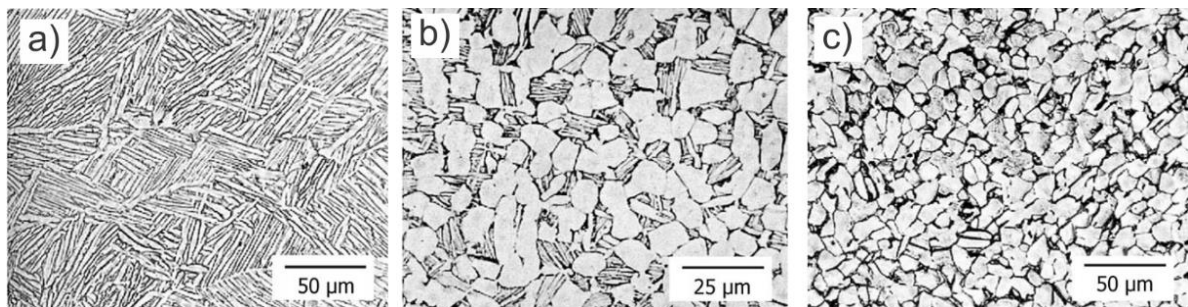


Figure 2-4 Three basic microstructure types in Ti-6Al-4V: a) lamellar; b) bimodal and c) equiaxed. Adapted From (DONACHIE, 2000).

For illustrate that effect, Figure 2-5 shows a diagram for different microstructure that can be formed depending on the cooling rate. During fast cooling, denoted as water quenched c) and e), the  $\beta$  phase will transform into martensite  $\alpha'$ .

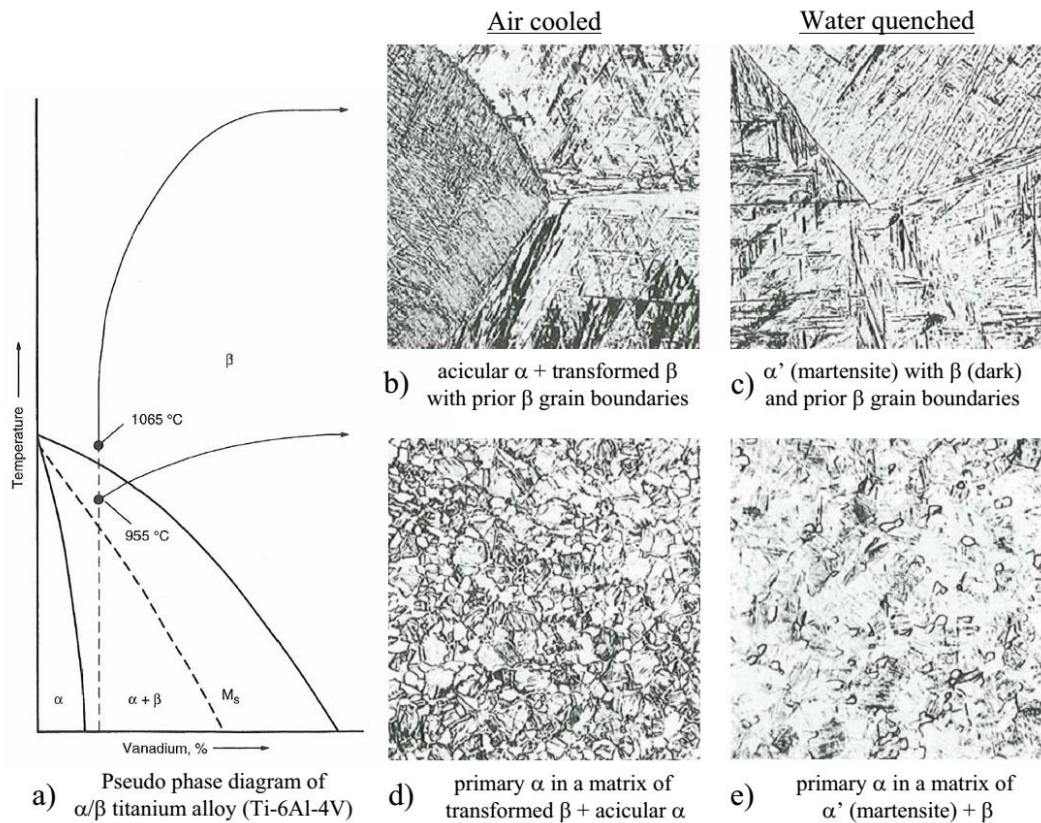


Figure 2-5 - The microstructure of Ti-6Al-4V for different cooling processes adapted from Donachie (2000).

The martensite  $\alpha'$  will then recover to  $\alpha + \beta$  after longer time maintained at medium high temperature as indicated in the lower part of the TTT-diagram Figure 2-6.

While for slower cooling rates from high temperature, exemplified by air cooling in Figure 2-4 b) and d), the  $\alpha$ -phase forms Widmanstätten plate-like or “basket-weave” acicular  $\alpha$  (with transformed  $\beta$ ) by nucleation and growth. Widmanstätten  $\alpha$  takes different morphologies depending on the cooling rate, spanning from aligned platelets in colonies to a “basket-weave” type of structure.

“Basket-weave” morphology forms when it becomes more energy efficient to nucleate new  $\alpha$ -lamellae than grow the existing lamellae. There are twelve possible orientation variants of  $\alpha$  in  $\beta$ . Multiple occurrences of these orientation variants form the “basket-weave” morphology. Therefore, the basket-weave morphology represents repeated nucleation of the Widmanstätten growth morphology. Finally, “basket-weave” structure is assumed to be a finer form of Widmanstätten morphology interpreted to be colonies of  $\alpha$ -plates formed with specific orientations to each other (VILANE, 2012).

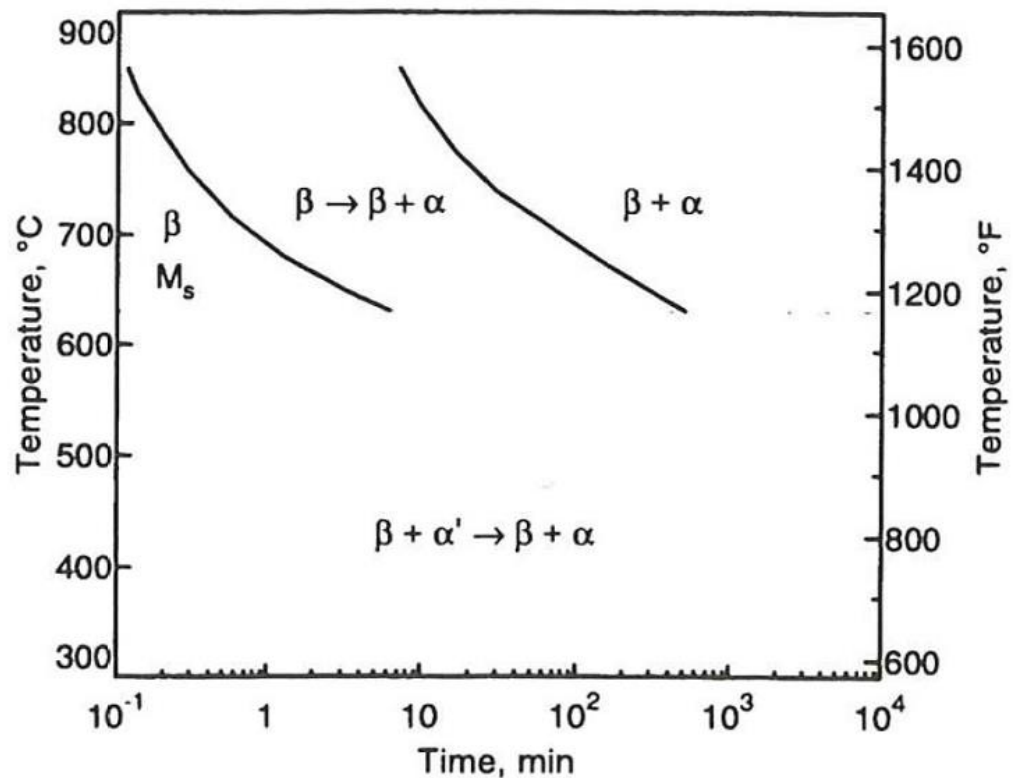


Figure 2-6 - Time-Temperature-Transformation (TTT) diagram for Ti-6Al-4V. The alloy was solution annealed at 1020 °C, and quenched to a given temperature where the transformation was observed (DONACHIE, 2000).

### 2.3.2. Evolution Phase in the Ti-6Al-4V alloys

According to Babu (2008), the temperature at which  $\alpha$  changes to  $\beta$  ( $\beta$ -transus temperature) depends on the composition of Aluminum and Vanadium.

The  $\beta$ -transus temperature is also sensitive to interstitial impurity; for example, higher amount of oxygen ( $O_2$ ) will raise  $\beta$  transus, whereas higher amounts of iron will lower it. Depending on the processing conditions, this alloy can form two stable phases ( $\alpha$  and  $\beta$ ), two metastable phases ( $\alpha'$  and  $\alpha''$ ) and the intermetallic phase  $\alpha_2$  as illustrate Figure 2-7.

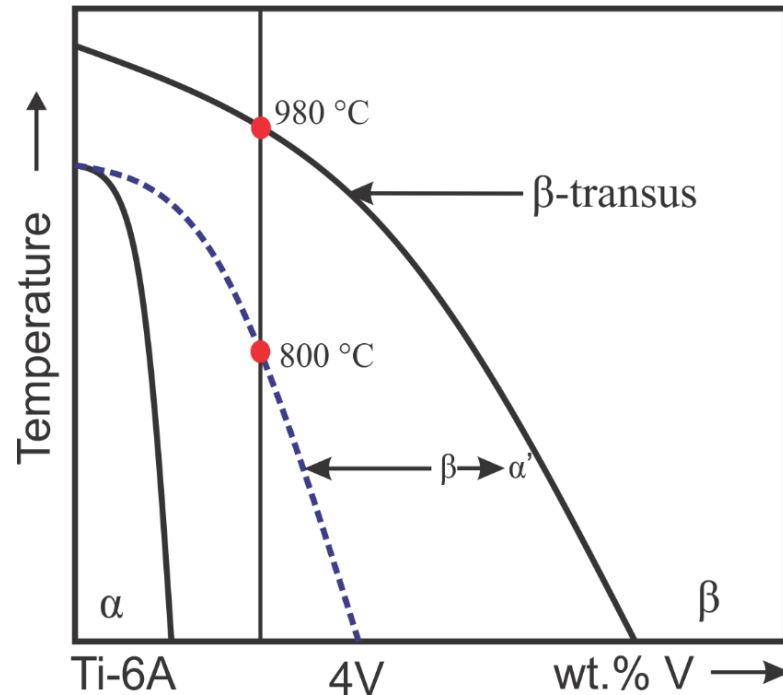


Figure 2-7 Ternary phase diagram, adapted from (BABU, 2008)

Besides these two phases, depending on the thermos-mechanical treatments, different other phases can be observed later in the Ti-6Al-4V alloy.

- **α' (Hexagonal close packed martensite):**

When the alloy is quenched from above 900 °C, a part of the β-phase will transform in α'. The α' has an acicular or sometimes fine lamellar microstructure. Crystallographically, it is related to the α-phase and their lattice parameters are very close.

- **α'' (Orthorhombic martensite)**

α'' is the result of a quenching of the β-phase from between 750 and 900 °C. This martensite is softer than α'. The formation of α'' can also be induced by straining metastable β.

- **ω (Omega precipitation)**

The formation of this phase is prevented by the presence of oxygen. In Ti-6Al-4V of industrial purity is normally never observed ω. But in β-phase highly rich in vanadium (more than 15 %), precipitation of ω can occur in the temperature range from 200 °C to 350 °C during aging or during room temperature aging in rapidly solidified material. Nevertheless, this precipitate is almost never observed in Ti-6Al-4V (PETERS, 2003).

- **$\alpha_2$  (Ti<sub>3</sub>Al precipitation)**

- To form  $\alpha_2$  the proportion of oxygen in the grade of Ti-6Al-4V must be less than 0.2 wt.% and the alloy must be aged at temperatures between 500 and 600 °C. The presence of Ti<sub>3</sub>Al promotes coarse planar glide on  $\{10\bar{1}0\}$  prismatic planes (OBASI et al., 2012). About the microstructure three different classes can be roughly distinguished: lamellar; equiaxed or a mixture of both.

- **Lamellar**

structures can be easily obtained by thermal treatment. Starting from above the  $\beta$  transus, the cooling rate will determine the size of the lamellae. Slow cooling about 15 K/min in the furnace will lead to the production of coarse plates of  $\alpha$ -phase starting from the  $\beta$ -grain boundaries and at the opposite quenching produces a needle like hcp martensite ( $\alpha'$ )

- **Equiaxed**

microstructures need extensive mechanical working (>75 %) in the ( $\alpha+\beta$ )-phases domain. During this process, the  $\alpha$  lamella are broken into equiaxed  $\alpha$  grains. A subsequent annealing at about 700°C produces the so-called "mill-annealed" microstructure. The result is very dependent of the previous working. Another possibility to obtain equiaxed grains is a recrystallization of the deformed material in the  $\alpha+\beta$ -phase field, at 925 °C during 4h, followed by slow cooling. In this second case, a more reproducible microstructure is obtained but, the resulting  $\alpha$  grains are coarse (grain size about 15-20  $\mu\text{m}$  instead of 8-10  $\mu\text{m}$ ) (VANDERHASTEN; RABET; VERLINDEN, 2008).

- **Bimodal microstructure**

consists of isolated primary  $\alpha$  grains in a transformed  $\beta$  matrix. This type of microstructure is obtained by quenching from the  $\alpha+\beta$  -phase field (approximately between 750 and 1000°C). After quenching, the  $\beta$  -phase is transformed in  $\alpha'$  or  $\alpha''$  in function of the anneal temperature and  $\alpha$  grains remain unchanged.

### 2.3.3. Mechanical properties of Ti-6Al-4V

Earlier work has shown that the initial microstructure such as the fraction of  $\alpha$  and  $\beta$  phases, the morphology and thickness of  $\alpha$ -lathes as well as the size of  $\alpha$  colonies (the geometrical arrangement of  $\alpha$  and  $\beta$ -phases) have significant effects on

the mechanical properties of the Ti-6Al-4V alloy (BHATTACHARYYA et al., 2006; BUFFA; FRATINI; MICARI, 2012; ODENBERGER et al., 2012).

The literature shows that among the all microstructural characteristics, a colony size has the most significant influence on the mechanical properties. It has furthermore been shown that parameters such as the cooling rate from the  $\beta$ -phase field, the initial  $\beta$  grain size and the presence of interstitial impurities (oxygen and carbon), can affect the geometrical arrangement within the microstructure of the Ti-6Al-4V alloy (DEGHAN-MANSHADI, 2010; PETERS, 2003; RHAIPU, 1998).

The cooling rate seems to be one of the most important parameters affecting microstructural development. Whereas slow and intermediate cooling rates lead to nucleation and growth of  $\alpha$ -lamellae into the initial  $\beta$  grains through a diffusion controlled process, higher cooling rates render a martensitic transformation. The influence of different initial microstructures on the mechanical properties of a variety of  $\alpha + \beta$  titanium alloys containing a single morphology, has been extensively studied. However, the case is more complicated when a mixture of different morphologies with different responses to hot deformation exists in the initial structure.

#### **2.3.4. Elevated temperature strength of Ti-6Al-4V**

The properties of titanium alloys are essentially determined by two factors: the chemical composition and the microstructure.

The chemical composition of the titanium alloys primarily determines the properties and volume fraction of the phases,  $\alpha$  and  $\beta$ . Due to the limited deformation capability of hexagonal dense packed crystal structures,  $\alpha$  is less ductile compared with the body-centred cubic  $\beta$ .

Therefore, the resistance to creep and oxidation increases with increasing aluminium content, while simultaneously the ductility and the deformation capability deteriorate. Therefore, care had to be taken when new alloys were developed to not exceed 9 wt.% of the so-called aluminium-equivalent (Aluminium equivalent = wt. % Al + 1/3 wt. % Sn + 1/6 wt. % Zr + 10 wt. % O < 9 wt. %)

For otherwise the alloy-embrittling intermetallic compound  $Ti_3Al$  precipitated. For this reason, the aluminium content of conventional titanium alloys was limited to a maximum of 6 wt. % for a long time.

## 2.4. SUPERPLASTICITY IN MATERIAL

In this section will be present the main points about superplasticity in material such as generality on superplasticity, deformation mechanism and superplastic behaviour of Ti-6Al-4V and industrial application.

### 2.4.1. Generality on superplasticity

As noted by Hamilton (1984), Superplasticity is of relatively recent scientific interest, much of the research attempting to understand the physical mechanism and to utilize this phenomenon being started in the early 1960's.

In International Conference on Superplasticity in Advanced Materials (ICSAM) since 2003, a wide variety of metal alloys and ceramics exhibit superplastic behaviour each with an associated forming temperature and strain rate which maximizes the ductility during forming. However in commercial practice the most popular alloys are Ti-6Al-4V, particularly in the aerospace sector and aluminium alloys 7475 and 5083 in other industries (MARTINEZ, 2012).

Within this range, superplastically deformed materials show a very high resistance against necking, so the material gets thinner in a uniform manner. Moreover, stresses to establish superplastic flow are low compared to conventional plastic flow. The main requirement for a material to behave superplastically is a fine grain size, which can vary from material to material between 1  $\mu\text{m}$  and 10  $\mu\text{m}$ . The grains should be randomly oriented in the material, so it behaves isotropically, and may not grow during plastic deformation, to maintain the superplastic properties throughout the entire forming process.

Much research has been carried out in order to achieve a better understanding of physical behaviour during superplastic deformation, as well as to apply superplasticity and superplastic forming successfully in industry (BARNES, 2007).

In general, superplasticity is defined as ability of polycrystalline materials to exhibit very high value of strain tensile elongation can be even more than 2000%, appearing in high homologous temperature under exceptionally low stress which is strongly dependent on strain rate (LI; TAN; LIEW, 2004; MOTYKA et al., 2007; PEARSON, 1934; RHAIPU, 2000; XING, 2004).

Superplasticity is characterized by a high elongation (ranging from a few hundred to several thousand percent) that can only be obtained in a narrow range of operating temperature and strain rate, as shown in the Figure 2 8.

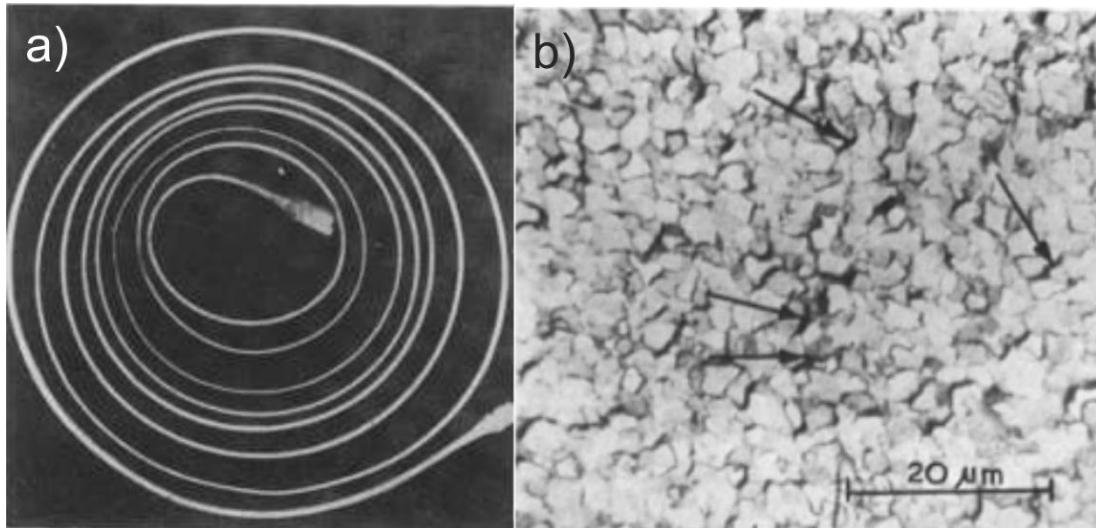


Figure 2-8 - Tensile specimens in superplastic state for polycrystalline materials: a) Pearson's famous test of a Bi-Sn alloy that undergone 1950 %. b) The structure extruded of titanium-lead eutectic alloy after superplastic strain of nearly 50% showing grain boundary offset (arrowed) (PEARSON, 1934).

The effect of superplastic forming process have a great versatility for manufacturing products (see Figure 2-9) (adapted from Bonet et al., 2006).

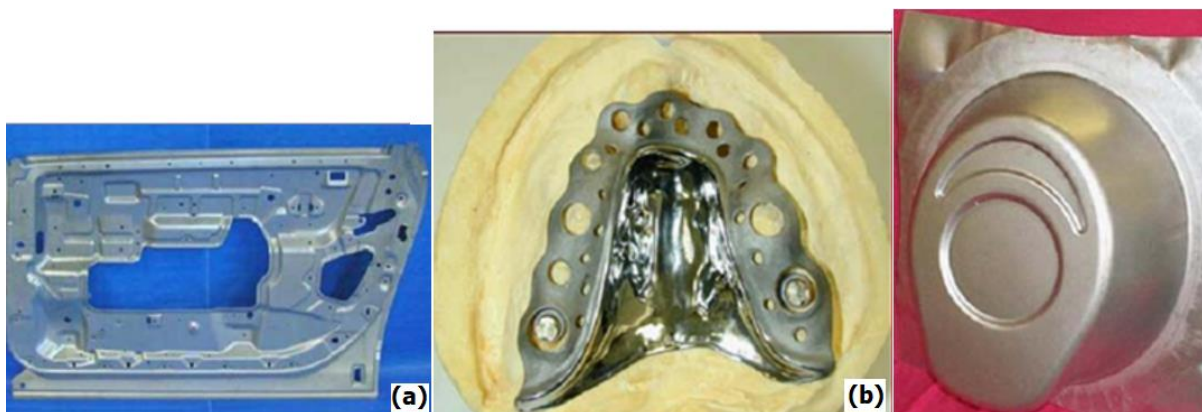


Figure 2-9 Some components based on titanium alloy: (a) automobile parts (b) prosthesis (c) blow test adapted from (Adapted from Bonet et al. 2006)

The effect of superplasticity is observed under deformations at high temperatures and low flow rates and is a consequence of the structural state of the metal. This structural state is characterized by a combination of several parameters, namely, the grain size, the structure of grain boundaries, the phase composition of the alloy, and the mechanical and crystallographic textures of the phases.

The formation of a finely disperse equiaxial structure in the material with the aim of obtaining long inter-grain surfaces that can provide uniform inter-grain slip over the volume, which makes a considerable contribution to plastic deformation, is very important for the effect of superplasticity (MUKHERJEE; ZELIN, 2004; PHAM, 2007; SIENIAWSKI; MOTYKA, 2007).

Generally, two types of superplasticity are distinguished: fine-structure superplasticity (FSS) – considered as an internal structural feature of material and internal-stress superplasticity (ISS) caused by special external conditions (e.g. thermal or pressure cycling) generating internal structural transformations that produce high internal stresses independent on external stresses.

- **Fine-Structure Superplasticity – FSS**

The term Fine Structure Superplasticity (FSS) is used to define the superplastic behaviour found in fine-grained materials deformed at temperatures above about 0.5 the absolute melting point of the material, where the deformation process can occur isothermally. This mechanism of superplasticity has been reported in metallic alloys, metal matrix composites, intermetallic, ceramics and ceramic matrix composites (RHAIPU, 2000). Although interest tends to shift toward the other material systems, e. g. high strain rate superplasticity in metal matrix composites, most research and exploitation has been in metallic alloys. It is believed (and proved up to some extent) that superplastic flow is dominated by a process which is called Grain Boundary Sliding (GBS) (MOTYKA et al., 2007). As the name suggests, boundary grains slide and this sliding is accommodated by means of some other mechanisms. These mechanisms are not completely understood yet, but the grain boundaries are known to play some important roles in superplasticity.

- **Internal Stress Superplasticity – ISS**

Internal stress superplastic materials exhibit large tensile elongation, e.g. 1400% tensile elongation to failure on a 6061-aluminium composite alloy (Al-20%SiC) under application small stress during thermal cycling. These materials deform by a slip creep process and they can have a strain rate of flow stress exponent ( $m$ ) defined before and mathematically describe by  $m = \frac{\partial \ln(\sigma)}{\partial \ln(\dot{\epsilon})}$ , and  $\sigma$  and  $\dot{\epsilon}$  are flow stress and strain rate, respectively) as high as unity and, hence, the materials can exhibit an ideal Newtonian viscous behaviour. ISS has been reported in pure iron, iron based alloys, commercially pure titanium and titanium-based composites during thermal cycling through a solid state allotropic transformation. ISS was also found in polycrystalline pure metals or single-phase alloys which exhibit anisotropic thermal expansion coefficients. Metal matrix composite materials such as SiC whisker-reinforced aluminium matrix composites and an Al<sub>2</sub>O<sub>3</sub> particle-reinforced zinc matrix composite, in which the thermal expansion coefficients of their constituents are different, were also found to exhibit ISS. The deformation behaviour of ISS materials could be very attractive in sheet and bulk forming since some of these materials e.g. metal matrix composites, are generally difficult to fabricate into useful products by conventional forming techniques.

#### 2.4.2. Deformation mechanism

In the Figure 2-10 evolution of the true flow stress ( $\sigma$ ) as a function of the strain rate ( $\dot{\epsilon}$ ) for materials with and without superplastic properties is illustrated. The slope of the  $\log \sigma - \log \dot{\epsilon}$  plot is denoted strain rate sensitivity  $m$ .

Superplastic occurs within region II due to the marked resistance to unstable neck development associated with the high strain rate sensitivity values exhibited within this deformation regime. There is a sharp drop in ductility at lower and higher strain rates associated with regions I and III (RHAIPU, 2000).

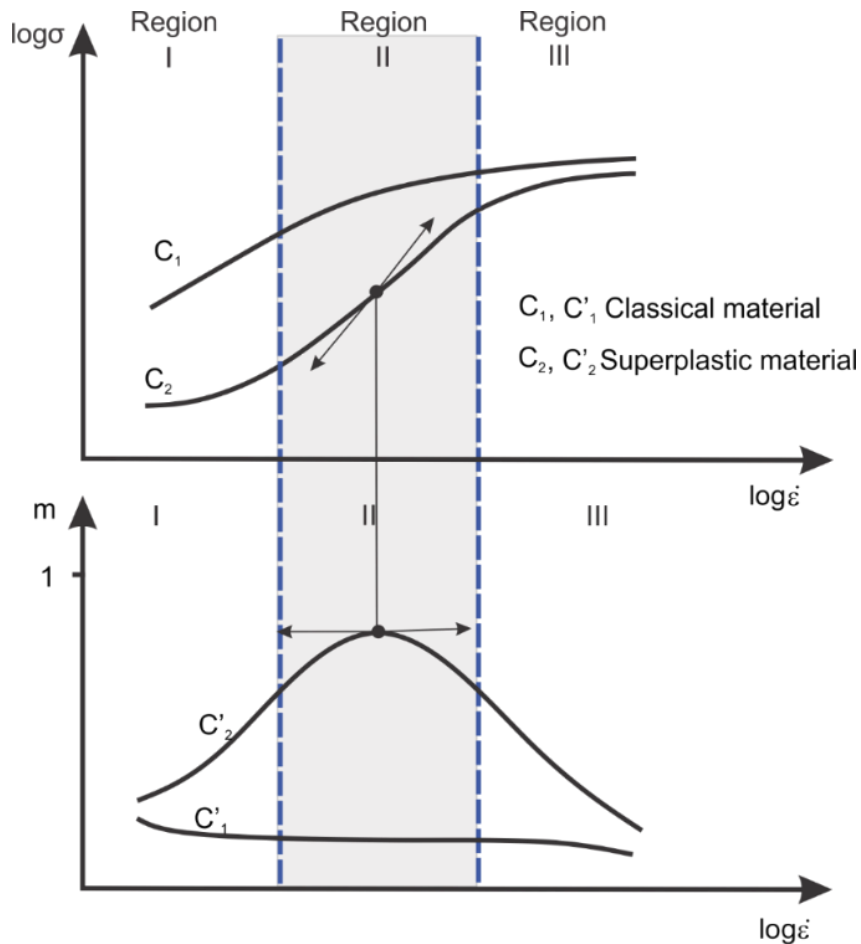


Figure 2-10 – Logarithmic plot of the dependence stress and strain rate for material with and without superplastic abilities (HAMILTON, 1984).

According to Rhaipu (2000), usually there are three main requirements for superplastic flow in metallic materials as following:

- The deformation temperature must be greater than approximately half the homologous melting point
- The material must have a fine stable grain size, typically less than 10  $\mu\text{m}$ .
- Low strain rate  $\sim 10^{-3} \text{ s}^{-1}$ .

If these three main conditions are fulfilled, the material will show a high strain rate dependence of flow stress commonly known as strain rate sensitivity ( $m$ ) which is characteristic of superplastic materials (see Figure 2-11). Then a high 'm' values normally occur from strain rate in the region  $10^{-3} \text{ s}^{-1}$  and usually greater 300% within the superplastic region (COMLEY, 2007; SHERBY; WADSWORTH, 1985).

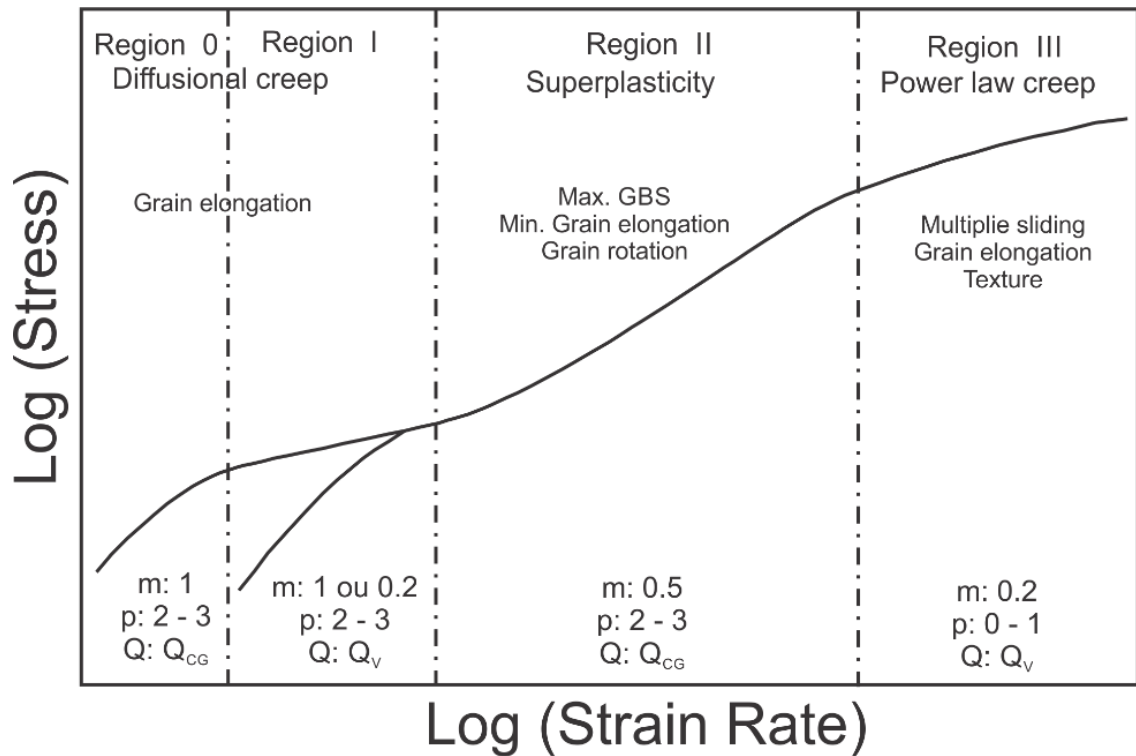


Figure 2-11 The region different deformation types adapted from Rhaipu (2000).

According to Rhaipu (2000), the ductility follows the same trends as the strain rate sensitivity such as the elongation increases with increasing temperature and decreasing grain size, and the optimum strain rate increases as the temperature is increased or grain size is decreased.

It is often observed that the strain rate at which the maximum strain rate sensitivity occurs and can be determined from the  $\log \sigma - \log \dot{\epsilon}$  curves, is not the same as that at which the maximum ductility is exhibited (RHAIPU, 2000).

With respect to these plots, region 1 corresponds to the diffusion creep, that is characterized by a transport of material via diffusion of atoms within the grains, and region 3 to the classical deformation by dislocation motion and climbing.

- **Superplastic deformation in region 2**

If grain boundary sliding was the only mechanism to occur in superplastic flow, then either the grains would have an ideal shape, such as a square, or huge cavities would occur in the material just before sliding takes place. Neither is the case. This means that in between the two-grain boundary sliding steps another mechanism is

responsible for this happening; it is called an accommodation mechanism (see Figure 2-12)

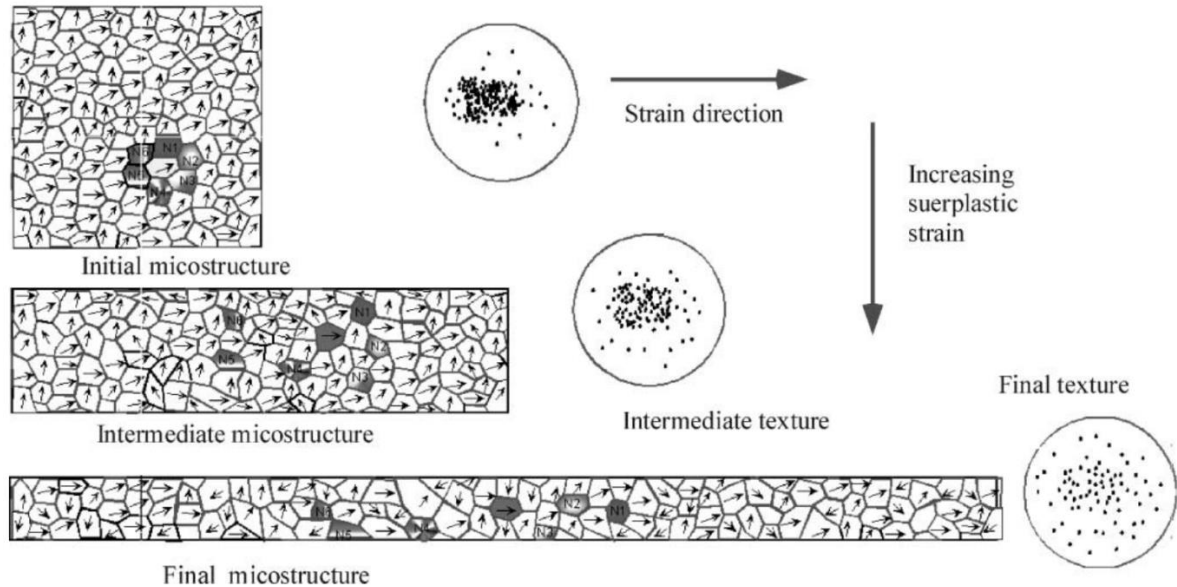


Figure 2-12 - Microstructure and texture evolution during strain increase (CHANDRA, 2002).

Two mechanisms will be discussed in this section, the diffusion creep and the intragranular slip. The mechanisms described are still under discussion, and it is also believed that grain boundary diffusion can be accommodated by partial melting in the boundary zone because of the elevated temperature.

The effect of all accommodation mechanisms is maintaining a coherent shape between the sliding grain boundaries without introducing large cavities. The accommodation mechanism builds up until a certain threshold stress. If this stress is reached, then cooperative grain boundary sliding will take place in a fraction of the time of the build-up period (LIU et al., 2009; SIEGERT; WERLE, 1994; YANG et al., 2016).

- **Diffusional creep**

This mechanism accommodation occurs by nucleation and coalescence of the creep cavitation generated at the  $\alpha$ - $\beta$  interfaces and it's necessary in order to achieve continuity at the grain boundaries. That would also enable a better understanding of the superplastic deformation mechanism in titanium alloys (ALABORT; PUTMAN; REED, 2015).

- **Intragranular Slipping**

If a slip plane arises inside a grain, then this is called intragranular slip. An extra boundary can grow inside this grain due to a collective movement of dislocations, which can assist in the mechanism of cooperative grain boundary sliding. Such a dislocation line inside a grain will then be collinear with the favourable sliding path. Intragranular slip is not seen in every superplastic material, this is especially seen in materials based on Al-Mg.

### 2.4.3. Superplastic behaviour of Ti-6Al-4V

According to Vanderhasten (2008), the evolution of the stress-strain ( $\sigma$ - $\epsilon$ ) curves of superplastic Ti-6Al-4V as function of temperature is presented in the Figure 2-13 for a strain rate of  $5 \cdot 10^{-4} \text{ s}^{-1}$ . Starting from 725 °C, a sample deformed slowly in tension reaches large elongation and a true plastic strain higher 1.3.

The maximum elongation is observed at temperatures between 800 °C and 850 °C and strain rate of  $5 \cdot 10^{-4} \text{ s}^{-1}$ . Superplasticity is most surely active and grain boundary sliding can be supposed to be dominant.

When the grain size increases, the effectiveness of those mechanisms will be more difficult because the volume to be accommodate becomes larger, thus resulting in an increasing flow stress as can be seen in Figure 2-13.

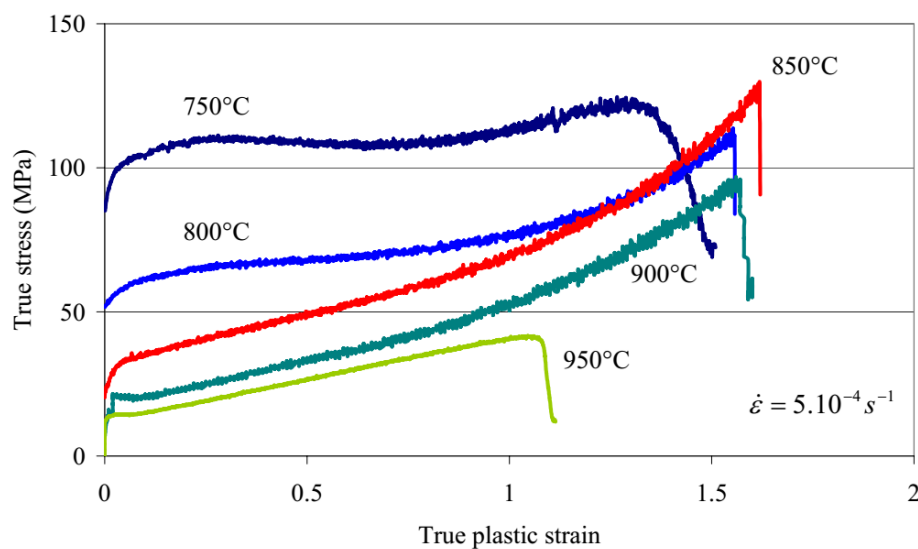


Figure 2-13 – True stress-true plastic strain curves of Ti-6Al-4V flat specimens tested between 750 °C and 950 °C and a strain rate of  $5 \cdot 10^{-4} \text{ s}^{-1}$  (VANDERHASTEN, 2008)

According to Vanderhastén (2008), the strain rate can determine the mechanism of deformation as shows Figure 2-14: deforming too fast can (i.e.  $0.05 \text{ s}^{-1}$ ) cause for instance the suppression of grain boundary sliding. But also, if the observations are limited to the superplastic domain, the influence of strain rate is observed. These tests performed at  $800^\circ\text{C}$  between  $0.005$ ,  $0.001$  and  $0.0005 \text{ s}^{-1}$  are all superplastic but the shape of the  $\sigma$ - $\epsilon$  curves is different.

Two main reasons are highlighted: Higher strain rate cause higher grain growth rate but the absolute grain size for a same strain level is larger at lower strain rate due to longer exposure time. So, hardening caused by dynamic grain growth is more pronounced for the test at  $0.0005 \text{ s}^{-1}$ . Secondly, strain rate has also an influence on the acting grain boundary sliding accommodation mechanism; at higher strain rate dislocation activity is preferred while at lower strain rate diffusion is dominant.

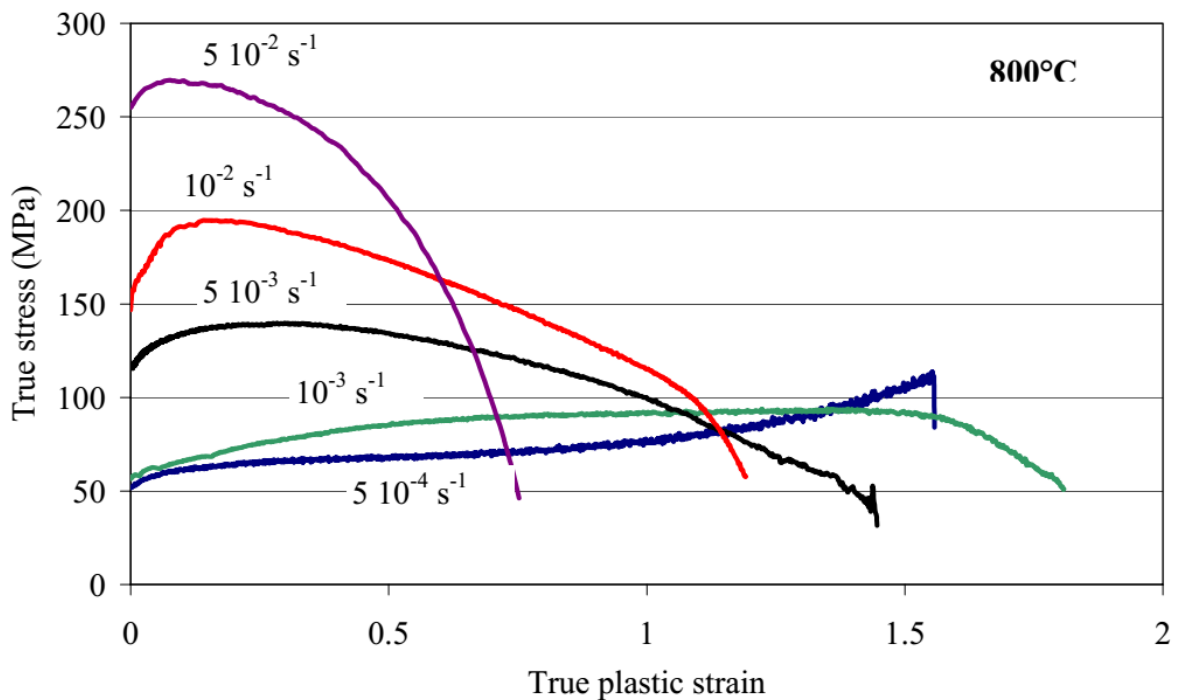


Figure 2-14 – True stress-true plastic strain of Ti-6Al-4V flat specimens tested at  $800^\circ\text{C}$  and at strain rate between  $5 \cdot 10^{-2} \text{ s}^{-1}$  and  $5 \cdot 10^{-4} \text{ s}^{-1}$  (VANDERHASTEN, 2008)

Superplastic materials show a very high sensitivity in mechanical properties, especially the flow stress, with respect to the strain rate. Temperature is an important aspect as well.

#### 2.4.4. Industrial applications

Titanium is a widely-used aerospace, marine, and structural material because of its high specific strength, fracture toughness, elastic modulus and resistance to corrosion characteristics. Titanium alloys are also used for cryogenic applications where the chemical resistance and strength behaviour at low temperatures make them more suitable than bcc materials (JOSHI, 2006)

Although the wide range of materials in which superplasticity has been investigated, the commercial exploitation of the phenomenon still has concentrated on the sheet forming of aluminium and titanium alloys with micro duplex stainless steel and eutectoid Zn-22%Al occasionally used (BELLET ET AL. 2010; MAY 2009; SIENIAWSKI and MOTYKA 2007).

The titanium alloy Ti-6Al-4V alloys is highly superplastic and unlike Aluminium does not significantly cavitation during superplastic forming. It also readily diffusion bonds at temperatures in the superplastic range so that forming and bonding can often be carried in the same operation and complicated internally stiffened components can be produced from layup of several sheets (INGELBRECHT, 1985).

Table 2-3 Strain rate sensitivity and activation energy of Ti-6Al-4V alloy as reported by previous researchers for various starting microstructure under different temperature-strain rate Conditions (ROY; SUWAS, 2013). The Table 2-3 summarizes results obtained by previous researchers for strain rate sensitivity index (m).

Table 2-3 – Strain rate sensitivity and activation of Ti-6Al-4V (ROY; SUWAS, 2013).

Source Reference	Material	Deformation condition	Deformation mechanism	m	Energy activation	
(SESHACHARYULU et al., 1999)	ELI Grade Ti-6Al-4V with Widmanstätten type microstructure	T= 850–950 °C; $\dot{\epsilon}=10^{-3} - 10^{-1} \text{ s}^{-1}$ ;	Globularization of $\alpha$ lamellae	0.22	453	
		T= 950 - 1100 °C; $\dot{\epsilon}=3 \times 10^{-3} - 100 \text{ s}^{-1}$	Large grained super-plasticity in $\beta$ phase (LGSP)	0.33		
	Commercial Ti-6Al-4V with equiaxed $\alpha$ - $\beta$ microstructure	T= 750–1000 °C; $\dot{\epsilon}=3 \times 10^{-4} - 100 \text{ s}^{-1}$ ;	Fine-grained super-plasticity	0.28	330	
		T= 1000–1100 °C; $\dot{\epsilon}=10^{-4} - 100 \text{ s}^{-1}$ ;	Dynamic recrystallization ( $\beta$ -phase field)	0.28	210	
	Commercial Ti-6Al-4V with lamellar starting structure	T= 800-975 °C; $\dot{\epsilon}=3 \times 10^{-4} - 10^{-2} \text{ s}^{-1}$ ;	Globularization of $\alpha$ lamellae	0.28	455	
		T= 1000–1100 °C; $\dot{\epsilon}=10^{-3} - 10^{-1} \text{ s}^{-1}$ ;	Dynamic recrystallization ( $\beta$ -phase field)	0.28	172±10	
	SEMIATIN; SEETHARAMAN; WEISS, 1999	Ti-6Al-4V with $\alpha$ colony microstructure	T= 815–955 °C; $\dot{\epsilon}=10^{-3} - 10 \text{ s}^{-1}$ ;	Globularization of $\alpha$ lamellae	0.25	
		Ti-6Al-4V with $\alpha$ colony microstructure ( $\beta$ grain size ~ 2000 $\mu\text{m}$ )	T= 750-900 °C; $\dot{\epsilon}=10^{-3} - 10^{-1} \text{ s}^{-1}$ ;	Dynamic recovery	0.13	265
T= 750–900 °C; $\dot{\epsilon}=1 - 10 \text{ s}^{-1}$ ;			DRx Instability formation	0.1	390	
T= 900–1000 °C; $\dot{\epsilon}=10^{-3} - 10^{-1} \text{ s}^{-1}$			Globularization, DRx, grain boundary sliding	0.3	350	
T= 900–1000 °C; $\dot{\epsilon}=1 - 10 \text{ s}^{-1}$ ;			Globularization, DRx, grain boundary sliding	0.25	370	
Ti-6Al-4V-0.1B with $\alpha$ colony microstructure ( $\beta$ grain size ~300 $\mu\text{m}$ )		T= 750–900 °C; $\dot{\epsilon}=1 - 10 \text{ s}^{-1}$ ;	Dynamic recovery, grain boundary sliding	0.12	200	
		T= 750–900 °C; $\dot{\epsilon}=1 - 10 \text{ s}^{-1}$ ;	Globularization, DRx,	0.1	410	
		T= 900–1000 °C; $\dot{\epsilon}=10^{-3} - 10^{-1} \text{ s}^{-1}$ ;	Globularization, DRx, grain boundary sliding	0.2	480	
		T= 900–1000 °C; $\dot{\epsilon}=1 - 10 \text{ s}^{-1}$ ;	Globularization, DRx, grain boundary sliding	0.2	420	

Farias (2015) has reported on his work one main advantages of superplastic forming or the combined forming/diffusion bonding (SPF/DB) forming fabrication processes have already been successfully applied to several demonstration and production savings aerospace components with cost savings up to 50% and weight with up to 30% compared conventionally produced titanium parts. These savings are achieved because fewer fasteners are required, much machining is eliminated and more structurally efficient designs are possible.

Titanium SPF/DB components can also economically replace Aluminium or steel parts in some cases. Titanium sheet forming are almost always carried out using argon gas pressure and female die.

Superplastic forming differs from cold sheet forming in several ways. The  $m$  value has an important play role due usually to assign most important factor in promoting large elongation and allowing design changes. See Figure 2-15.

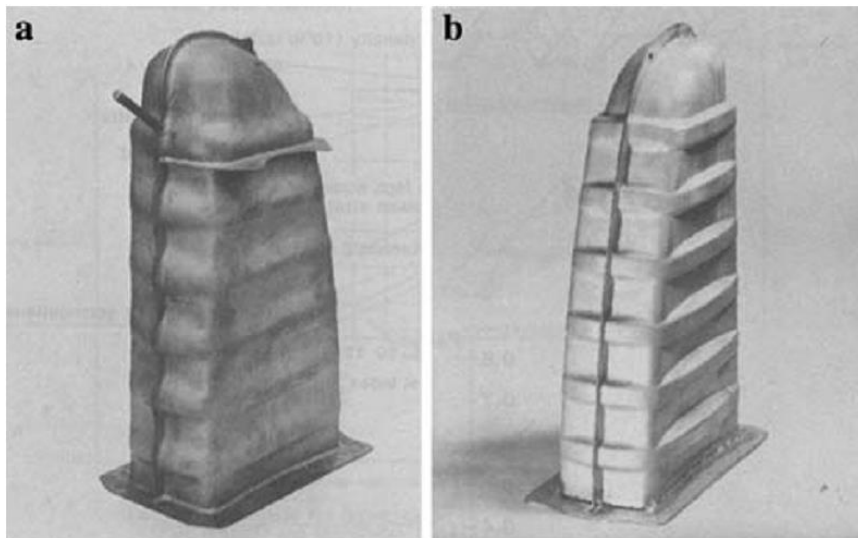


Figure 2-15 (a) Conventionally fabricated 'old design' and (b) SPF Ti-6Al-4V new design first superplastic formed commercial titanium application (1981) (Adapted from Barnes, 2007).

Most applications of superplastic titanium alloys are in aerospace (civil, military and space) and in several industrial applications as petrochemical, offshore, subsea and building structures.

## 2.5. SUPERPLASTIC BEHAVIOUR MODELLING

In the present section will be present main superplastic behaviour modelling approach such as constitutive equations, classical models and evolution and practice for testing procedure applied into hot tensile test.

### 2.5.1. Classical models and evolution

The plasticity phenomenon at high temperature in polycrystalline material can be described by the well-known MBD (Mukherjee-Bird-Dorn) Equation proposed by Mukherjee (2002), which has been used more than three decades and showing good results with materials as metallic alloy, intermetallic, ceramic and tectonic system. General MBD form is written as:

$$\dot{\epsilon} = C_1 D \left( \frac{b}{d} \right)^p \left( \frac{\sigma}{G} \right)^n \quad (2-1)$$

Where:

- $\dot{\epsilon}$  = Stationary strain
- $C_1$  = non dimensional
- $G$  = shear moduli (MPa)
- $b$  = Burgers vector ( $\mu m$ )
- $k$  = Boltzmann constant ( $1.381 \times 10^{-23} J / K$ )
- $T$  = absolute test temperature (K)
- $d$  = medium grain size ( $\mu m$ )
- $p$  = converse grain size exponent
- $\sigma$  - applied stress (MPa)
- $n$  - stress exponent =  $d \text{Log} \dot{\epsilon} / d \text{Log} \sigma = 1/m$
- $D$  - diffusion coefficient written as:

$$D = D_0 \exp \left( \frac{-Q_c}{RT} \right) \quad (2-2)$$

Where:

- $D_0$  – diffusion frequency coefficient ( $m^2/s$ )
- $Q_c$  – activation energy of creep process (kJ/mol)
- $R$  - gas constant (8.314 J/(mol.K))

The Equation MBD aggregates parameters obtained from both tensile and creep tests. Critical parameters to any material and creep test condition are:  $n$  (stress exponent),  $Q_c$  (activation energy) and  $p$  (converse grain size ( $d$ ) exponent).

A threshold stress ( $\sigma_0$ ) value could be added to Equation (2-1), then modified to creep power law as:

$$\dot{\varepsilon} = A.D \left( \frac{Gb}{kT} \right) \left( \frac{\sigma - \sigma_0}{G} \right)^n \quad (2-3)$$

Where:

$A$  – constant dependent mechanism;

$\sigma_0$  – threshold stress;

Constitutive model used to describe relation between flow stress ( $\sigma$ ), deformation ( $\varepsilon$ ) and strain rate ( $\dot{\varepsilon}$ ) is named power law or Ludwick equation, which could be obtained from MBD equation rewritten in form (Júnior 2009; Sablik et al. 2005):

$$\sigma = K.\dot{\varepsilon}^m \varepsilon^n \quad (2-4)$$

Where:

$\sigma$ – effective flow stress;

$\dot{\varepsilon}$  – effective strain rate;

$\varepsilon$  – effective deformation,

$m$  – strain rate sensitivity exponent;

$n$  – strain hardening exponent;

$K$ –constant composed with data obtained of hot tensile test.

At high temperature plastic regime, the  $n$  (strain hardening exponent) influence is very small and  $m$  (strain rate sensitivity of flow stress exponent) influence starting to be dominant let Ludwick Equation related to expression:

$$\sigma = C.\dot{\varepsilon}^m \quad (2-5)$$

Where

C – constant function of temperature;

m – strain rate sensitivity exponent, represents the slope of the logarithmic plot.

The most important mechanical characteristic of superplastic material is m exponent, to strain rate ( $\dot{\epsilon}$ ) related through Equation (2-5), obtained with hot tensile test data, which tend to form a sigmoidal or three stages curve. Region I, shows low ( $\dot{\epsilon}$ ) and m values; at region II  $\dot{\epsilon}$  and m values are high in superplastic regime, and at region III ( $\dot{\epsilon}$ ) and m are low (as seen in Figure 2-11).

If stable strain rate measurements are obtained Equation (2-3) can in a second stage be rewritten in the form ( $\dot{\epsilon}$ ) as function of ( $\sigma$ ) with creep test data related through MBD Equation as:

$$\dot{\epsilon} = A.D.\left(\frac{b}{d}\right)^p\left(\frac{\sigma}{E}\right)^n \quad (2-6)$$

Where:

A – material coefficient

E – elasticity module,

with (C) constant, related through equation:

$$\dot{\epsilon} = C.\sigma^n \quad (2-7)$$

Where:

C – constant =  $(1/C)^{1/m}$

n – stress exponent =  $1/m$  presented by slope of logarithmic plot.

In the Table 2-4 are reported a brief summary of superplastic behaviour models based upon study initially performed in Western and continued in Eastern (Soviet Union) in forties.

Table 2-4 - summary of superplastic behaviour evolution models.

Author	Concept	Constitutive equation
(BACKOFEN; TURNER; AVERY, 1962)	At this field with proposal and proved that behaviour of superplastic alloy result of high strain rate sensitivity with flow stresses (m). K and m are constant, the equation is used at simple tensile state without effect of deformation (n=0). It was a first exhibition of potential superplasticity use in simple forming operation	$\sigma = K \cdot \dot{\epsilon}^m$ $m = \frac{\left( \log \left( \frac{P_b}{P_a} \right) \right)}{\left( \log \left( \frac{V_2}{V_1} \right) \right)}$
(Gibbs 1967)	showed an initial procedure of m calculation using load values to change volume constant, immediately before (point d) and after (point e)	$m = \frac{\left( \log \left( \frac{P_e}{P_d} \right) \right)}{\left( \log \left( \frac{V_2}{V_1} \right) \right)}$
(ROSSERD, 1966)	added characteristic of strain rate strength and (n) strain hardening exponent to superplastic forming.	$\sigma = K \dot{\epsilon}^m \epsilon^n$
(Ball & Hutchison 1969)	Grain boundary sliding (GBS) process through dislocation climb.	$\dot{\epsilon} = K_4 \left( \frac{d}{d} \right)^2 D_{gb} \left( \frac{\sigma}{E} \right)^2$
(Hart 1970)	procedure of m calculation which the crosshead speed is interrupted at S point, then true stress values are estimated in different points alongside relaxation curve, m is determined through slope plot of log $\sigma$ with log $d\sigma/dt$ .	$m = \frac{\partial \ln \sigma}{\partial \ln (d\sigma/dt)}$
(LANGDON, 1970)	Dislocation of climb and glide.	$\dot{\epsilon} = K_4 \left( \frac{d}{d} \right)^2 D_L \left( \frac{\sigma}{E} \right)^2$
(Mukherjee 1971)	controlled rate of sliding by dislocation climb GBs.	$\dot{\epsilon} = K_2 \left( \frac{d}{b} \right)^2 D_{gb} \left( \frac{\sigma}{E} \right)^2$
	rate controlled by diffusional accommodation.	$\dot{\epsilon} = K_{14} \left( \frac{d}{b} \right)^2 D_{eff} \left( \frac{\sigma - \sigma_0}{E} \right)$
(Mukherjee 1975)	change of original rate controlled by GBS /dislocation climb/glide model	$\dot{\epsilon} = K_3 \left( \frac{d}{b} \right)^2 D_{gb} \left( \frac{\sigma}{G} \right)^2$
(Arieli & Rosen 1976)	Procedure to m calculation which true $\sigma$ and $\dot{\epsilon}$ values are calculated in several points alongside load x time curve thus is plot log $\sigma$ with $d\epsilon / dt$ .	$m = \frac{\partial \ln \sigma}{\partial \ln (d\epsilon/dt)}$
(GIFKINS, 1976)	pile-up sliding at Grain Boundary.	$\dot{\epsilon} = K_5 \left( \frac{b}{d} \right)^2 D_{gb} \left( \frac{\sigma}{E} \right)^2$

Source: Adapted from Guanabara Júnior (2009)

This represents the initial or classic structural superplasticity approach, since the superplastic deformation and its material parameters optimization are useful as a tool to provide a good understanding about the superplastic forming of components. This is applied with high ( $\dot{\epsilon}$ ), both high and low temperature showing application in metal and nanocrystalline alloy, among other materials as: ceramics, composites, intermetallic, metallic glass.

More advanced models including static and dynamic grain growth during are addressed in chapter 5.

### 2.5.2 Testing procedures

Hot tensile test is the most commonly used test procedure to get data for superplastic material model parameter identification. Optimum testing procedure corresponds to a constant strain rate testing procedure that requires a continuous change in crosshead speed during the test. Modern tensile testing equipment's allow today such procedures to be conducted as standard procedures. Tensile tests are conducted at increasing temperatures and strain rates. In such conditions, the common relationship for hot deformation of metallic materials is also true for SPF materials as following Equation (2-8).

$$\sigma = A \cdot \epsilon^n \cdot \dot{\epsilon}^m \quad (2-8)$$

Assuming that during hot forming the term  $\epsilon^n$  tends to 1 and correspondingly the strain hardening exponent  $n$  to 0, the flow stress only depends on the strain rate considering a constant factor  $A$ .

In arbitrary necking occurs at an incidental position, the "dynamic strain hardening", characterized by the exponent  $m$ , then causes an increase in flow stress and thus stabilizes the potential necking area. Local necking is suppressed, and the specimen is homogeneously strained further along its entire gauge length.

Analysis of these curves allows the plot  $m$  value diagrams are shown in Figure 2-16. To determine the  $m$ -value, a stepped strain test is also often chosen Figure 2-17. During the test, the strain rate is step-wise increased, always after a short period of constant strain rate.

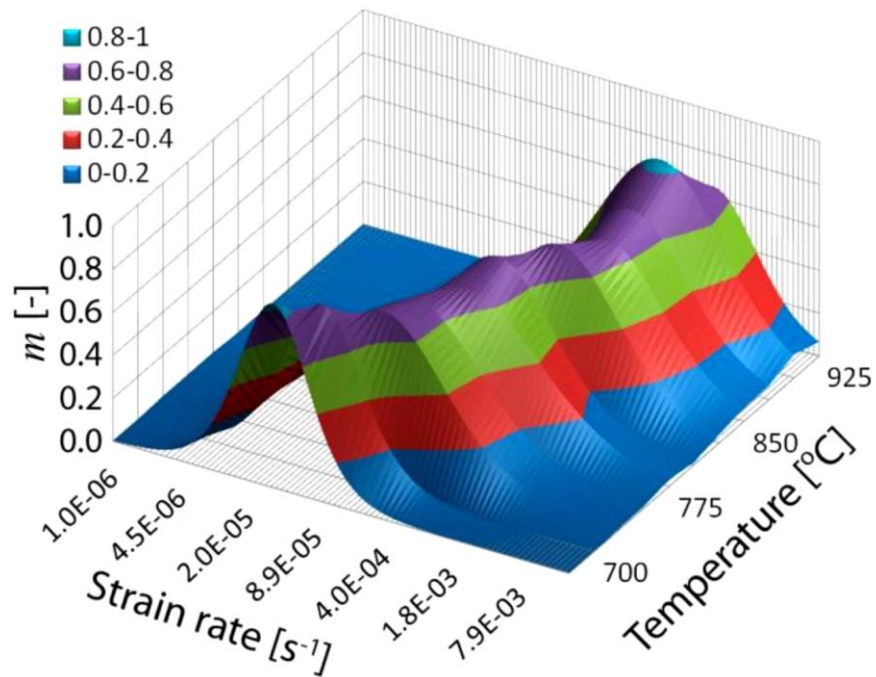


Figure 2-16 Evolution of  $m$  with respect to strain rate and testing temperature (Aksenov, S.; Chumachenko, E.; Logashima 2012)

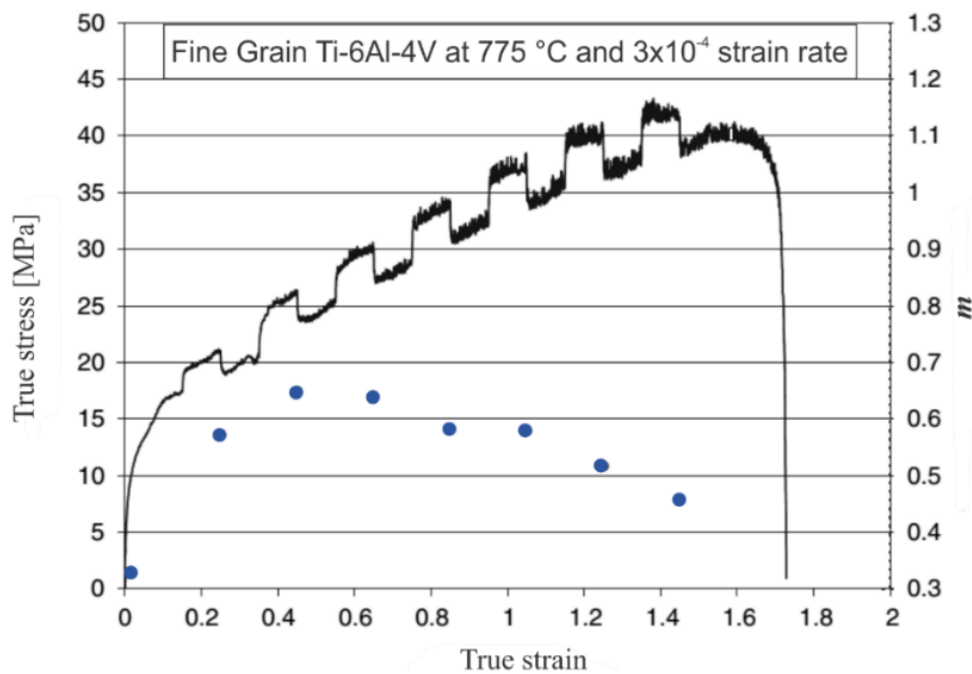


Figure 2-17 - Stepped strain test and determination of strain-rate sensitivity index ( $m$ ) value (COMLEY, 2007c).

### 3. MATERIAL, EQUIPMENT AND EXPERIMENTAL PROCEDURE

In this chapter, it will be described the material, procedure and methodology for the mechanical and microstructural characterizations carried out in this work. It includes heat treatment, tensile tests under both superplastic and hot work conditions as well as SEM observations associated to image analysis.

#### 3.1. MATERIALS

In this work, three TA6V4 sheets characterized by an equiaxed ( $\alpha+\beta$ ) microstructure and by respectively three different initial  $\alpha$  grain sizes are studied (Table 3-1):

- a sheet (sheet 1) examined was donated by EMBRAER to the Polytechnic School of Engineering of the University of Sao Paulo. It has a thickness of 2 mm and a grain size of 4.9  $\mu\text{m}$
- a sheet from the École des Mines d'Albi-Carmaux (sheet 2), supplied by AIRBUS, with a thickness of 4 mm and a grain size of 3  $\mu\text{m}$
- one sheet from the University of Kagawa in Japan (Sheet 3) with a thickness between 1.4 mm and 3 mm. It was obtained by doing on sheet 2 a solution heat treatment followed by a quenching in ice water to obtain the single  $\alpha'$  martensite. Then this Ti-6Al-V4 plate, having a single  $\alpha'$  martensite microstructure with an initial thickness of 4 mm, was hot-rolled at a strain rate (rolling speed) of approximately 7  $\text{s}^{-1}$  to get thicknesses ranging from 1.4 mm to 1.0 mm. Finally it provides a plate with an average grain size of 0.5  $\mu\text{m}$  named Ultrafine-Grained Microstructure (UFGM) (MATSUMOTO; VELAY; CHIBA, 2015) –

Table 3-1: Chemical composition (wt. %) for each Ti–6Al–4V sheet as-received.

Start Microstructure Grain size ( $\mu\text{m}$ )	Chemical composition (wt. %)					Thickness (mm)
	Ti	Al	V	Ca	O	
4.9 $\mu\text{m}$ (sheet 1)	Balance	6.41	4.32	0.004	0.15	2
3.0 $\mu\text{m}$ (sheet 2)	Balance	6.50	4.24	0.004	0.17	4
0.5 $\mu\text{m}$ (sheet 3)	Balance	6.50	4.24	0.004	0.17	1

Note that Sheet II and I ( Figure 3-1b and Figure 3-1c) starting microstructure (SM), belong to the Ti-6Al-4V alloy the most widely used by industrials to carry out Superplastic Forming (SPF). It considers equiaxed ( $\alpha+\beta$ ) Ti-6Al-4V alloy with an average  $\alpha$  - phase grain size equal to 3  $\mu\text{m}$  (sheet 2) and 4.9  $\mu\text{m}$  (sheet 3), respectively.

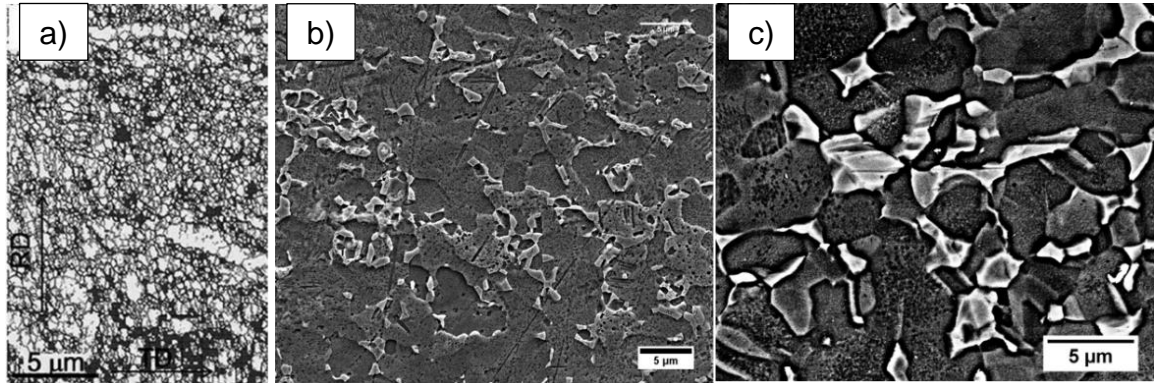


Figure 3-1 - Grain Size Starting microstructure: 0.5  $\mu\text{m}$  ultra-fined-grained (a); fined-grain 3.0  $\mu\text{m}$  and (b) and fined-grain 4.9  $\mu\text{m}$  (c).

Based on their microstructure the sheets I, II and III were classified respectively as a fined-grain microstructure (for grain size of 3.0 and 4.9  $\mu\text{m}$ ) and as an ultra-fined grain microstructure (for a grain size of 0.5  $\mu\text{m}$ ).

### 3.2. TENSILE TESTS AT HIGH TEMPERATURE

Mechanical tests were carried out at several temperatures and under different strain rate using mainly two equipment: a Gleeble machine for hot working conditions (high temperature and strain rate between  $10^{-1} \text{ s}^{-1}$  and  $10^{-3} \text{ s}^{-1}$ ) and a MTS 50kN for superplastic conditions (high temperature and strain rate between  $10^{-2} \text{ s}^{-1}$  and  $10^{-4} \text{ s}^{-1}$ ).

#### 3.2.1. Samples

Two different geometries of the specimen were used, respectively, for tensile test on the Thermomechanical machine Gleeble and the MTS 50 kN. These specimens were manufactured regarding the specifications of each machine and test goals.

The first type, shown on the Figure 3-2 with its dimensions' characteristics, was used for the tests done on the thermomechanical simulator model "the Gleeble 3800". The second type specimen was used for the superplastic tests carried out on the MTS machine (see Figure 3-3)

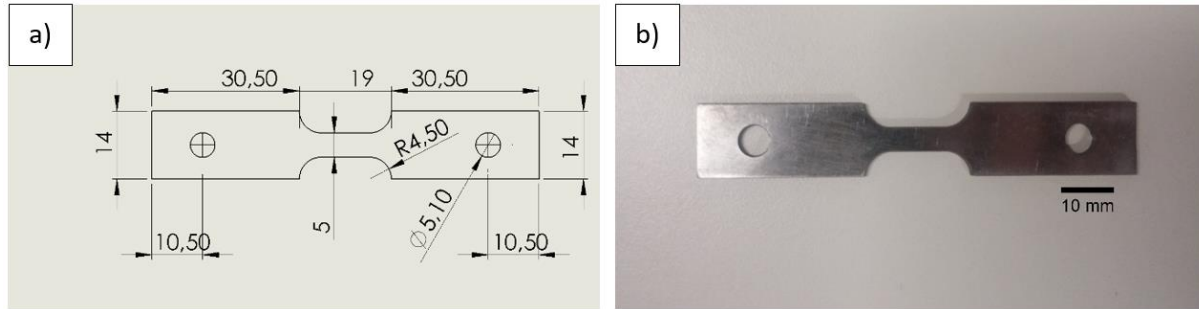


Figure 3-2: Technical draw of specimen for thermomechanical test (a) and machined specimen aspect (b)

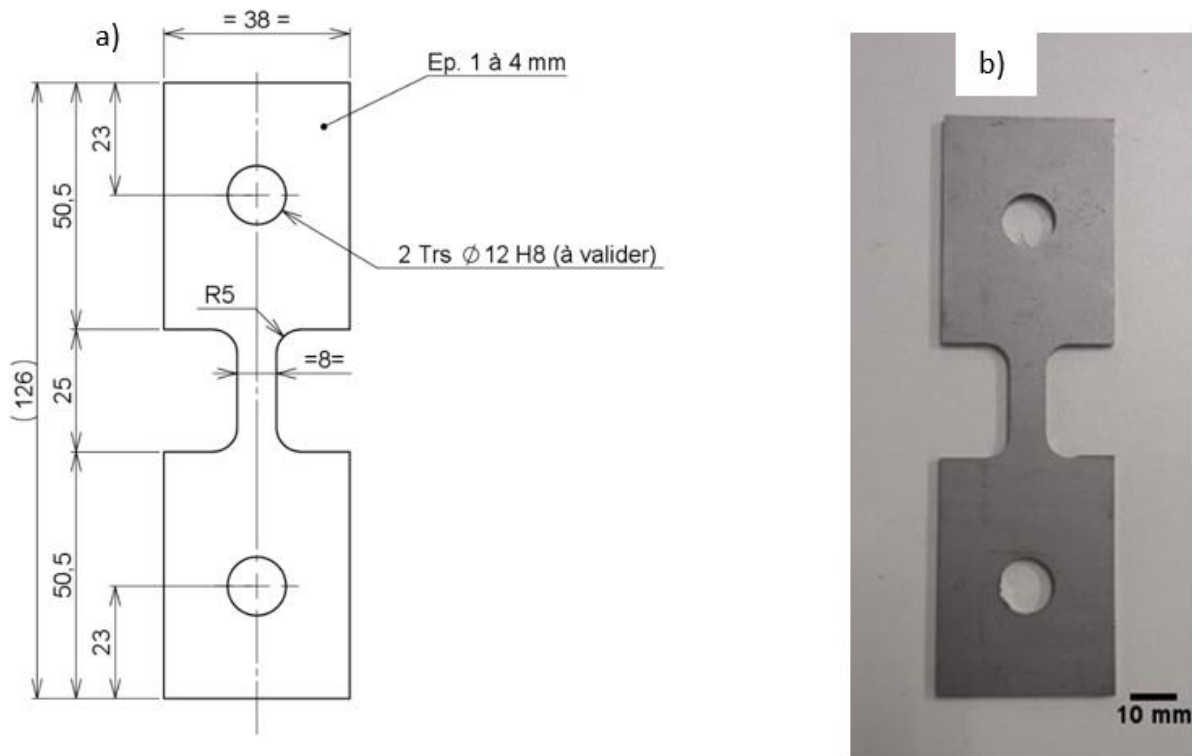


Figure 3-3 – Specimen for superplastic test at high temperature: and specimen technical draw (a) machined specimen (a)

### 3.2.2. Mechanical Tests on the Gleeble equipment

The mechanical test procedure taken account on the Gleeble is presented from following section such as set up conditions test, the specimen type and the other materials used during the tests.

#### 3.2.2.1 The Gleeble

A Gleeble is a dynamic test machine that can simulate a wide variety of mechanical metallurgical situations.

The direct resistance heating system of the Gleeble 3800 can heat specimens at rates of up to 10,000 °C/second, or can hold steady-state equilibrium temperatures. High thermal conductivity grips hold the specimen, making the Gleeble 3800 capable of high cooling rates. An optional quench system can achieve cooling rates more than 10,000°C/second at the specimen surface.

A Gleeble 3800 thermo-mechanical simulator, located at Brazilian Synchrotron Light Laboratory LNL member of Brazilian Centre for Physics Research (CBPF)<sup>1</sup>, was used for the characterization of equiaxed Ti-6Al-4V alloys Tests were performed using a Mobile Conversion Unit (MCU).



Figure 3-4: Gleeble 3800 MCU for tensile test – (LNL- Brazil courtesy)<sup>1</sup>

---

<sup>1</sup> Website: <http://lnnano.cnpem.br/>

Tensile tests on the Gleeble 3800 machine was used to determine the stress-strain behaviour at high temperature (from 700 °C to 950 °C) and high strain rate ( $10^{-1}$ ;  $10^{-2}$  and  $10^{-3} \text{ s}^{-1}$ ) as shown on the Figure 3.5.

The elastic properties are assessed using tensile test under small deformation conditions. In order, to obtain accurate values of the Young moduli, an extensometer is used to calculate the deformation. However, at these temperatures, the small values of the yield strength make these measurements difficult.

Isothermal constant-strain-rate tension tests were performed for determine the plastic flow behaviour and accompanying microstructure evolution for the few minutes under load control (to prevent buckling) and soaked at temperature for 2 minutes before testing under stroke control. Most tests were done in mode true strain of approximately 0.5. Because of the 5.0 mm maximum crosshead travel of the system (corresponding to an average axial strain of about 1.0), only a few tests could be taken to failure with the current sample design.

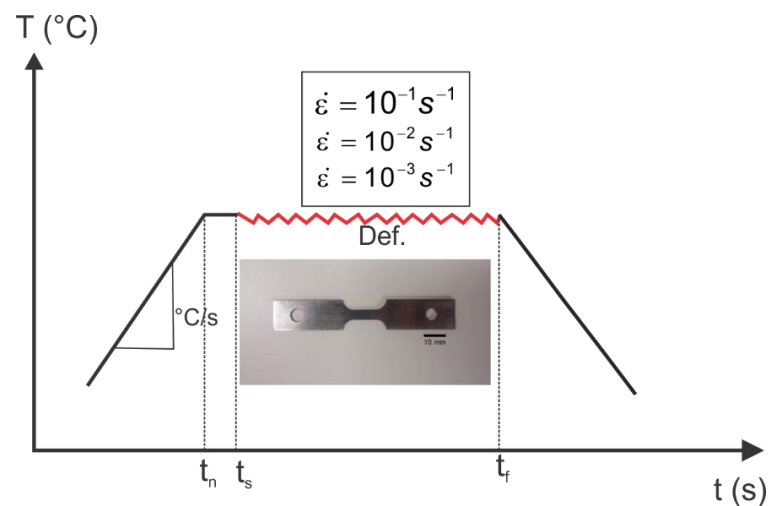


Figure 3-5 – Thermal cycle for tensile test planning with values for strain rate thermomechanical parameters for testing time vs temperature and sample specimen.

The sample was mounted within a chamber, which can be vacuum pumped or gas filled. Minimum pressure on the chamber is  $10^{-4}$  Torr; for the tests vacuum was set to  $5.6 \times 10^{-1}$  Torr. The physical simulator has a hydraulic system with load capacity of 100 kN (10 tons) in traction with 0.1 kN resolution. Heating was done by the Joule

effect, which provides heating rates of up to 5 °C/s. For cooling, the machine counts with copper claws favouring the accelerated cooling and accessories enabling to use inert gas Argon to 5 °C/s.

At the start of the test, the specimen was deformed to 20% elongation within region II, if we considering the different region for deformation types present in the Figure 2-11. The crosshead velocities were  $10^{-1}$ ,  $10^{-2}$  and  $10^{-3}$  s<sup>-1</sup>. True stresses were calculated at each crosshead velocity from the measured load and from the instantaneous cross-sectional area which was calculated by  $s = (s_0 L_0) / L$ , if we consider a volume conservation in the four specimens geometry tested.

The temperature can be measured by two types of thermocouples: the thermocouple type SP10-R-008 or the Platinum vs Platinum 10%-Rhodium thermocouple. For the test requiring a precision in displacement, an extensometer was used with an operating range: 0 ° to 1450 °C as show in the Figure 3.6. The temperature testing range was from 700 °C to 950 °C.

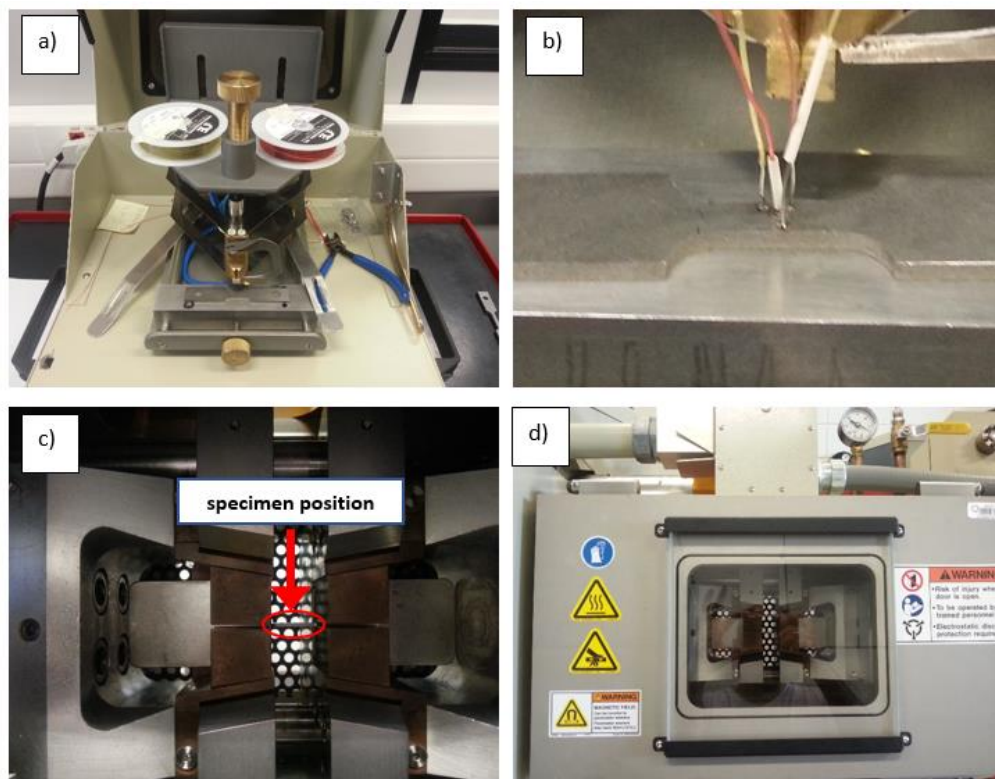


Figure 3-6: Setup for uniaxial tensile test at Gleeble® 3800: welder machine (a); Thermocouple wire type S (Platinum (–) vs. Platinum 10% Rhodium (+)) (b); the specimen position in detail (c) and chamber test; test execution.

### 3.2.2.2 Tensile tests conditions (Geeble)

Tensile tests at several temperatures were conducted on a Gleeble 3800 testing machine at a strain rate of  $10^{-1}$ ,  $10^{-2}$  and  $10^{-3}$  s $^{-1}$  on samples with a starting grain size of 4.9  $\mu\text{m}$ .

Table 3-2: Matrix for hot work (HW) test at high temperature

N° Specimen	Temperature (°C)	$\dot{\epsilon}$ (s $^{-1}$ )
HW1	600	$10^{-1}$
HW2		$10^{-2}$
HW3		$10^{-3}$
HW4	700	$10^{-1}$
HW5		$10^{-2}$
HW6		$10^{-3}$
HW7	800	$10^{-1}$
HW8		$10^{-2}$
HW9		$10^{-3}$
HW10	850	$10^{-1}$
HW11		$10^{-2}$
HW12		$10^{-3}$
HW13	950	$10^{-1}$
HW14		$10^{-2}$
HW15		$10^{-3}$

### 3.2.3. Mechanical tests on the Servo-machine MTS 50 kN

#### 3.2.3.1 The MTS 50 kN

The mechanical tensile tests were performed using a servo-hydraulic testing machine and a furnace accurate for the very large elongations (see Figure 3-7).

It includes three heating zones controlled by S- thermocouples and allows to maintain a constant temperature during all the sample deformation. As the use of a

classical extensometer was not possible due to the very large elongation, a nonlinear crosshead displacement can be considered in order to obtain a constant target strain rate  $\dot{\epsilon}$  at the middle of the specimen (COMLEY, 2007c; PAN et al., 2005).

However, it is important to notice that such a strain rate controlled test is only performed on the starting microstructure of 3  $\mu\text{m}$  and 4.9  $\mu\text{m}$ . Thus, in the case of the initial grain size of 0.5  $\mu\text{m}$ , a constant cross head displacement is considered which induces a slight decrease of the target strain rate with the sample elongation.



Figure 3-7: MTS 50 kN machine with furnace equipped used at superplastic test.

### 3.2.3.2 Tensile tests in superplastic conditions (MTS 50 kN)

The Table 3-3 summarizes all the tensile test conditions (temperature and strain rate) used to characterize the samples with a starting grain size of 0.5  $\mu\text{m}$ , 3  $\mu\text{m}$  and 4.9  $\mu\text{m}$ .

Table 3-3: Experimental Matrix - superplastic (SP) test at temperature - 3 grain size.

Strain rate [ $\text{s}^{-1}$ ]	Temperature [ $^{\circ}\text{C}$ ]							
	700	770	800	840	850	870	920	950
$\dot{\epsilon} = 10^{-2} \text{ s}^{-1}$	*#	x	x*	x*#	x	x*	x	
$\dot{\epsilon} = 5 \cdot 10^{-3} \text{ s}^{-1}$	#							
$\dot{\epsilon} = 10^{-3} \text{ s}^{-1}$	*#	x	x*	x*#	x	x*	x	*
$\dot{\epsilon} = 5 \cdot 10^{-4} \text{ s}^{-1}$	#							
$\dot{\epsilon} = 10^{-4} \text{ s}^{-1}$	*#	x	x*	x*#	x*#	x*	x	*

(# 3.0  $\mu\text{m}$ ; \* 4.9  $\mu\text{m}$ ; x 0.5  $\mu\text{m}$ )

Regarding the definition of the tensile test conditions, the typical superplastic properties for Ti–6Al–4V alloy are tested at a temperature range and strain rate range of  $10^{-2}$  to  $10^{-4} \text{ s}^{-1}$ . Note that, as already mentioned, the fine grain starting microstructure of 3.0 and 4.9  $\mu\text{m}$  are frequently certified in the aircraft industry.

Hence, the test conditions to investigate the superplastic capabilities of the ultra-fine grain microstructure of 0.5  $\mu\text{m}$  are defined by decreasing the test temperature (forming temperature) and by increasing the strain rate. The test conditions considered for each starting micro-structure have been selected to be close or similar in order to compare their strain-stress responses.

### 3.3. STATIC TESTS AT HIGH TEMPERATURE CONDITION

The static tests consider different temperature exposure time of samples regarding to the mechanical testing times. The goal of these tests is to be able to investigate the grain growth behaviour of the alloys without any mechanical deformation. When compared to the grain growth after mechanical testing under the same temperature history, it will then be possible to define the grain growth only due to the strain rate.

The specimens were heat treated according to times used during the pre-heating in the dynamic tests, using a high-temperature furnace Nabertherm® (Figure 3-8). The temperature varied from 700 to 920 °C. Samples were exposed to several heating times and then quenched under air for cooling as shown in Figure 3-9.

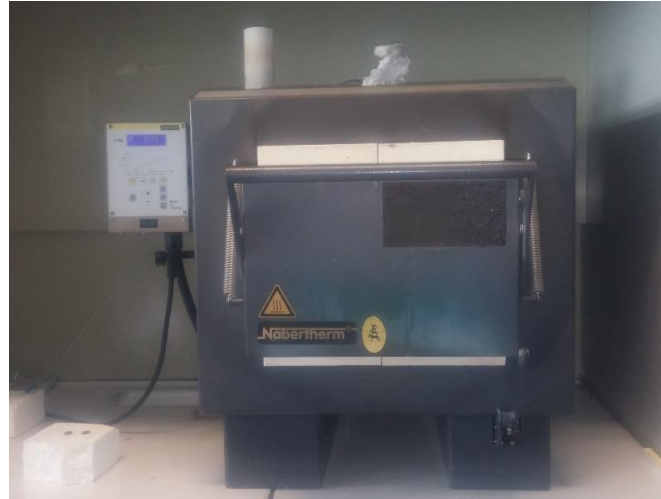


Figure 3-8 – Nabertherm® furnace using in annealing tests.

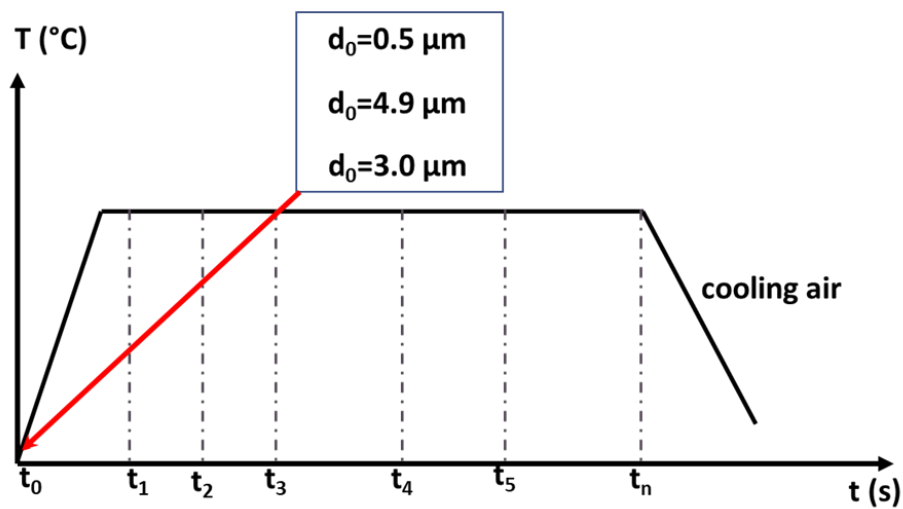


Figure 3-9 – Thermal cycle of the heat treatment named "static test"

### 3.4. MICROSTRUCTURAL INVESTIGATION

Microstructural investigations were carried out by light, scanning electron microscopy as well as by image analysis.

#### 3.4.1 Sample preparation

Metallographic samples were cut from the middle of the sheet using a circular saw model IsoMet 5000 Precision Saw in both cross and longitudinal sections. Afterwards, the metallographic specimens were embedded using Bakelite powders on a SimpliMet 3000 Automatic Mounting Press Buehler© machine (Figure 3-10).

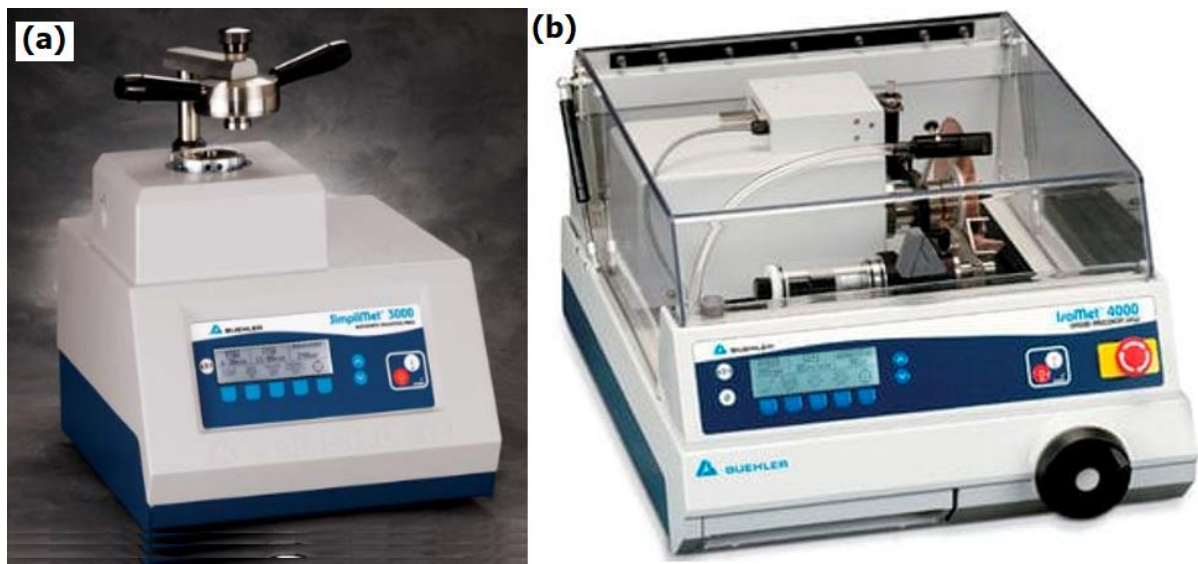


Figure 3-10 - SimpliMet 3000 Automatic Mounting Press Buehler© machine (a). circular saw model IsoMet 5000 Linear Precision Saw (b).

Surface investigated were ground on an EcoMet 300 machine tool using an abrasive SiC paper with a grit of P300 and 600 until plane. Subsequently the ground surfaces were polished using a 9  $\mu\text{m}$  diamond suspension and, finally polished with a mixture of colloidal silica and hydrogen peroxide. After that, a mirror like quality of the surface specimen was achieved.

Finally, an etch which consisting of 10 parts of hydrofluoric acid (HF), 30 parts nitric acid ( $\text{HNO}_3$ ) and 60 parts of peroxidic ( $\text{H}_2\text{O}_2$ ) was employed for etching of the metallographic specimens during a time of 15-20 seconds.

### 3.4.1. Sample observation and grain size measurement

Microstructural studies of the metallographic specimens were carried out on a Leica DMRM light microscope with a highest possible magnification of x1000 and on a SEM Novanano-SEM (FEI). The size of alpha grain was evaluated using Image-J software. Optical and SEM micrographs were obtained in the middle of the specimens in order to compare the deformation behaviour of the material at different strain rate and temperature.

The procedure for grain size measurement consists of drawing two diagonals on each grain in order to obtain the mean diameter's grain size. (see Figure 3-11). For this the grain size was measured using micrographs obtained from an SEM.

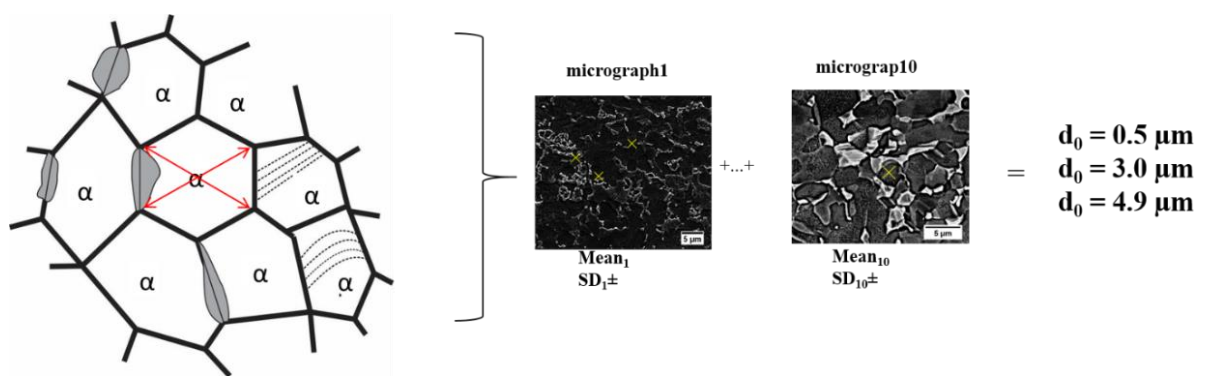


Figure 3-11 - Measurement grain size procedure

## 4. MECHANICAL TEST

In this chapter are presented and discussed the mechanical test results and their influence on the microstructural evolutions under high temperature and lower strain rate. For that, it is carried out measurements of the grain size and distribution for each test condition are carried out: dynamic tests and static tests.

From the typical Equations (4-1) and Equation (4-2) were build the true stress-true strain curves in dynamic condition (COMLEY, 2007):

$$\varepsilon_v = \ln(1 + \varepsilon_c) = \ln\left(1 + \frac{u}{l_0}\right) \quad (4-1)$$

$$\sigma = \sigma_c(1 + \varepsilon_c) = \frac{F}{S_0} \left(1 + \frac{u}{L_0}\right) \quad (4-2)$$

### 4.1. DYNAMIC TESTS RESULTS

The mechanical behaviour results for experimental tests will be present and discussed from this section as the Gleeble as well the MTS 50 kN. The metallographic examination is presented at the last part in this section.

#### 4.1.1. Gleeble 3800 test results

All results presented in this part were obtained on samples that were machined from sheet 1 supplied by EMBRAER to USP (4.9  $\mu\text{m}$  grain size).

#### 4.1.2. Mechanical results.

##### a) Effect of temperature at constant strain rate

- **Strain rate  $10^{-3} \text{ s}^{-1}$**

The Figure 4-1a shows some of the specimens issued from Gleeble 3800 tests where we can notice four different state: first on the top of Figure 4-1a we can see a non-deformed specimen and followed by specimens deformed at strain rate of  $10^{-3} \text{ s}^{-1}$  at 950 °C, 700 °C and 600 °C.

The Figure 4-1b shows the true-stress-true strain curves obtained from lower strain rate ( $10^{-3} \text{ s}^{-1}$ ) at increasing temperatures (600, 700, 850 and 950 °C). The curves obtained at lower strain rate are noisier when compared to higher strain rate. This effect can be related to the low level of loads required during deformation process at lower strain rate.

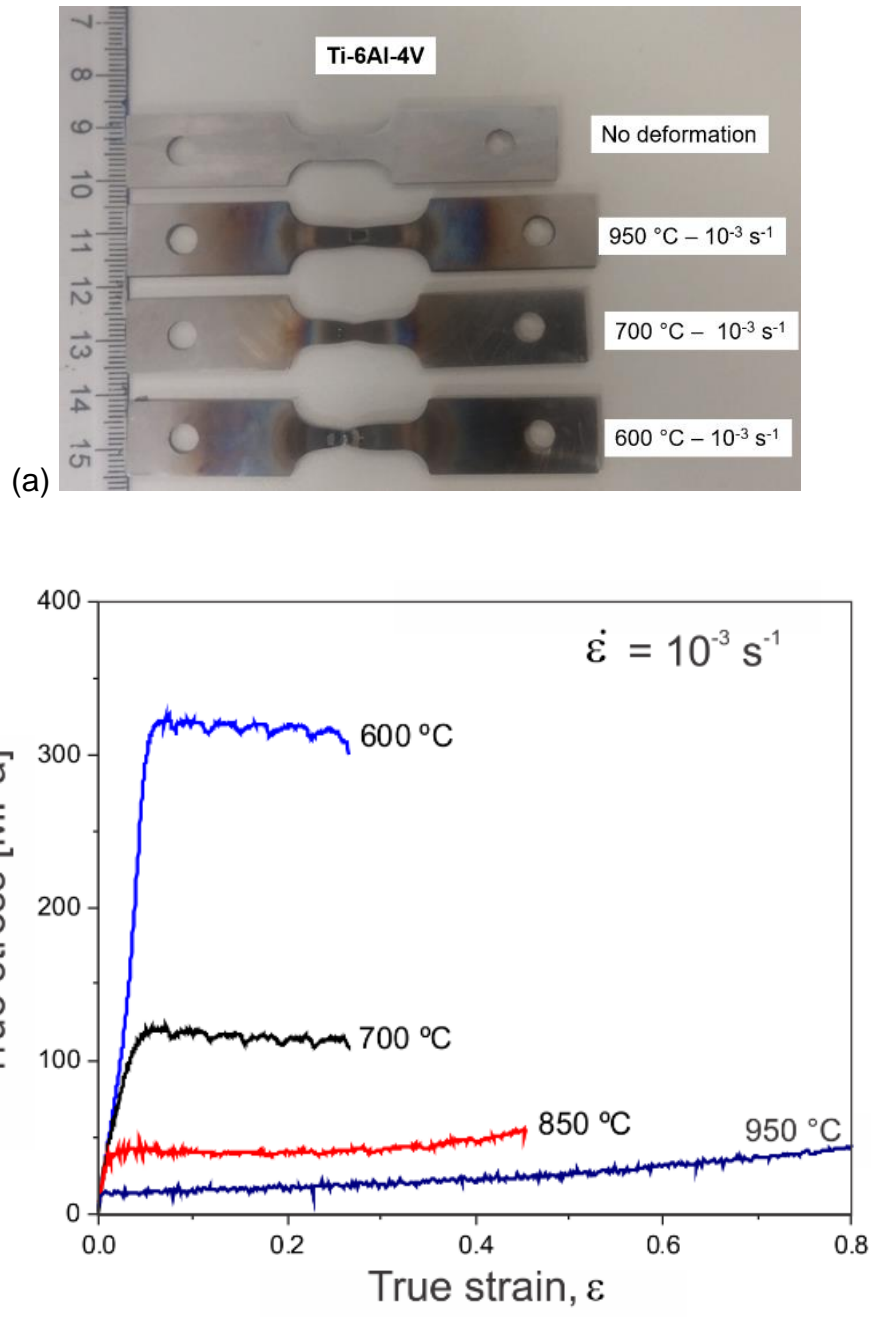


Figure 4-1 - The curves obtained at high strain rate are more noisy, due to the high forces involved compared to the testing machine cell capacity.

- Strain rate  $10^{-1} \text{ s}^{-1}$

The Figure 4-2 presents load vs displacement curves: it can be noticed the hardening rate due to the higher strain rate. For temperature at  $950 \text{ }^{\circ}\text{C}$  a flat curve is observed in comparison with those obtained at  $600$ ,  $700$  and  $850 \text{ }^{\circ}\text{C}$ .

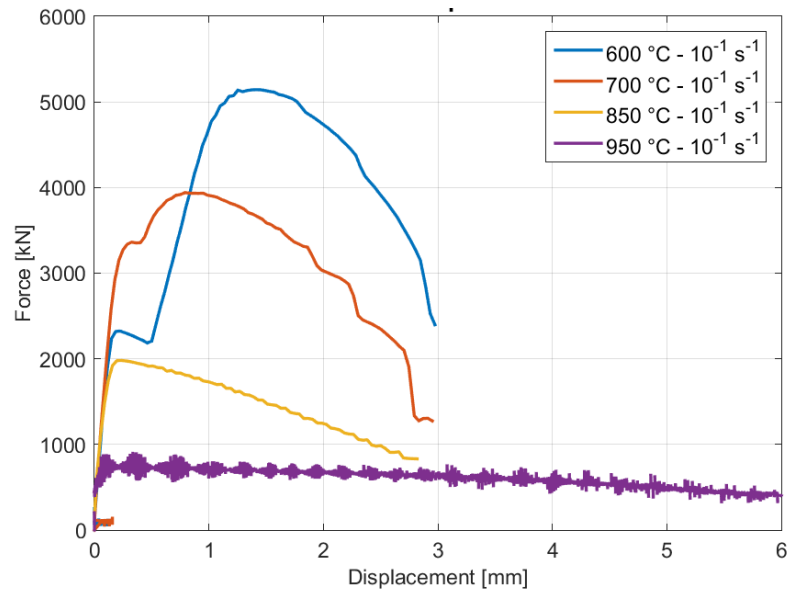


Figure 4-2 - Variation of elongation with initial strain rate at different temperatures for  $10^{-1} \text{ s}^{-1}$  strain rate.

Figure 4-3a - shows a test specimen after having been submitted at  $950 \text{ }^{\circ}\text{C}$  and strain rate  $10^{-1} \text{ s}^{-1}$ : a good ductility without failure is observed. It can also be noticed a colour in the heat-affected zone by joule effect. That colour suggests a modification of microstructure by recrystallisation. Figure 4-3b presents the true stress-true strain curve obtained at  $950 \text{ }^{\circ}\text{C}$  and strain rate  $10^{-1} \text{ s}^{-1}$ ; true strain at rupture is higher than 0.2.

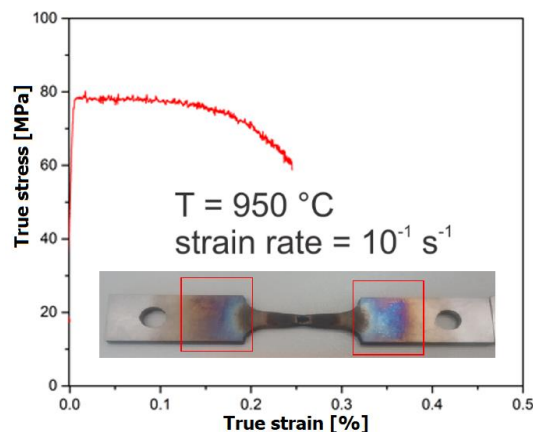


Figure 4-3 – The specimen for thermomechanical test and (a) the true stress-strain curves obtained via the uniaxial tensile tests (b)

**a) Effect of strain rate at constant temperature**

- **Temperature 850 °C**

Figure 4-4 presents true-stress true-strain curves at 850°C for 3 strain rates. As expected the higher strain rate presents a hardening rate very important when compared to lower strain rate i.e.:  $10^{-3} \text{ s}^{-1}$  where the mechanical behaviour curve is flatter shaped.

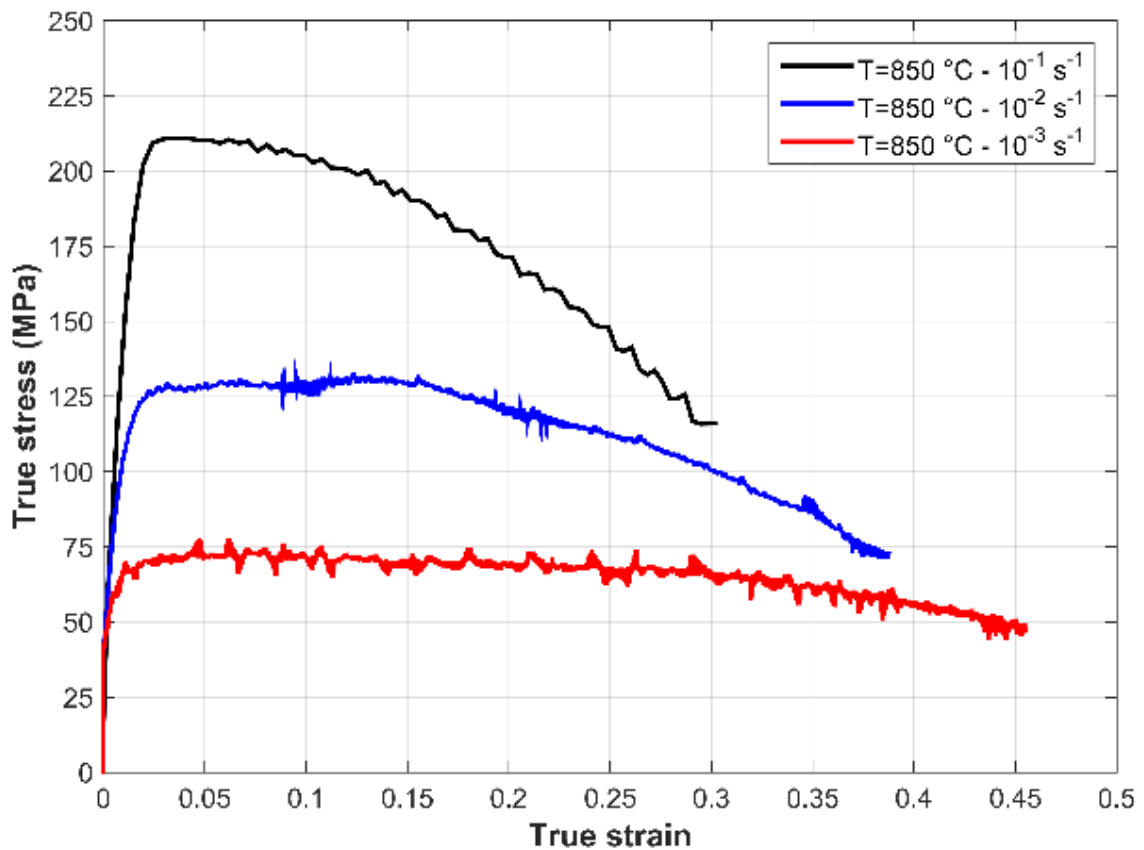


Figure 4-4 – Tensile test stress-strain curves at 850 °C and a strain rate from  $10^{-3} \text{ s}^{-1}$  to  $10^{-1} \text{ s}^{-1}$ .

- **Temperature 950 °C**

Figure 4-5 show the true stress-true strain curves at 950 °C for strain rate from  $10^{-3} \text{ s}^{-1}$  to  $10^{-1} \text{ s}^{-1}$ . Here the hardening rate reduction is smaller when comparing to 850 °C. Moreover, curves obtained for the two lower strain rates ( $10^{-3} \text{ s}^{-1}$  and  $10^{-2} \text{ s}^{-1}$ ) are quite similar.

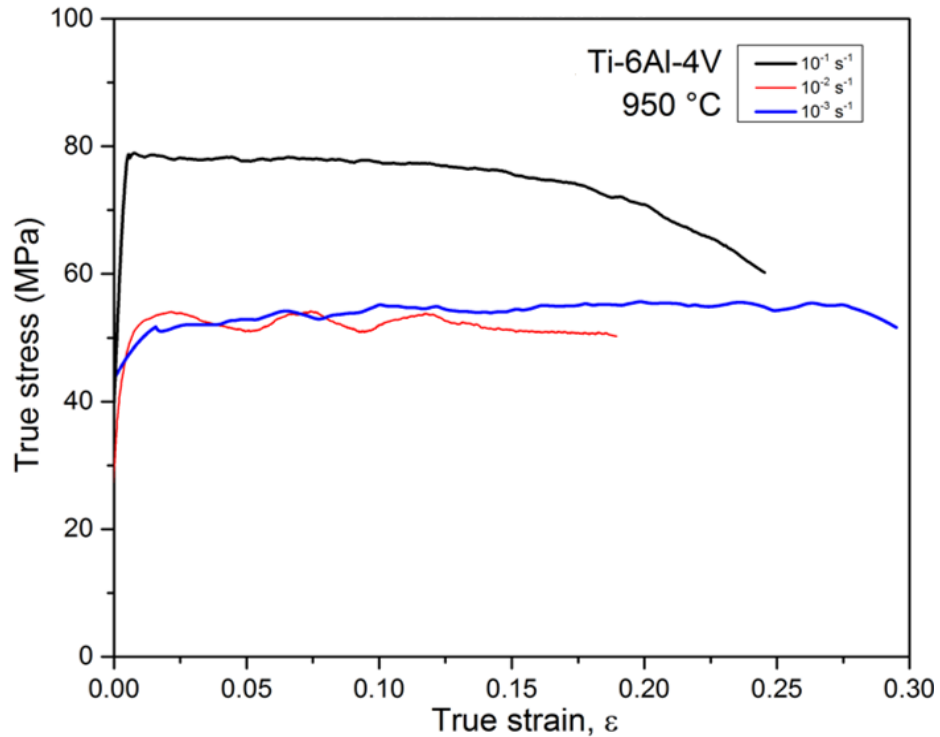
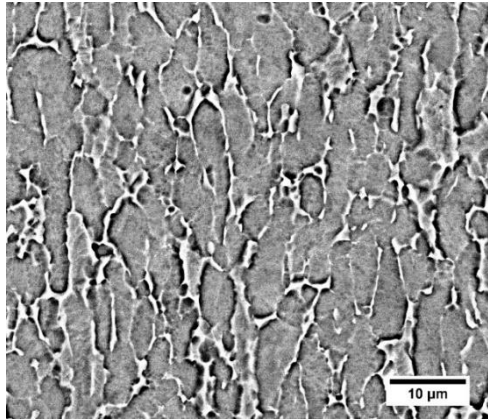


Figure 4-5 – Tensile test stress-strain curves at 950 °C and strain rate from  $10^{-3} \text{ s}^{-1}$  to  $10^{-1} \text{ s}^{-1}$ .

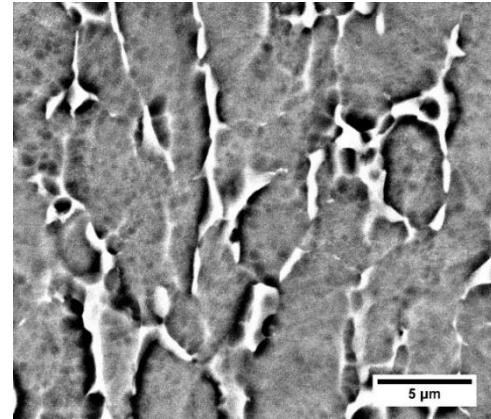
#### 4.1.3. Microstructural Analysis after mechanical testing

The Figure 4-6 presents the microstructure after deformation in Gleeble thermomechanical tests machine. These observations have been performed in the center of the test samples. It can be seen the grain elongations that could be attributed to a hot working plasticity mechanism. The microstructure can be seen at two magnifications (2000x and 5000x) at 700 °C and 850 °C for strain rate from  $10^{-3}$  to  $10^{-1} \text{ s}^{-1}$ .

@ 700 °C -  $\dot{\epsilon}=10^{-3} \text{ s}^{-1}$

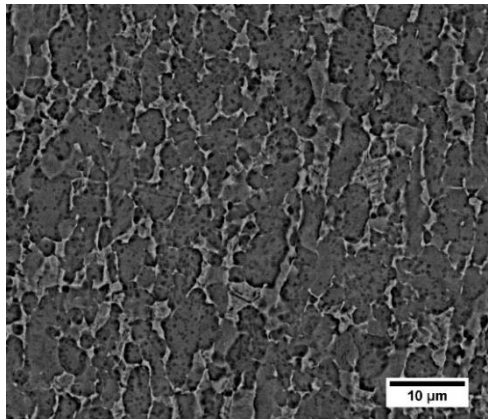


700 °C;  $\dot{\epsilon}=10^{-3} \text{ s}^{-1}$ ; mag. 2000x

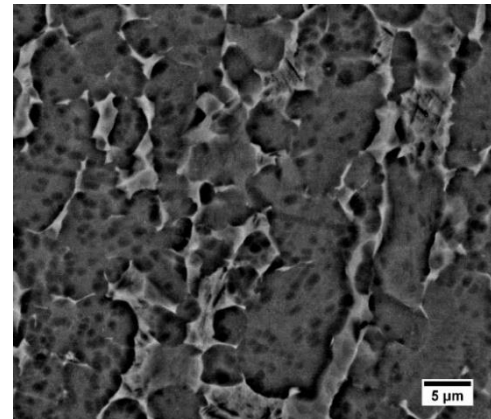


700 °C; 5000x

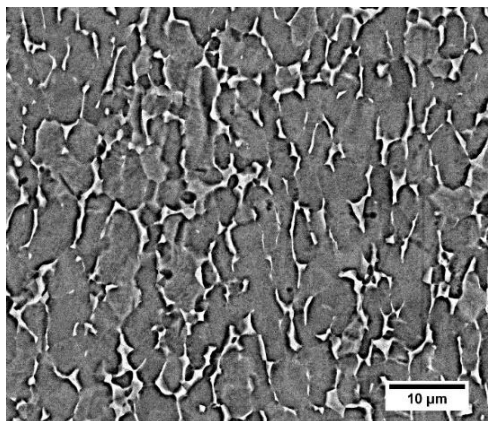
@ 850 °C -  $\dot{\epsilon}=10^{-3} \text{ s}^{-1}$



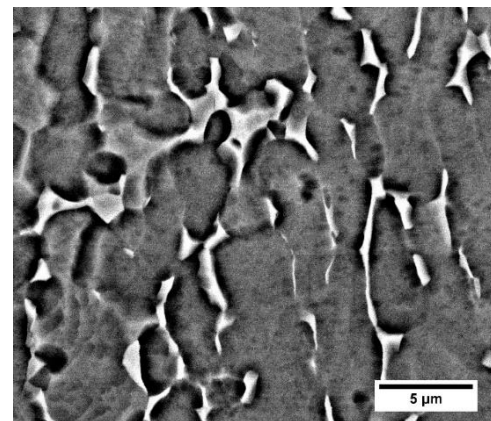
850 °C -  $\dot{\epsilon}=10^{-1} \text{ s}^{-1}$ ; (a) 2000x



850 °C (b) 5000x



850 °C;  $\dot{\epsilon}=10^{-2} \text{ s}^{-1}$  © 2000x



850 °C;  $\dot{\epsilon}=10^{-2} \text{ s}^{-1}$  © (d) 5000x

Figure 4-6 – Microstructure after Gleeble thermomechanical deformation process at 700 °C and 850 °C for a strain rate from  $10^{-3} \text{ s}^{-1}$  to  $10^{-1} \text{ s}^{-1}$ . Two magnifications: 2000x and 5000x.

The Figure 4-7 illustrates the microstructure's specimen sheet 1 with a selected area indicating the arrangement of the grains of the  $\alpha$ -phase and the  $\beta$ -phase for the specimen tested at 950 °C – strain rate are  $10^{-3} \text{ s}^{-1}$ . It helps to identify round shapes of the grains, in this case a higher temperature and a lower strain rate could have contributed to superplastic grains boundary sliding mechanism in predominance in this set up condition. We can observe the lamellae formation in the SEM micrograph in yellow arrow detail (see detail in Figure 4-7) that occur during the slow cooling from 950 °C.

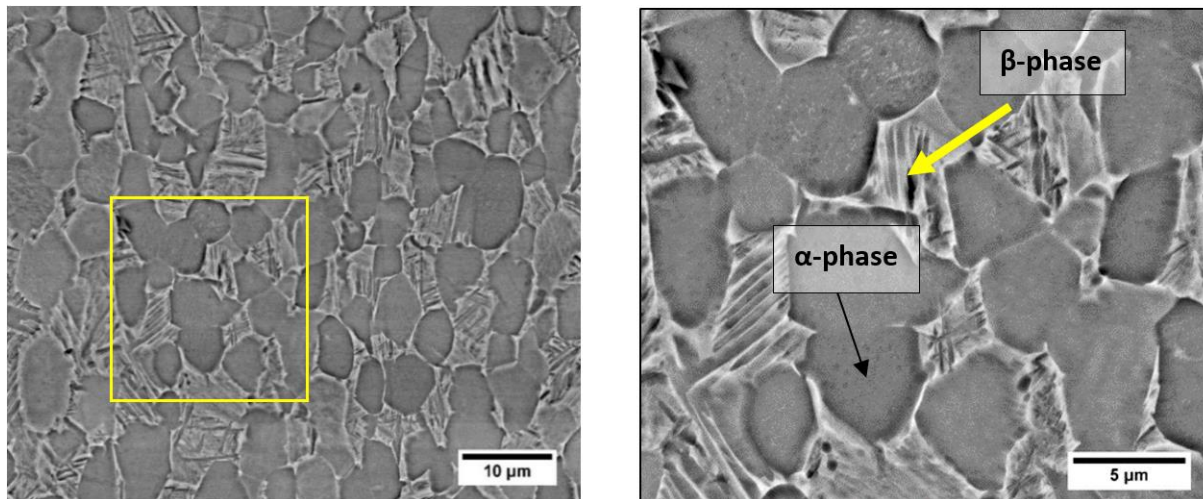


Figure 4-7 – Microstructure with selected area of  $\alpha$ -phase and  $\beta$ -phase sample tested at 950 °C – strain rate:  $10^{-3} \text{ s}^{-1}$ .

#### 4.1.4. Test results on samples tested on MTS 50kN equipment

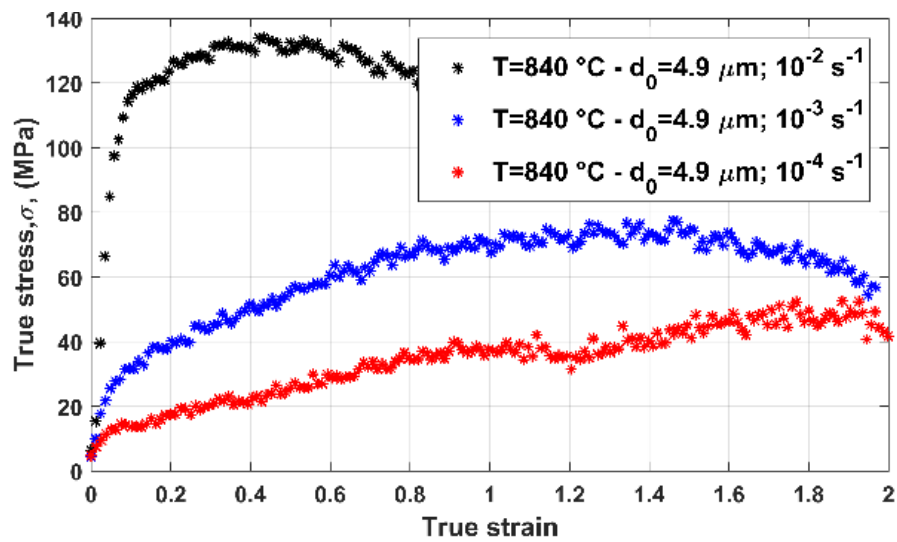
Results presented in this part were obtained on samples that were machined from the three different sheets investigated in this work (grain sizes of 0.5, 3 and 4.9  $\mu\text{m}$ ).

#### 4.1.5. Mechanical behaviour

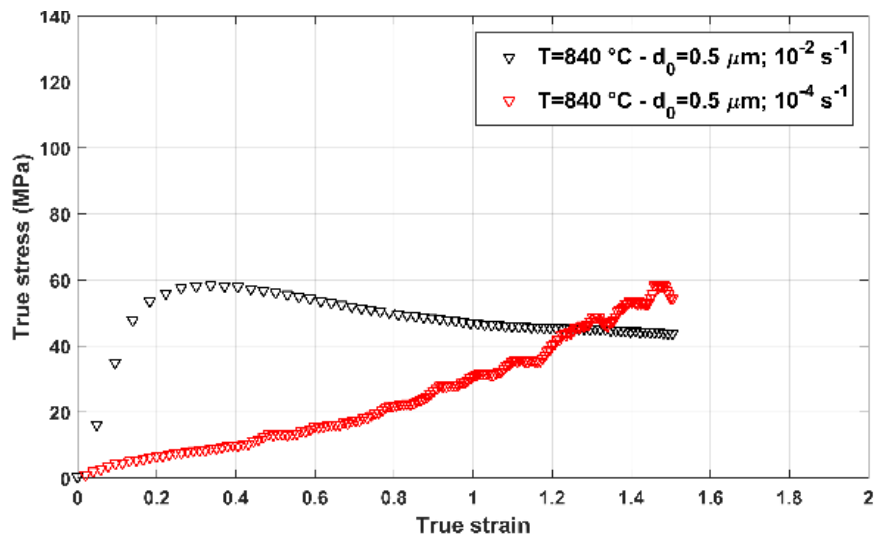
The tensile true stress-true strain curves of the mechanical behaviour are summarized under various strain rates and temperatures. Figures of deformed samples are reported in Appendix B.

### a) Influence of strain rate at Temperature 840 °C

The Figure 4-8 shows the influence of strain rates at lower temperature 840 °C on the mechanical behaviour for two grain sizes (4.9 and 0.5  $\mu\text{m}$ ). The smaller strain rate facilitates the superplastic mechanism of grain boundary sliding for the average grain size material of 4.9  $\mu\text{m}$ . The Figure 4-8b presents the results for the average grain size of 0.5  $\mu\text{m}$  and there is a very important difference between mechanical behaviour influenced by its initial grain size (ALABORT; PUTMAN; REED, 2015): flow stresses are much lower and strain hardening much more important at the lowest strain rate ( $10^{-4} \text{ s}^{-1}$ ).



(a)



(b)

Figure 4-8- True strain-stress curves for the same temperature level and two different grain sizes: 4.9 (a) and 0.5 (b)  $\mu\text{m}$ .

### b) Influence of strain rate at Temperature 750 °C

The true stress–strain curves observed during the tensile tests at 750 °C and strain rates from  $10^{-2}$  to  $10^{-4}$  s $^{-1}$  for the initial microstructure 0.5 and 3.0  $\mu$ m respectively (see Figure 4-9) has a relatively stable flow with low stress values, which is typical for superplastic deformation. However, the maximum elongation was observed at higher strain rate of  $10^{-4}$  s $^{-1}$  when some strain hardening occurred. The increase in the strain rate to  $10^{-2}$  s $^{-1}$  leads to an extensive hardening during deformation and lower tensile elongations. The extensive hardening was also observed on the initial microstructure 3.0  $\mu$ m but it decreases with decreasing strain rate from  $10^{-3}$  to  $10^{-4}$  s $^{-1}$ .

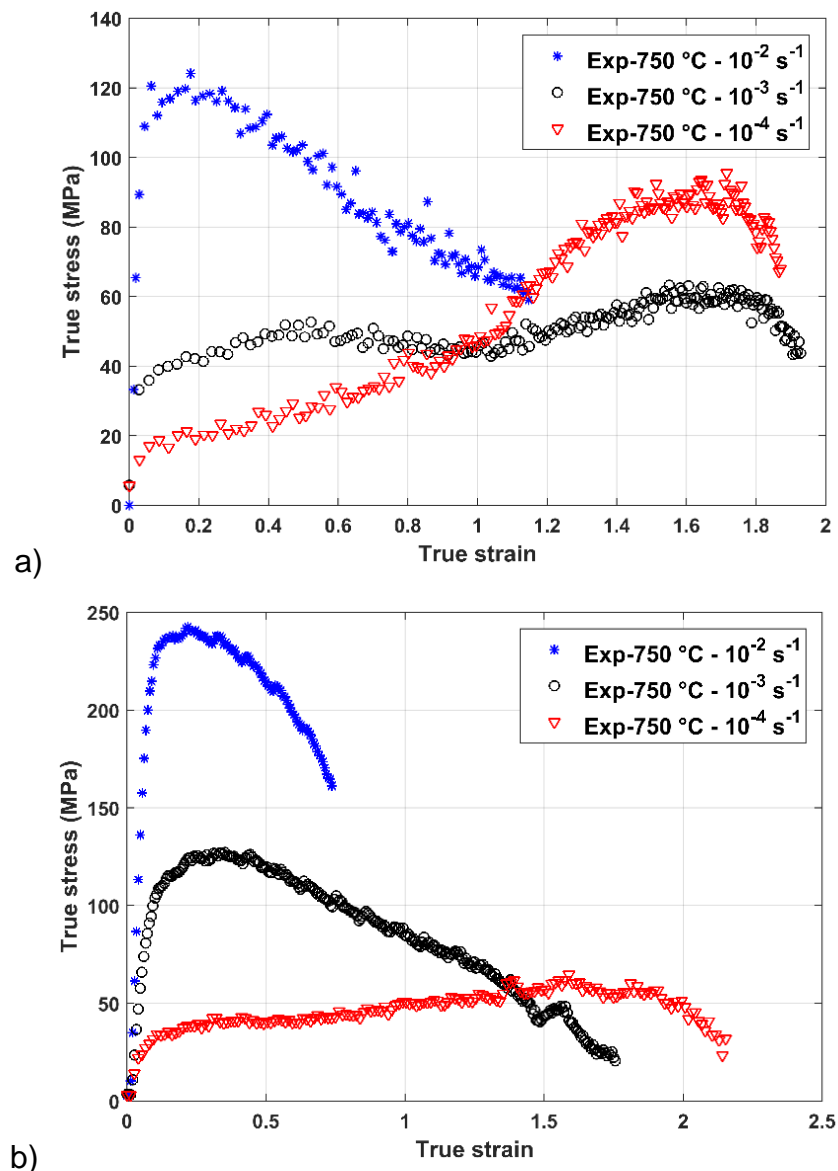


Figure 4-9– Mechanical behaviour at 750: initial microstructure 0.5  $\mu$ m a) and initial microstructure 3.0  $\mu$ m b)

**c) Behaviour at Strain rate  $10^{-2} \text{ s}^{-1}$  for various temperatures (initial microstructure  $3.0 \mu\text{m}$ )**

A view of several specimens for strain rate  $10^{-2} \text{ s}^{-1}$  after deformation is shown on Figure 4-10. It is seen that specimens deformed at higher temperature have a shape for superplastic deformation (range of temperature from  $800 \text{ }^\circ\text{C}$  to  $870^\circ$  for a strain rate of  $10^{-2} \text{ s}^{-1}$ ). For lower temperature range (from  $650 \text{ }^\circ\text{C}$  to  $770 \text{ }^\circ\text{C}$ ) it can be seen that an extensive strain hardening occurs that leadsto a typical hot working material shape curve.

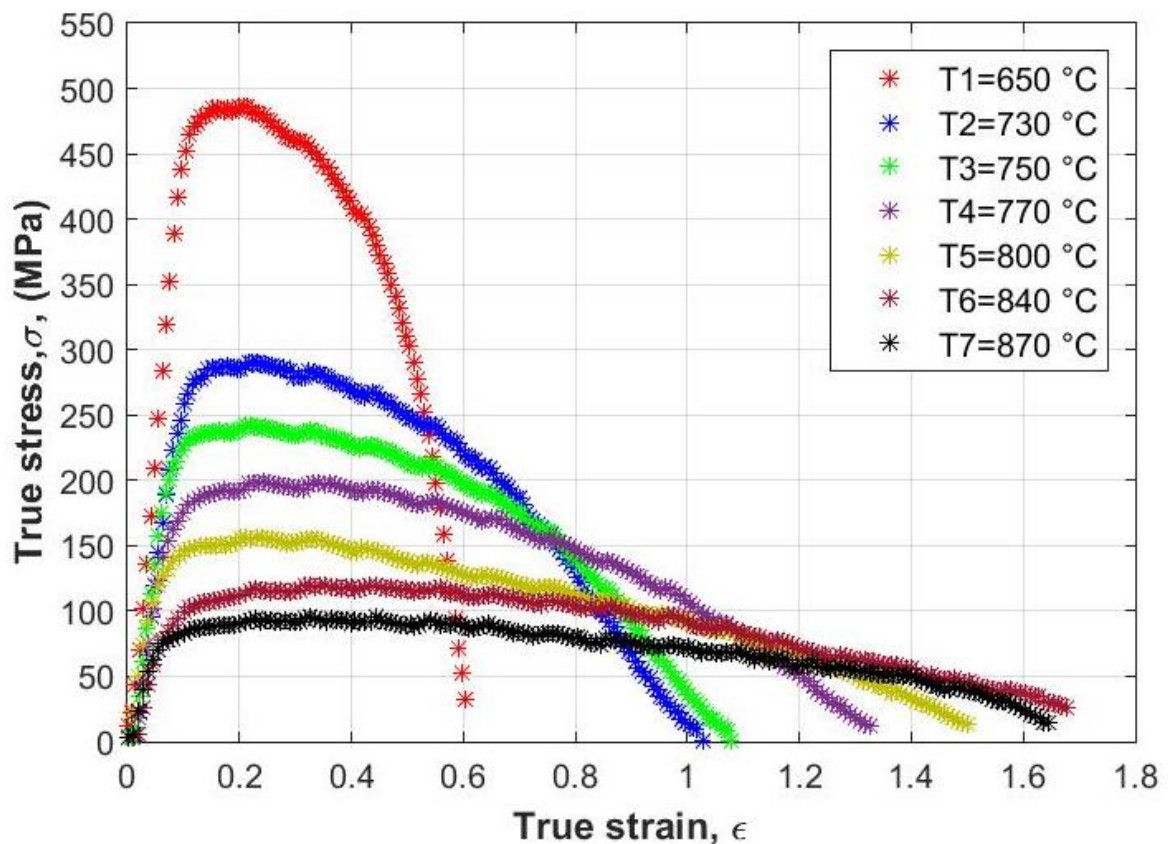


Figure 4-10 – Mechanical behaviour for initial microstructure  $3.0 \mu\text{m}$  and strain rate  $10^{-2} \text{ s}^{-1}$

Another mechanical test result are visible in Appendix B.

**4.1.6. Microstructure analysis after mechanical testing**

Figure 4-11 shows, for the  $4.9 \mu\text{m}$  initial grain size, a summary of the microstructures observed after high temperature mechanical testing for all the samples investigated ( $800^\circ\text{C}$  to  $950^\circ\text{C}$  and strain rate from  $10^{-2} \text{ s}^{-1}$  to  $10^{-4} \text{ s}^{-1}$ ). It can be noticed a dynamic grain growth at higher temperature which present a typical superplastic microstructure. In lower temperature, i.e.: at  $800 \text{ }^\circ\text{C}$  and higher strain rate  $10^{-2} \text{ s}^{-1}$  the

microstructure is slightly similar to initial ones, while the microstructure at lower strain rate i.e.:  $10^{-3} \text{ s}^{-1}$  to  $10^{-4} \text{ s}^{-1}$  present a large grain growth in order of 2.5x. There is an evident difference between grain size at  $800 \text{ }^\circ\text{C}$  for a strain rate  $10^{-4} \text{ s}^{-1}$  and  $950 \text{ }^\circ\text{C}$  for the same strain rate level ( $\dot{\epsilon} = 10^{-4} \text{ s}^{-1}$ ).

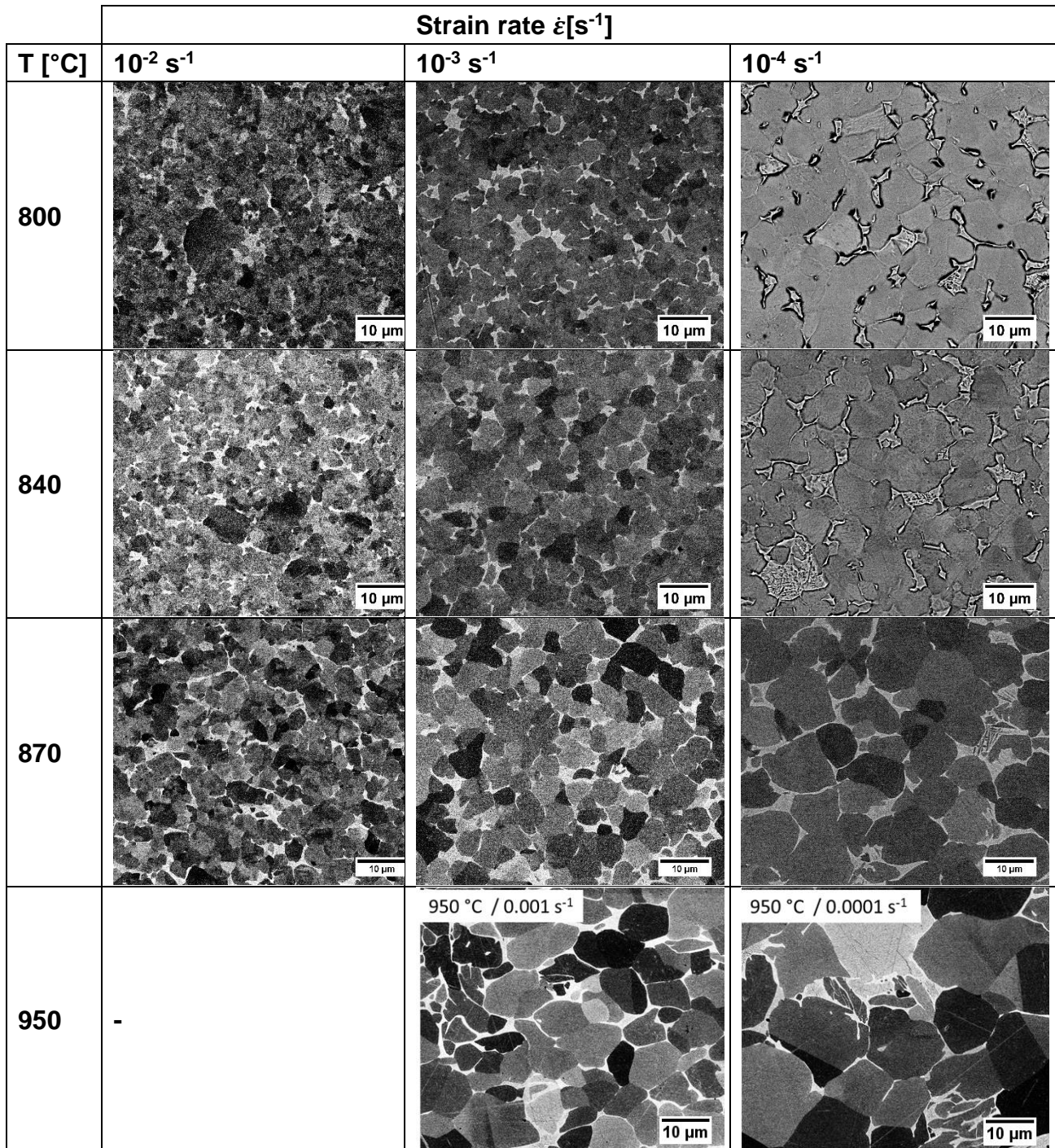


Figure 4-11- The micrographics show dynamic grain growth evolution for tensile tests at temperature range from  $800 \text{ }^\circ\text{C}$  to  $950 \text{ }^\circ\text{C}$  and strain rate from  $10^{-2} \text{ s}^{-1}$  to  $10^{-4} \text{ s}^{-1}$  for an initial grain size of  $4.9 \text{ } \mu\text{m}$ .

In Table 4-1 the values of dynamic grain growth measures measured for the tensile test samples as shown in Figure 4-11. We are observed a significant increase of grain size for slow strain rate combined within high temperature. These effects of grain growth are related to absorption energy by microstructure during heating.

Table 4-1 - Dynamic Grain growth size ( $d_{\text{dyn}}$ ) measurements ( $\mu\text{m}$ ) (MTS).

Temperature [°C]	Strain rate [ $\dot{\epsilon}$ ]					
	$\dot{\epsilon} = 10^{-2} \text{ s}^{-1}$		$\dot{\epsilon} = 10^{-3} \text{ s}^{-1}$		$\dot{\epsilon} = 10^{-4} \text{ s}^{-1}$	
	average	SD±	average	SD±	average	SD±
700	4.97	0.81	5.47	1.2	5.76	0.85
800	5.34	0.9	5.54	1.03	6.46	1.02
840	5.43	0.79	5.82	0.95	7.46	0.99
850	5.49	0.88	5.93	0.91	7.52	1.40
870	5.67	0.85	6.9	1.01	10.57	2.21
950	-	-	10.6	1.9	15.6	3.60

## 4.2. STATIC GRAIN GROWTH

### d) Grain size 4.9 $\mu\text{m}$

The grain growth is investigated by conducting static tests (see Figure 4-12). The static tests consider different temperature exposure time regarding to the forming time during the process.

The Figure 4-12 illustrates the grain growth evolution for the static tests in the temperature range from 800°C to 950 °C and exposure times  $t = 120\text{s}$ ;  $t = 2,100\text{s}$  and  $t = 23,4000\text{s}$ .

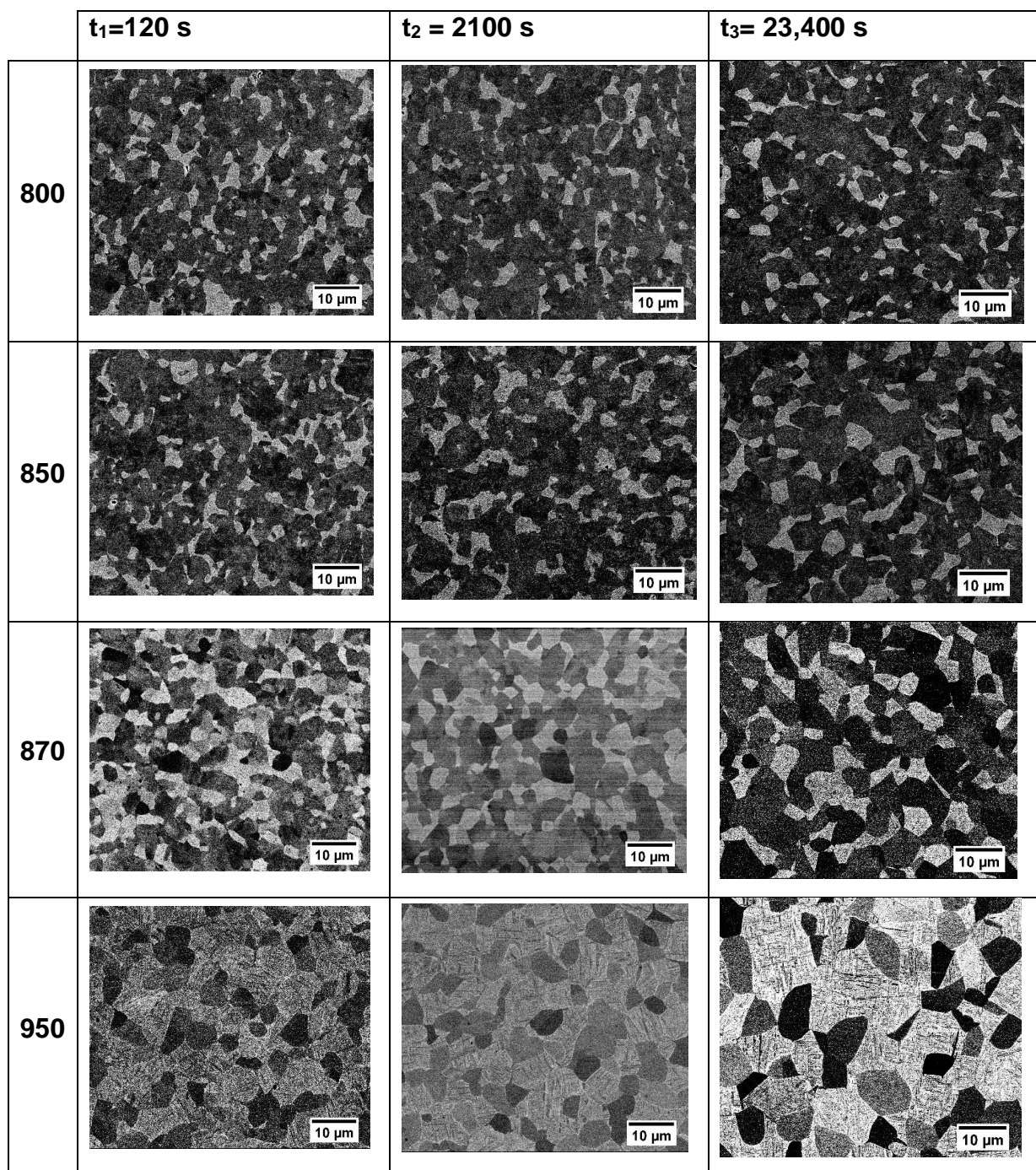


Figure 4-12- FEGSEM BSE mode micrographs of samples heat treated at 800°C(a,c,e) and 850°C (b,d,f) and 870 °C water quenched (a,b), 950 °C cooled in air (c,d) and cooled in furnace (e,f).

In this case, the measured grain size allows to analyze the static grain growth for all temperature tested as well as to identify that an increase of temperature induces an important microstructure evolution as seen in the Figure 4-13. We can notice the grain growth change for each temperature level considering three different heat time (120 seconds, 2100 seconds and 24300 seconds). Temperature play a role in the microstructure change promoting a grain growth in the material.

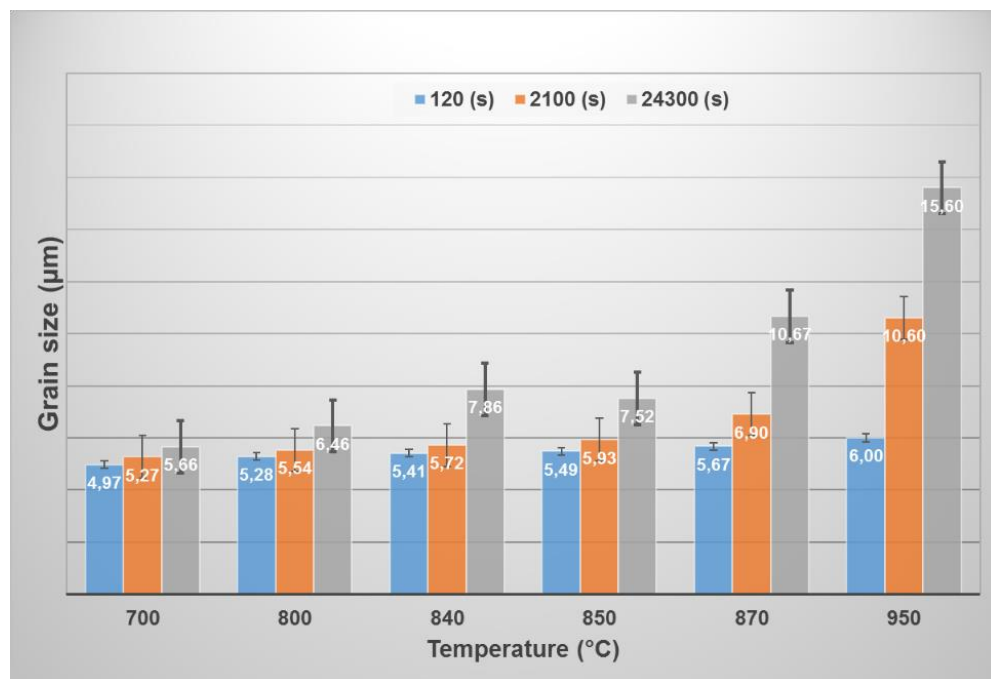


Figure 4-13 - Measurements of the static grain growth for different heat-treating times.

- **Grain size 3.0  $\mu\text{m}$**

The measurement grain growth evolution allows to analyze the static grain growth for all temperature tested as well as to identify that increase of temperature allowed an important microstructural evolution as seen in the Figure 4-14 that illustrates the grain growth evolution for the static tests at  $T = 840\text{ }^{\circ}\text{C}$  and several temperature exposure times ( $t = 1000\text{ s}$  (a),  $t = 5000\text{ s}$  ; (b),  $t = 10000\text{ s}$  (c) and  $t = 30000\text{ s}$  (d)) (VELAY et al., 2016).

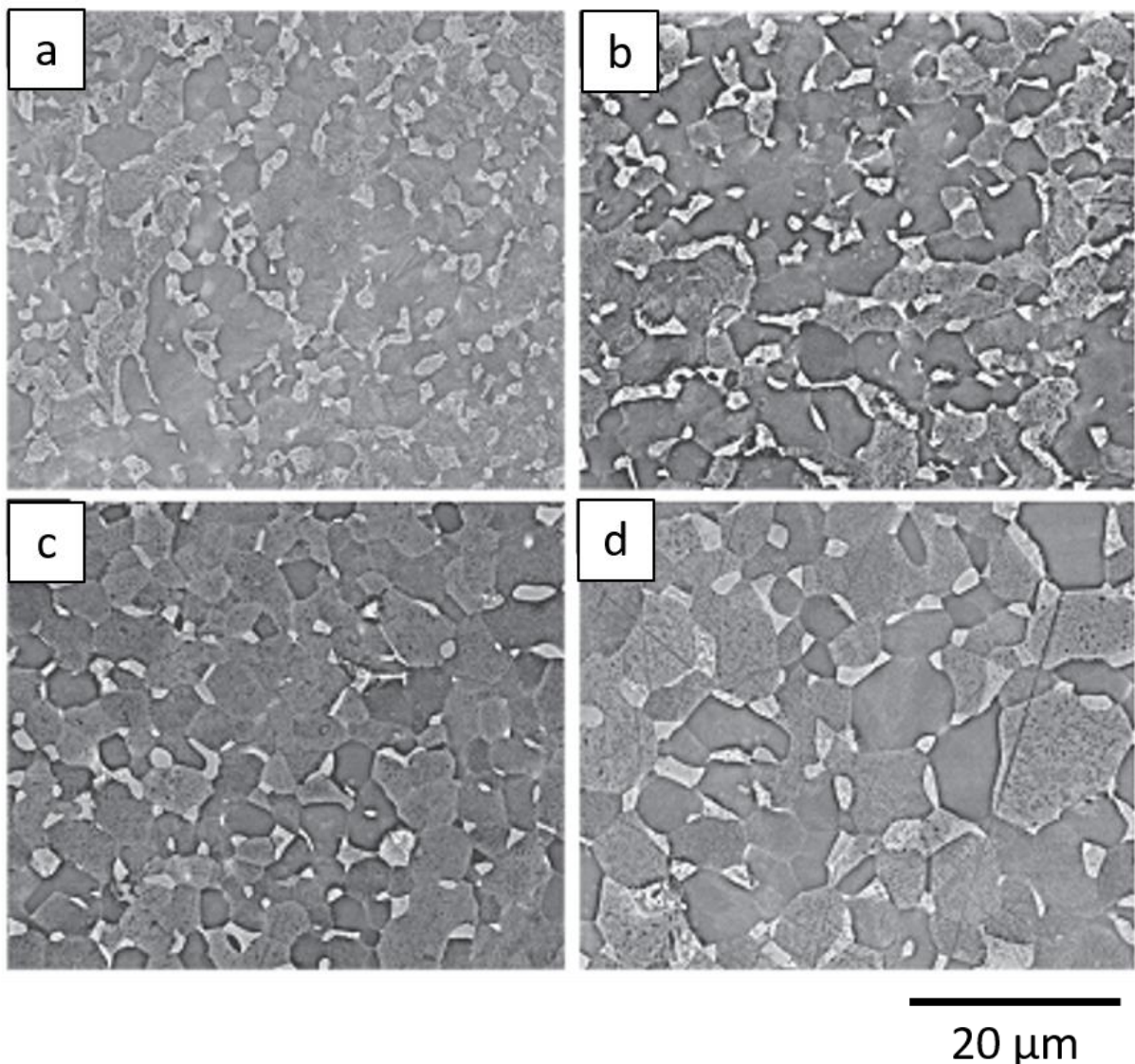


Figure 4-14 – Grain growth evolution observed by SEM micrographs (BSE mode) in the case of the static tests at  $T = 840\text{ }^{\circ}\text{C}$  and several temperature exposure times  $t = 1000\text{ s}$  (a),  $t = 5000\text{ s}$  (b),  $t = 10000\text{ s}$  (c) and  $t = 30000\text{ s}$  (d) (VELAY et al., 2016).

## 5. BEHAVIOUR MODELLING

The present chapter presents and discusses the constitutive models based on microstructural evolution. They use experimental data provided by tensile tests carried out in the present work. Hence, a behaviour model is presented able to describe both mechanical and microstructural responses of the material.

### 5.1. LITERATURE REVIEW

The main point of microstructural mechanisms and deformation conditions that control superplastic forming, among different test conditions, are related to tensile/creep test results and micro structural analysis. The parameters that are prerequisite for materials to exhibit superplasticity are reviewed. This basically includes strain rate sensitivity index ( $m$ ) and temperature effect (COMLEY, 2007a; PAN et al., 2005; VELAY et al., 2016).

The model formulations can also introduce parameters related to the micro structural changes which can greatly influence the mechanical behaviour (DANG; CHANDRA, 1998; LIN; CHEN, 2011). As illustrated the Figure 5-1, an approach to micromechanical model for a dual-phase (A+B) superplastic material.

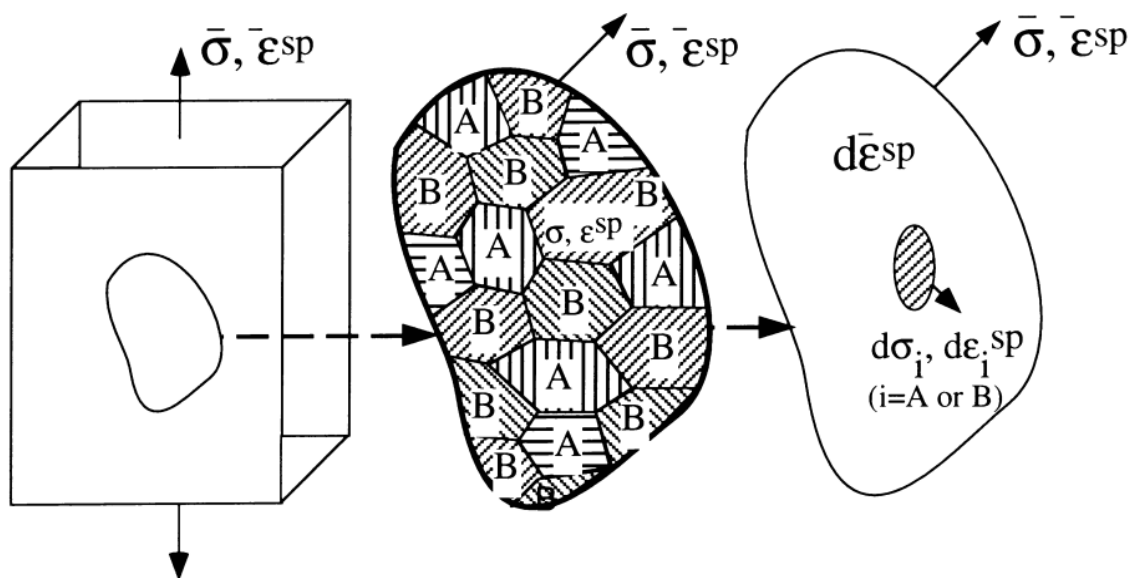


Figure 5-1 - Dual-phase polycrystalline model based on the self-consistent relation (DANG; CHANDRA, 1998)

These micro structural evolutions such as grain size, shape, stability are in relation to the induced mechanisms such as grain movements accommodated by dislocation motion, diffusion or boundary sliding (GAO et al., 2017).

Depending on the activated mechanisms, behaviour model can require complex constitutive equations able to predict mechanical response of the material and the microstructural evolution themselves activated by the deformation and the temperature (BRUSCHI et al., 2014).

Lin & Dean (2005), discuss models physically based on microstructural evolution during hot forming and its effects on viscoplastic flow. Such approaches can be applied to optimize processing conditions and at the same time to improve final product properties. These variables are incorporated into appropriate viscoplastic constitutive equations and their interaction with the microstructural parameters material are characterized, a set of unified physically based viscoplastic constitutive equations can be formed.

Cheong, Lin, and Ball (2001), show the importance of the grain growth and grain size control that dynamically affects viscoplastic flow and superplastic forming processes. For this purpose, they present physically based viscoplastic constitutive equations for superplastic alloys considering both static and dynamic grain growth at high temperature. In this context, the static evolution can be described in the behaviour model by a new internal variable related to the grain size who's the evolution equation will only include a time dependent term (5-1)

$$\dot{d} = \frac{M\sigma_{surf}}{d} \quad (5-1)$$

Moreover, if a dynamic evolution occurs for a given inelastic strain rate, the previous law can be modified by considering time and strain rate dependent terms in to the evolution equation. (5-2)

$$\dot{d} = \alpha d^{-\gamma_0} + \beta \left| \dot{\epsilon}_p \right| d^{-\phi} \quad (5-2)$$

As show in the sequel, the grain size internal variable will have a significant effect on the mechanical behaviour.

According to (DOMKIN, 2005), the parameters identification of an empirical model without any microstructural consideration, can be done generally by mean fitting model equations with experimental data. In this sense, GAO et al. (2017), led a research about superplastic forming processes modelling from rheological approaches applied on Ti-6Al-4V titanium alloy. They concluded that the established constitutive model can accurately predict the superplastic deformation behaviour.

The approach developed in the present study is based constitutive model and fitting parameters from experimental data. Moreover, it includes microestrutural considerations related to the grain size evolution. The constitutive equations are first presented and afterwards the results obtained on Ti-6Al-4V alloy are discussed.

## 5.2. GRAIN GROWTH MODELLING

Semiatin & Sargent (2010) employed a grain growth model which takes account static and dynamic grain growth for a temperature range from 775 °C to 815 °C. In the present work, the model is used and extended to take account the grain growth from 700 °C to 950 °C.

According to Deshmukh (2003), the static ( $d_{static}$ ) and dynamic ( $d_{dynamic}$ ) grain growth mechanisms are assumed to be independent and the total grain growth rate ( $\dot{d}_0$ ) is given by Equation (5-3).

$$\dot{d}_0 = \dot{d}_{static} + \dot{d}_{dynamic} \quad (5-3)$$

### 5.2.1. Static condition

The static grain growth is given by Equation (5-4), it describes the atomic diffusion process affected by temperature and related to the grain boundary mobility and boundary energy density (CHEONG; LIN; BALL, 2003; LIN, 2003; VELAY et al., 2016):

$$\dot{d}_{static} = A_1 d^{-m_1} \quad (5-4)$$

where  $A_1$  is a temperature dependent parameter. In the sequel,  $m_1=2$ .

The Figure 5-2 presents the extrapolated values curves provided by the work of Semiatin et al. (2010) (775 °C to 815 °C) and illustrates the evolution over temperature of the coarsening rate coefficients under static conditions where the established law was extrapolated to the temperatures used in this work (from 700 °C to 950 °C) . These coefficients give an empirical law of the static grain growth Equation (5-5) for a given initial grain size. This law will be used to identify the parameter of Equation (5-4) for several temperature levels.

$$d^3(t) - d_0^3 = K_d(T).t \quad (5-5)$$

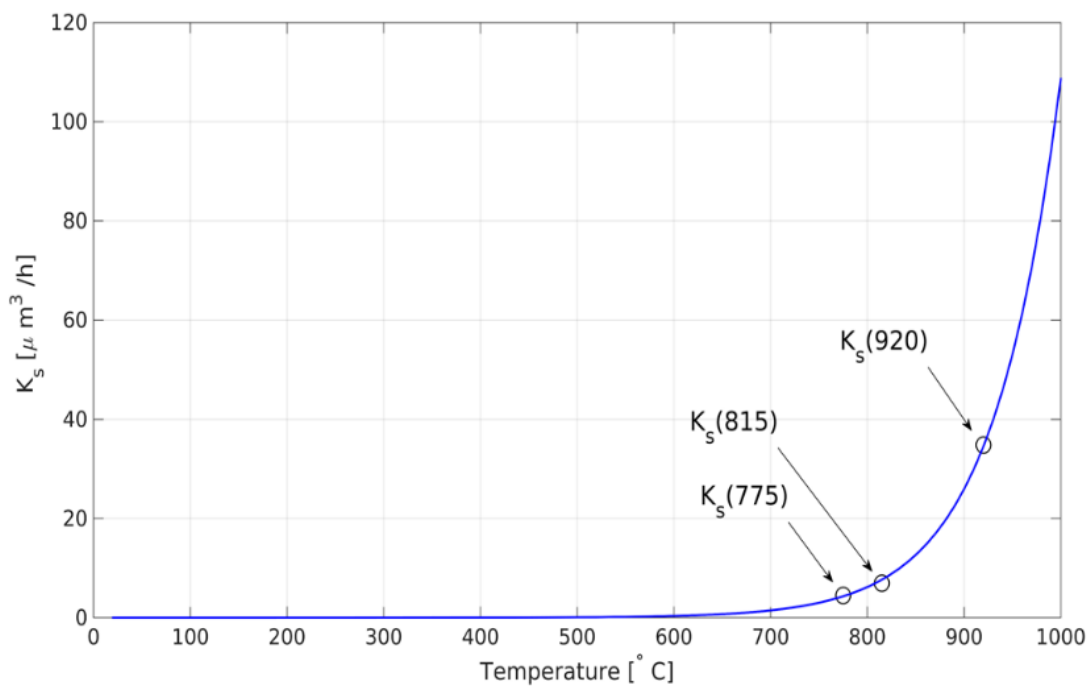


Figure 5-2 - Identification of the coarsening rate constants based on the values provided by Semiatin et al. at 775 °C and 815 °C and extrapolation from 700 °C to 920 °C (adapted from Semiatin & Sargent (2010))

### 5.2.2. Dynamic Condition

The dynamic grain growth Equation (5-6) allows to reproduce grain growth kinetics over a range of temperatures and strain rates (CAO; LIN, 2008).

$$\dot{d}_{dynamic} = A_2 \dot{p}^{n_1} d^{m_2} \quad (5-6)$$

where  $A_i$ ,  $m_i$  ( $i = 1; 2$ ) and  $n_1$  are temperature dependent parameters and  $p$  is the effective inelastic strain. In the sequel,  $m_1 = m_2 = 2$

Similarly to the static conditions, the work of Semiatin et al. (2010) allows us to determine the coarsening rate coefficients under dynamic conditions, for a wide temperature range and several strain rates. These empirical laws follow the same evolution law than in the static case (Equation (5-6)); They were used to identify the parameters of Equation (5-5). The Figure 5-3 and Figure 5-4 shows the identification of the coarsening rate constants based on the dynamic values provided by Equations (5-6) (SEMIATIN et al., 2010) at 775 °C and 815 °C and  $\epsilon=10^{-4} \text{ s}^{-1}$ ;  $10^{-3} \text{ s}^{-1}$  and extrapolation at 920 °C.

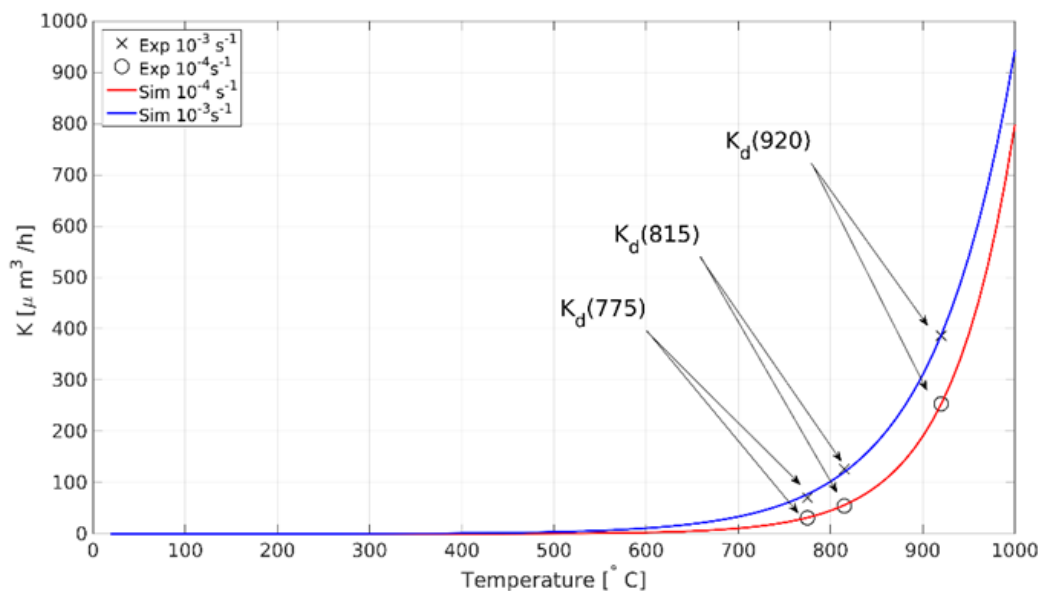


Figure 5-3 - Identification of the coarsening rate constants based on the values provided by (SEMIATIN et al., 2010) at 775 °C and 815 °C and  $\epsilon=10^{-4} \text{ s}^{-1}$ ;  $10^{-3} \text{ s}^{-1}$  and extrapolation from 700 °C to 920 °C

In both conditions (static and dynamic), the empirical Semiatiin's laws match very well with the grain size measurements performed in this work by using SEM observations and image analysis whatever the test conditions (strain rates, temperatures, initial grain size ...). In the next part, these laws are used as experimental data and allow to identify the coefficients of the differential equations given by Equations (5-4) and (5-6).

### 5.2.1. Results and discussions

Figure 5-4 shows the comparison of the computed grain growth obtained under both static and dynamic conditions and for several temperatures with the grain size measurements provided by microstructural observations and image analysis.

The results obtained are in a very good agreement with experiment data. Hence, the differential equations allow to simulate the static and dynamic grain growth for various starting microstructures, several temperature levels and strain rates.

The Table 5-1 presents the parameters of the grain growth evolution with the temperature. One can notice an increase parameter  $A_1$  and  $A_2$  with the temperature and for  $n_1$  parameter, a slow increase with increasing temperature

Table 5-1 - Parameters of the grain growth evolution with the temperature

Parameters of the grain growth evolution	Temperature [°C]						
	650	700	730	750	770	800	870
$A_1 \times 10^{-13} \text{ (mm}^3 \text{ s}^{-1}\text{)}$	1.24	2.01	2.71	3.31	4.05	5.46	10.75
$A_2 \times 10^{-11} \text{ (mm}^3 \text{ s}^{-1+n_1}\text{)}$	1.38	3.08	4.95	6.72	9.19	14.7	45.0
$n_1$	0.331	0.356	0.37	0.379	0.388	0.402	0.480

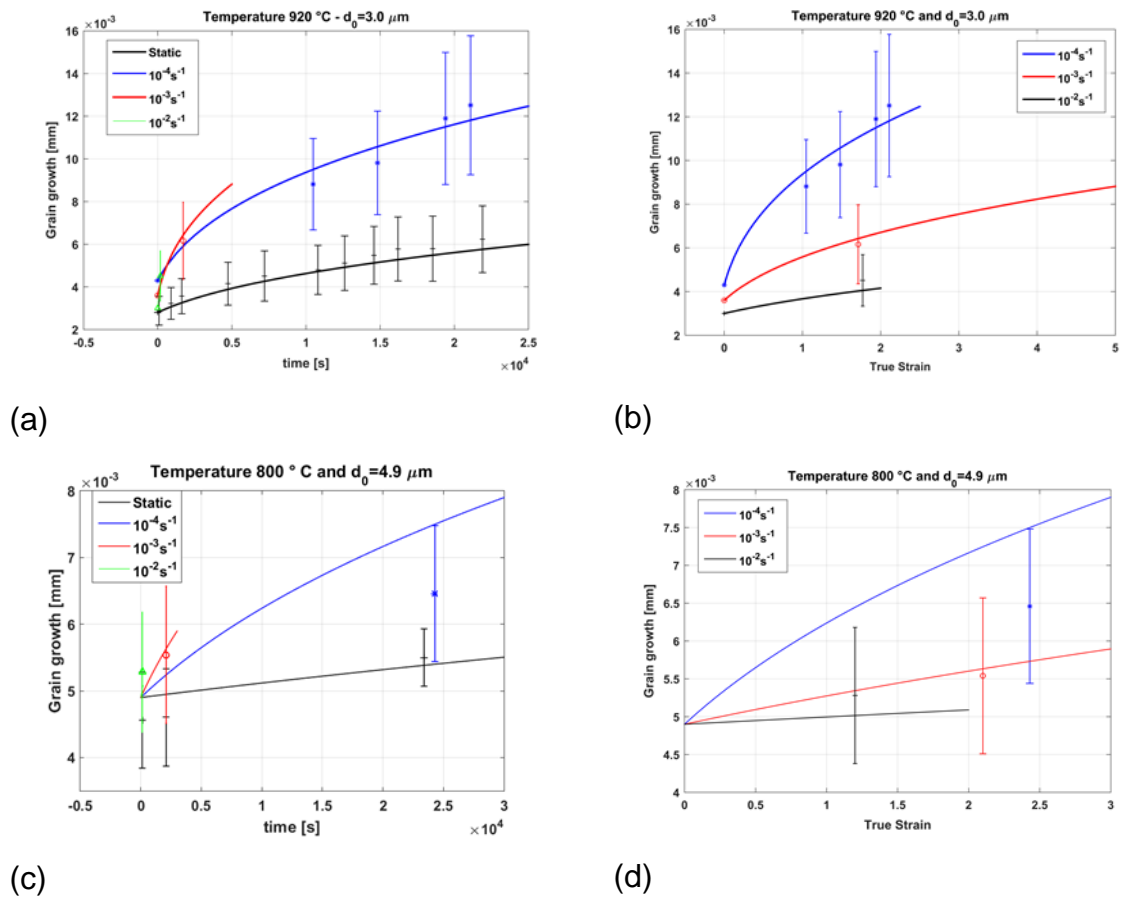


Figure 5-4 - Comparison of computed grain growth-time (a,c) and computed grain growth-strain (b,d) curves using the evolution law identified with the coarsening rate constants by Semiatin et al and experimental measurements performed in the present work at 920 °C and  $d_0=3\mu\text{m}$  (a,b); at 800 °C and  $d_0=4.9\mu\text{m}$  (c,d).

### 5.3. MECHANICAL BEHAVIOUR MODELLING

This part presents the model formulation developed in this study to describe the true stress true strain curves obtained for several test conditions (Temperature and strain rates) and various starting microstructures. First, the constitutive equations are described in details and the introduction into the model formulation of the internal variable associated to the grain size evolution is explained. Then, some predictions are shown.

### 5.3.1. Constitutive equations

Such approaches are in agreement with the thermodynamics of the irreversible processes and can be developed either under small or large deformation conditions. Moreover, they allow to predict complex thermomechanical loadings encountered in the hot forming processes (VANDERHASTEN; RABET; VERLINDEN, 2008; VELAY et al., 2016)

The elasticity domain is classically described by a von Mises yield criterion. It considers an elasticity limit  $\sigma_0$  and an isotropic hardening variable  $R$  related to the dislocation motion and density in the inelastic deformation (Equation (5-7)). This variable is not significant under superplastic deformation mechanisms but can become predominant for the low temperatures or for an important grain growth. Their formulations are presented in the Equations (5-7) and (5-8):

$$f = \sigma_{eq} - R - \sigma_0 \quad (5-7)$$

$$R = Q(1 - e^{-bp}) \quad (5-8)$$

Where  $p$  is the effective strain,  $Q$  and  $b$  are material parameters.

Assuming normality and associated flow rule, the multiaxial viscoplastic strain rates for materials implemented within a large deformation is presented in the Equation (5-9)

$$D_p = \frac{\partial \Omega}{\partial \sigma} = \Omega'(f) \frac{\partial f}{\partial \sigma} \quad (5-9)$$

Where  $\dot{p} = \Omega'(f) = \left[ \frac{f}{K} \right]^n = \sqrt{\frac{3}{2} D_p : D_p}$ . Moreover, the corotational stress rate is given by Hooke's law by Equation (5-10)

$$\sigma = 2GD_e + \lambda Tr(D_e) \quad (5-10)$$

In which  $G = \frac{E}{2(1+\nu)}$  is the shear modulus defined by the Young Modulus  $E$  and the Poisson ratio  $\nu$ , and the lame elasticity constant is given by  $\lambda = \frac{E\nu}{(1-2\nu)(1+\nu)}$

$D_e$  is the elastic strain rate which can be expressed from the total and inelastic strain rates by considering a strain rate partition:  $D_e = D_t - D_p$  with  $D_t$  is the rate of the total deformation.

The deformation gradient  $F$  can be defined together with the velocity gradient  $L$  and can be decomposed as the rate of the deformation tensor  $D$  and the spin tensor  $W$ ; as pointed in the Equation (5-11)

$$L = \dot{F}F^{-1} = D + W \quad (5-11)$$

$$\text{With } D = \frac{1}{2}(L + L^T) \text{ and } W = \frac{1}{2}(L - L^T)$$

Thus, the material stress rate can be expressed from the corotational stress rate, the spin tensor and the Cauchy stress as shown in the Equation(5-12).

$$\dot{\sigma} = \overset{\nabla}{\sigma} + W\sigma - \sigma bW \quad (5-12)$$

### 5.3.2. Introduction of grain growth effect on the viscosity and the hardening law

According to Velay et al., (2016) that model formulation aims to consider the initial grain size and its evolution with the temperature and the deformation. The initial grain size effect is introduced into the model formulation through the viscous parameters  $K$  and  $n$  (see Equation (5-13)).

$$K = K_r \left( \frac{d}{\chi(d_0)} \right)^{\frac{\mu}{n}} \Rightarrow n = n_r \left( \frac{d}{\chi(d_0)} \right)^{\alpha}; \quad (5-13)$$

Where  $d$  is the average grain size (5-13)  $\mu$  and  $\alpha$  are material constants which characterize the continuous material hardening due to grain growth. The initial grain size is taken into account by the parameter  $X$  written as a function of the initial grain size,  $d_0$ ,  $\chi(d_0) = \chi_1 e^{-\chi_0 d_0}$ ,  $\chi_0$  and  $\chi_1$  are constant parameters as described by Velay et al. (2016)

The evolution law translates that the more important the initial grain size will be the more promptly its effect on the viscous flow will vanish. These equations can reproduce the continuous increase of the viscous flow due to grain growth, but cannot describe the drastic increase of the stress level which operates at low strain rate and a long-time period. In such a case, the grain growth induces a change in the deformation mechanisms (dislocation glide) (CHEONG; LIN; BALL, 2003).

Then, the asymptotic value of the hardening variable  $Q$  is dependent on the grain growth variable  $d$  following the Equation (5-14) (VELAY et al., 2016).

$$Q = Q_0 e^{\gamma \Delta d} \quad (5-14)$$

where  $\Delta d = d - d_0$ ,  $Q_0$  and  $\gamma$  are constant parameters. Thus, the hardening will be important for significant increase of the grain size and reduced for a slight growth.

### 5.3.3. Results and discussions

This section presents and discusses the results obtained by comparison between experimental data and model predictions at a temperature from 700 °C to 950 °C and strain rate from  $10^{-2} \text{ s}^{-1}$  to  $10^{-4} \text{ s}^{-1}$ .

The Table 5-2 presents the temperature evolution of the identified parameters at (650 °C to 870 °C) for the mechanical behaviour model.

The values of the parameters found at Table 5-2 are identified from the tensile tests performed at the nominal temperatures (700, 770, 800, 840, 870 °C).

Table 5-2 – Temperature evolution of the identified parameters for the mechanical behaviour model (VELAY et al., 2016)

Identified parameters for the mechanical behaviour model	Temperature [°C]						
	650	700	730	750	770	800	870
$\sigma_0$ [MPa]	10	8.0	6.0	5.0	4.0	3.0	0.2
$K_r$ [MPa s <sup>1/n<sub>r</sub></sup> ]	1608	1750	1757	1700	1457	1250	1000
$n_r$ [-]	3.71	2.80	2.40	2.31	2.25	2.10	1.90
$\alpha$ [-]	0.128	0.095	0.088	0.08	0.764	0.0691	0.06
$Q_0$ [MPa]	5.0	6.9	8.4	9.5	10.6	12.5	17.2
$\gamma$ [mm <sup>-1</sup> ]	850	700	595	530	460	356	140

For temperature at 700 °C and for different initial grain sizes (4.9 µm and 0.5 µm) we can notice that starting microstructure greatly influences the flow stress and elongation levels Figure 5-5.

Indeed, the fine grain microstructure exhibits a decrease of the flow stress with an increase of the elongation in comparison to the average grain size of 4.9 µm. Moreover, one can observe a significant strain hardening occurring for the lower strain rates Figure 5-5.

The results in the Figure 5-5a does not present a deformation mechanism change for an initial grain size of  $d_0= 4.9 \mu\text{m}$ , whereas in Figure 5-5b this effect is observed and well assessed at low strain rate ( $10^{-4} \text{ s}^{-1}$ ) for an initial grain size of  $d_0= 0.5\mu\text{m}$ .

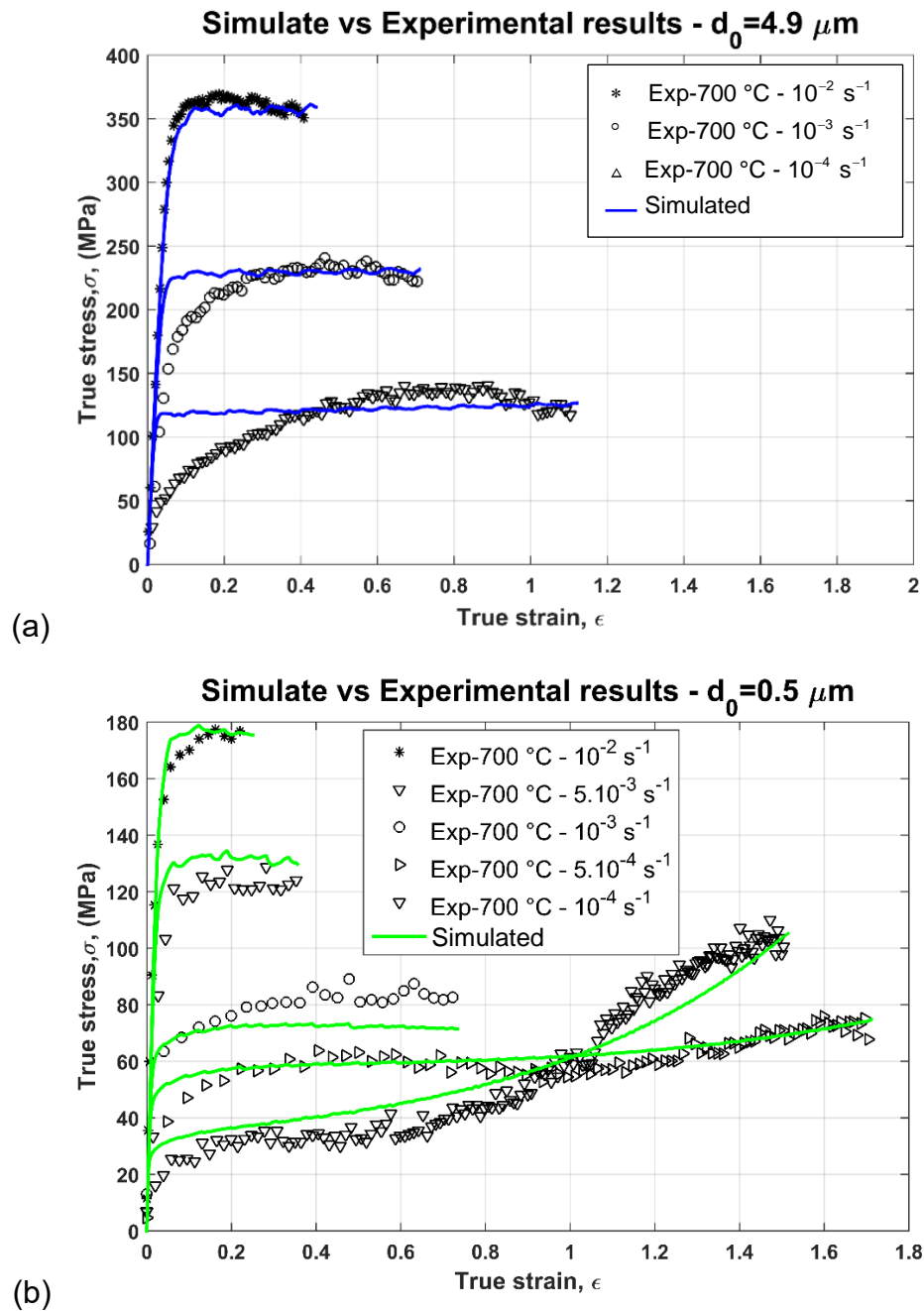


Figure 5-5 - Computed true strain - true stress data vs Experimental results at a temperature of 700 °C and initial grain size of  $d_0=0.5 \mu\text{m}$  (a) and  $4.9 \mu\text{m}$  (b)

For the case of the starting grain size of  $0.5 \mu\text{m}$  at a temperature of 840 °C and strain rate of  $10^{-2} \text{ s}^{-1}$  and  $10^{-4} \text{ s}^{-1}$ , one can notice that the behaviour model predicts a stress decrease (see Figure 5-6) It is due to the time-strain applied in the simulation inducing a slight strain rate decrease with the sample elongation.

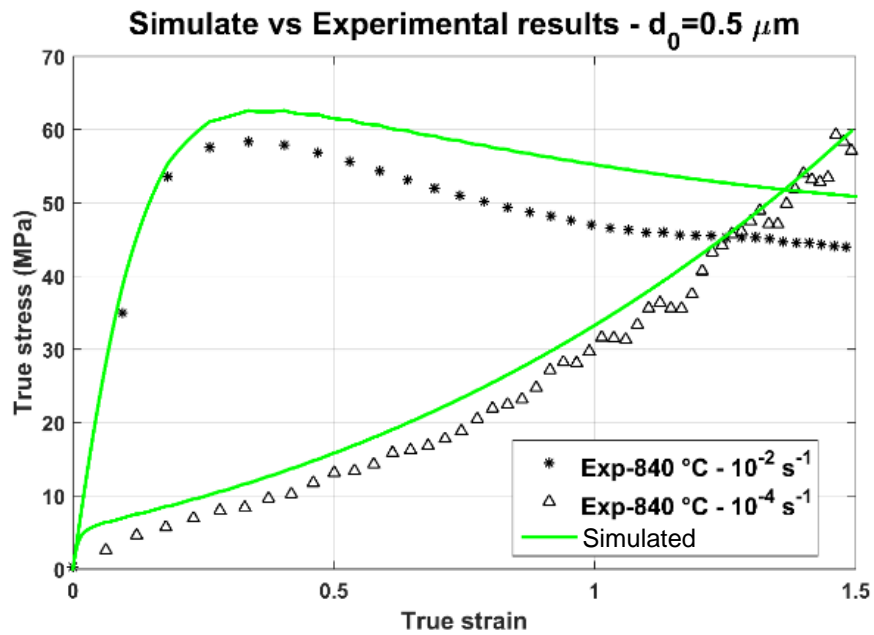


Figure 5-6 - Computed Strain-Stress data vs Experimental: results at a temperature of 840 °C and initial grain size of  $d_0=0.5 \mu\text{m}$

The Figure 5-7 presents the true stress-true strain predicted by the behaviour model at temperature of 840 °C and strain rate from  $10^{-2} \text{ s}^{-1}$  to  $10^{-4} \text{ s}^{-1}$  and a starting grain size of  $d_0= 3.0 \mu\text{m}$ . The results show a good fitting between experimental data and the model response.

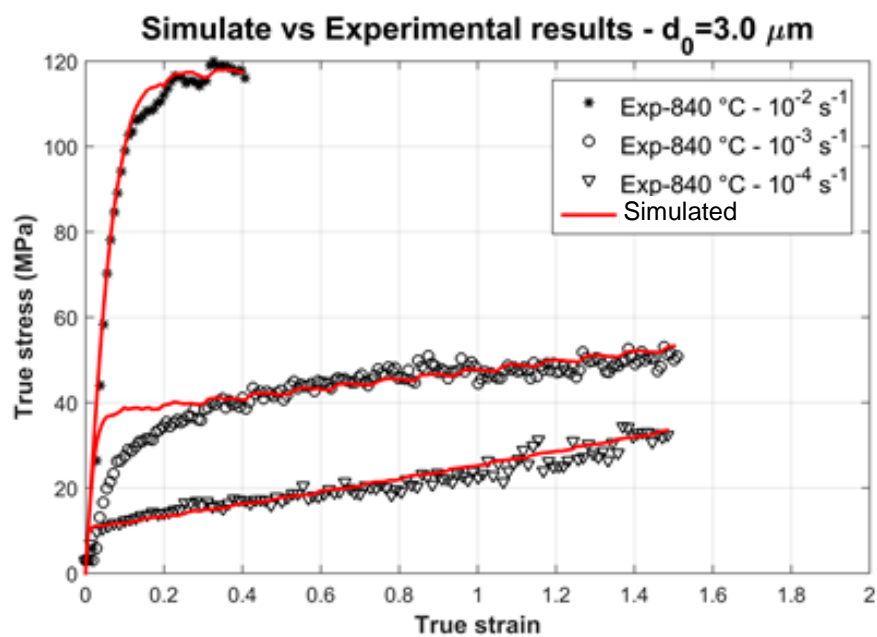


Figure 5-7 - Computed Stress-strain data vs Experimental results at a temperature of 840 °C and initial grain size of  $d_0=3.0 \mu\text{m}$

The Figure 5-8 presents the true stress-true strain predicted by the behaviour model at a temperature 840 °C and strain rate from  $10^{-2} \text{ s}^{-1}$  to  $10^{-4} \text{ s}^{-1}$  for starting grain size of  $d_0 = 4.9 \mu\text{m}$ . In this case, the model gives reasonably good prediction knowing that the tests performed on this starting microstructure are not used to achieve the identification process of the model parameters. In this simulation, only the initial grain size was modified in the set of parameters.

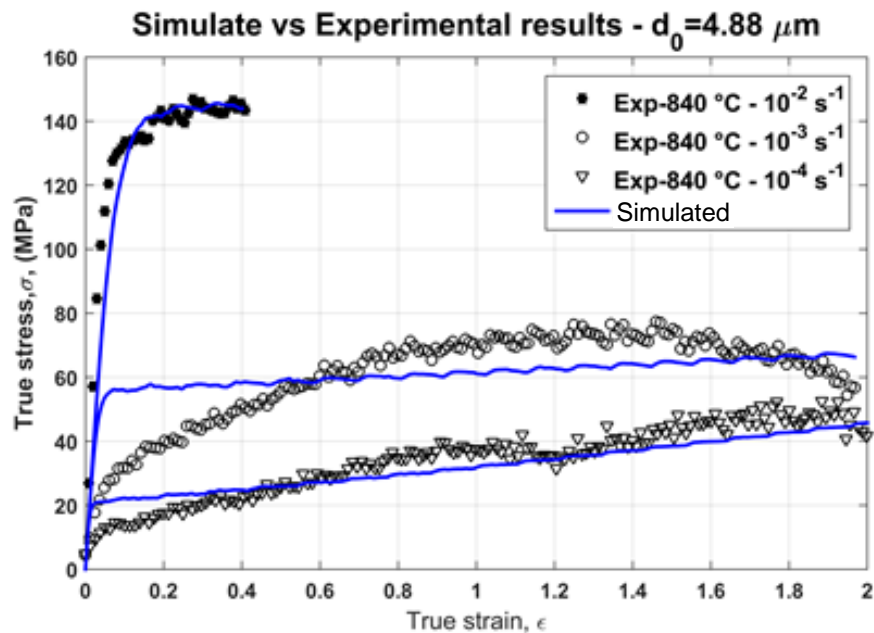


Figure 5-8 - Computed Strain-Stress data vs Experimental results at a temperature of 840 °C and initial grain size of  $d_0 = 4.9 \mu\text{m}$

This part was devoted to the development of a thermomechanical behaviour model able to take into account various starting microstructures and their evolutions with time, temperature and deformation. The model parameters were identified from two starting microstructures (0.5 and  $3 \mu\text{m}$ ) and then the predictions were extrapolated to a third one ( $4.9 \mu\text{m}$ ). The results show model predictions in quite a good agreement with experiment whatever the microstructure and the test conditions investigated. In the sequel, the multiaxial model formulation described above is implemented in a Finite Element Method (FEM) code in order to simulate a superplastic blow forming test. The objective is to validate the model response under a multiaxial loading path.

## 6. SUPERPLASTIC BLOW FORMING

Superplastic forming consists a relatively easy way to take advantage of the material behaviour for manufacturing purposes. For that reason, blow forming process is selected as experimental forming of Ti-6Al-4V alloy. For that, a single sheet laid on a female die and subjected to gas pressure is considered. It results in a formed part with the die configuration. Then, blow forming is a pressurized forming process which is widely used to produce complex shapes using superplastic alloys.

The main goals of that chapter are to evaluate the numerical behaviour modelling accuracy within a real superplastic forming through a blow forming.

In this process, the sheet is added inside a press and tightly clamped around its periphery and gas pressure is applied on its surface. After that, an inert atmosphere of Argon gas is required in the forming chamber, for both pressurization and maintenance of protective atmosphere. The modelling behavior's parameters were used for pressure-time profile to achieve complete adaptation of the metal sheet of 3 mm thickness to the die surface at a controlled rate of deformation.

### 6.1. EXPERIMENTAL PROCEDURE

Blanks of a Ti-6Al-4V alloy sheet were used for the superplastic blow forming. The material used is similar to the alloy already presented in Chapter 3 of this thesis. It has 3 mm thickness and an initial average grain size of 3.0  $\mu\text{m}$  (Figure 6-1). The experimental and numerical modelling of the superplastic forming were carried out with the following equipment, material and devices to simulate the bulge forming experiments:

- Ti-6Al-4V alloy sheet as specimens with starting grain size 3.0  $\mu\text{m}$ ;
- Press Machine for superplastic forming (Placed at LEL-IPT laboratory);
- ABAQUS 6.12 software for numerical analysis.



Figure 6-1 – Ti-6Al-4V sheet Blank

#### 6.1.1. Press Machine

The forming procedure was carried out in the IPT - Lightweight Structures Laboratory facility, in São José dos Campos, Brazil. The superplastic forming press machine used in the experimental test as seen in Figure 6-2, works with a system range of 15 to 150 metric Ton (from 147 to 1470 kN) of clamp force, and has a work area of approximately 760 × 860 mm. The gas pressure, which presses the blank against the die, has a range of 1 to 40 bar, and can work with gas injection on both sides of the blank.

One of the main worry was during the forming process to keep a low strain rate, to prevent some grain deformation or grain coarsening and, thus, making all the superplastic forming process through grain boundary sliding mode.

The furnace is assembled around the die sets and fixed to the bottom platen of the press. The top side of the furnace is covered by a thick insulation of ceramic fibre to prevent any heat loss.

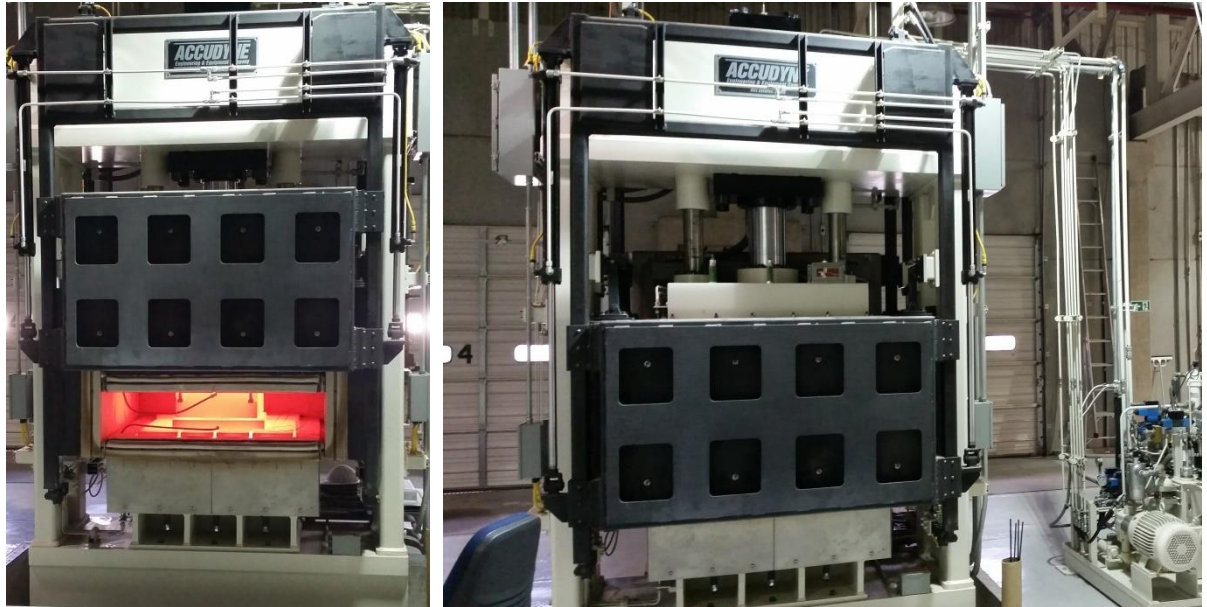


Figure 6-2 – IPT Lightweight Structures Laboratory's superplastic forming machine

The Figure 6-3 shows the images parts of blow forming bulge testing tooling parts used during superplastic tests at IPT Lightweight Structures Laboratory at Sao Jose dos Campos - SP.

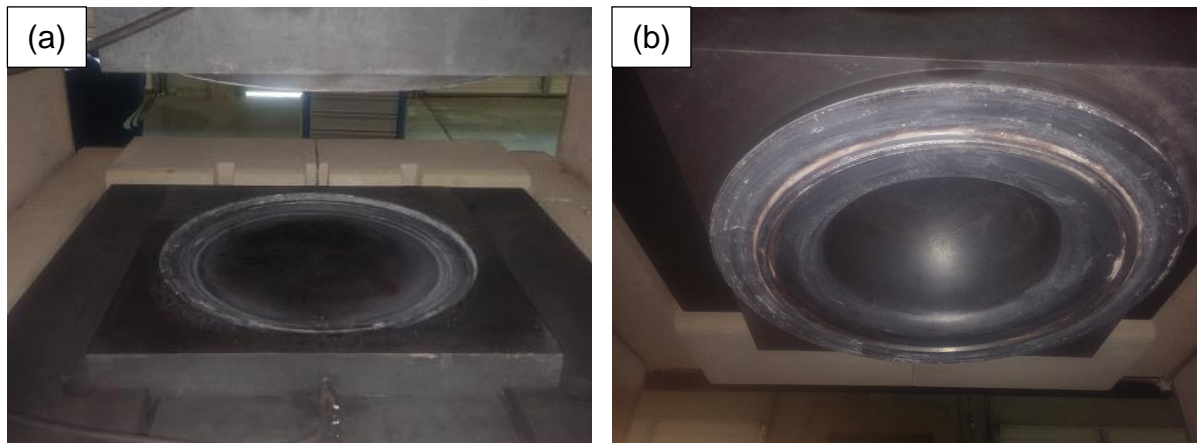


Figure 6-3 – Blow forming bulge testing tooling parts: bottom-die (a) and top die (b)

The Figure 6-4 presents a schematic diagram of the entire experimental set-up for the superplasticity testing machine. The bottom-die where located the gas chamber is placed to the back-up plate and this die assembly is mounted on the top platen of the press.

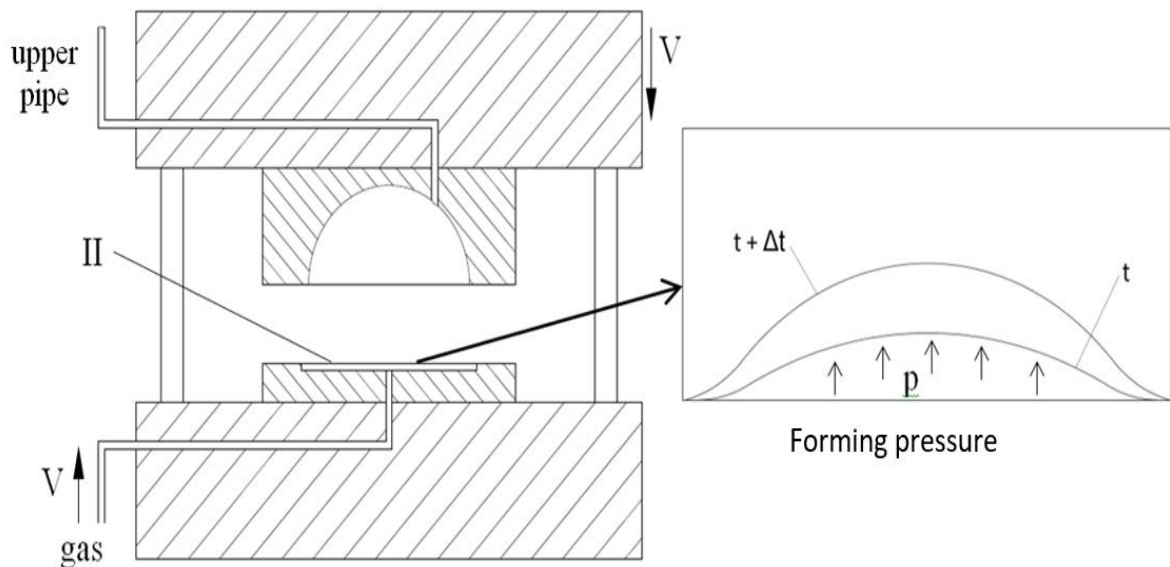


Figure 6-4 – Schematic superplastic press and forming process

The forming process includes the following six steps procedure presented hereafter:

- I. Initially the press was heated until reach the desirable temperature in this case 840 °C, in time about 27,000 s (see Figure 6-5).
- II. The blank disk, that is compatible with the SPF tool, was coated with boron nitride to avoid the part sticking in metal tooling, as a recommendation of the machine's manufacturer. Furthermore, previous trials of forming without boron nitride have led to difficulties to extract the formed sheet from the die;
- III. The purge process was started, releasing argon from the upper pipe, the press was opened and the part was put inside it;
- IV. The homogeneous time which is necessary for the blank to reach the desirable temperature but that measure was not taken account due to temperature system installed in the press which not equipped with this dispositive.

- V. The upper part of the press was sent down to clamp the blank's edge, to ensure a good draw bead contact or, in other words, to seal the blank against the die and prevent the gas to escape;
- VI. Finally, the gas flow followed the pressure versus time curve and the part was formed.

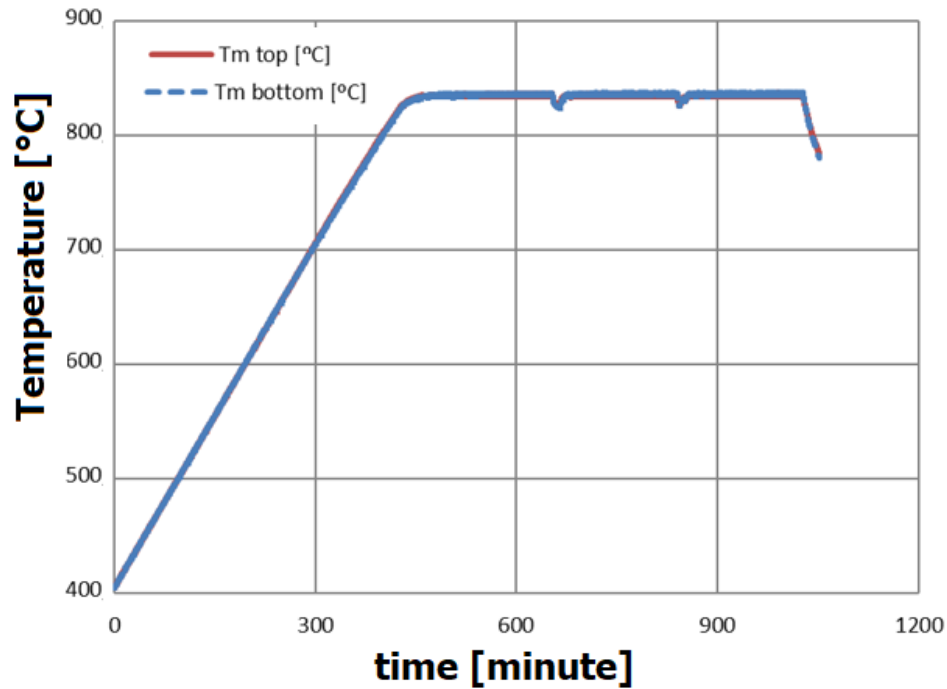


Figure 6-5 – Typical thermal cycle for one of the superplastic forming process

## 6.2. RESULTS OF SUPERPLASTIC FORMING

- **Verification and Mukherjee's pressure equation**

Superplastic forming is highly sensitive to strain rate thus it is essential to generate an accurate pressure-time profile to maintain the desired strain rate, during deformation. Mukherjee Equation (6-1) devised a relationship based on biaxial stress conditions to maintain a constant strain rate during superplastic blow forming of a hemisphere.

$$P = 4 \frac{S_0}{a} \bar{\sigma} \exp(-\dot{\epsilon}t) \left[ \bar{\sigma} \exp(\dot{\epsilon}t) (1 - \bar{\sigma} \exp(-\dot{\epsilon}t)) \right]^{\frac{1}{2}} \quad (6-1)$$

Where: P – pressure,

$\bar{\sigma}$  - Effective stress,

$\dot{\epsilon}$ - Effective stress,

t – time,

S<sub>0</sub> - Initial sheet thickness,

a - Die radius

From the point of view of data input, elastoplastic modified model works with the traditional Norton-Hoff equation format, as shown in equation (6-2)., where  $\sigma$  is the stress.

$$\sigma = K\dot{\epsilon}^m \quad (6-2)$$

The analysis used commercial finite element code, Simulia Abaqus 6.12, was used for the numerical calculations. It was observed that several procedures must be performed in software packages to guarantee a correct representation of the forming process.

The blank is composed of S4R shell elements. The free forming region of the sheet is 453 mm in diameter, with a 157-mm flange around it, and the initial sheet thickness is 3.0 mm.

Taking advantage of the symmetry, a quarter of the blank is modelled using 885 quadrilateral elements (M3D4). These elements are fully integrated bilinear membrane elements. The sheet is clamped along the circumference and symmetric boundary conditions are applied along the axis of symmetry.

The flat initial configuration of the membrane model is entirely singular in the normal direction, unless it is stressed in biaxial tension. This problem is overcome by applying a very small initial biaxial stress on the surface of the sheet.

They had all degrees of freedom fixed in the circular edge, simulating the machine clamp force, and the friction coefficient imposed for the contact between the blank and the rigid die was assumed as 0.1.

The material parameters used in the constitutive model are those obtained at 840°C and were found from tensile tests in this work are given in (VELAY et al., 2016). In addition, the experimental work of (HAMILTON, 1984) was used to calibrate these models.

It was necessary to divide the process into two parts: in the first one, the material is modelled as linear elastic, and in the final step, as viscoplastic. All the material data used in the numerical procedures were considered for a temperature of 840 °C.

- STEP 1
  - The initial application of the pressures is assumed to occur so quickly that it involves purely elastic response. This is achieved by using the \*STATIC procedure
- STEP 2
  - The creep response is developed in a second step using the \*VISCO procedure

From the point of view of data input, ABAQUS worked with elastoplastic modified equation format, as described early in Chapter 5. Abaqus, on the other hand, does not support this type of input, making it necessary to adapt a mechanical behaviour model including a grain growth effect through a CREEP user subroutine before launching the simulation (VELAY et al., 2016).

The information that should be obtained through the numerical models is the gas pressure curve that may be applied to the blank, not only to form the part, but also to keep the strain rate close to  $2.5 \times 10^{-4} \text{ s}^{-1}$ , which can ensure a superplastic behaviour. To be sure that the finite element data was reliable, an analytical calculation for the optimal pressure cycle was carried out.

To reach those conditions, the curve obtained through of characterization material presented in Chapter 5, was adjusted to linear function – the only type of curve that is accepted as an input by the hot press control system (Figure 6-6).

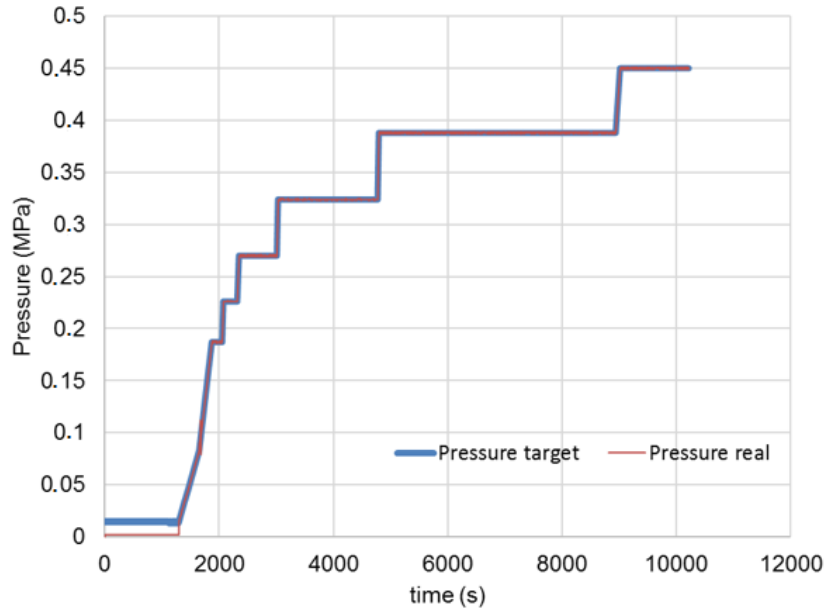


Figure 6-6 – Pressure control: pressure target vs real pressure

Figure 6-7 present the variation of strain versus time curve calculated on the hemispherical dome by ABAQUS 6.12 simulating.

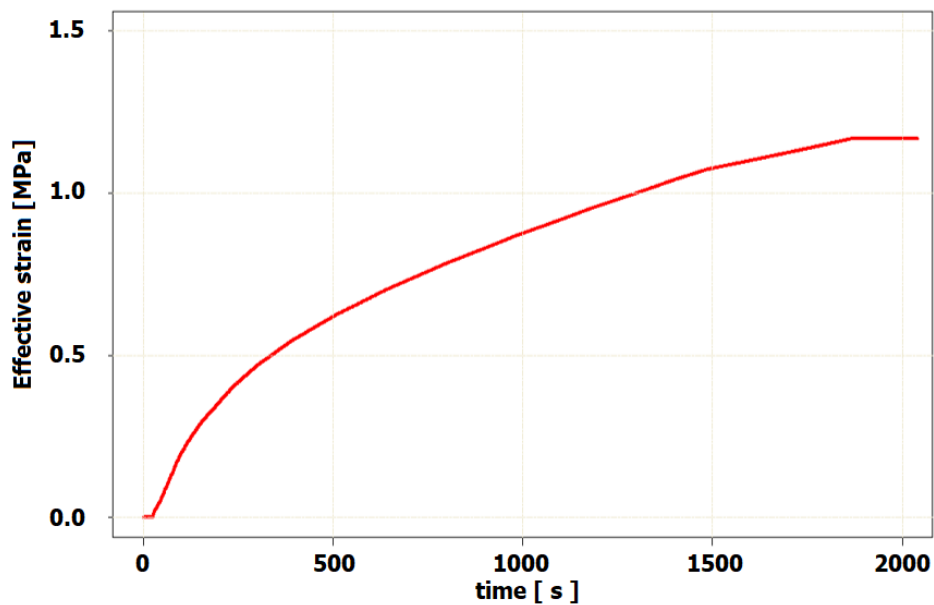


Figure 6-7 – Effective strain versus time in the hemispherical dome for the two models

The main results are presented in the Figure 6-8 for the FEM numerical simulation of the superplastic bulge forming.

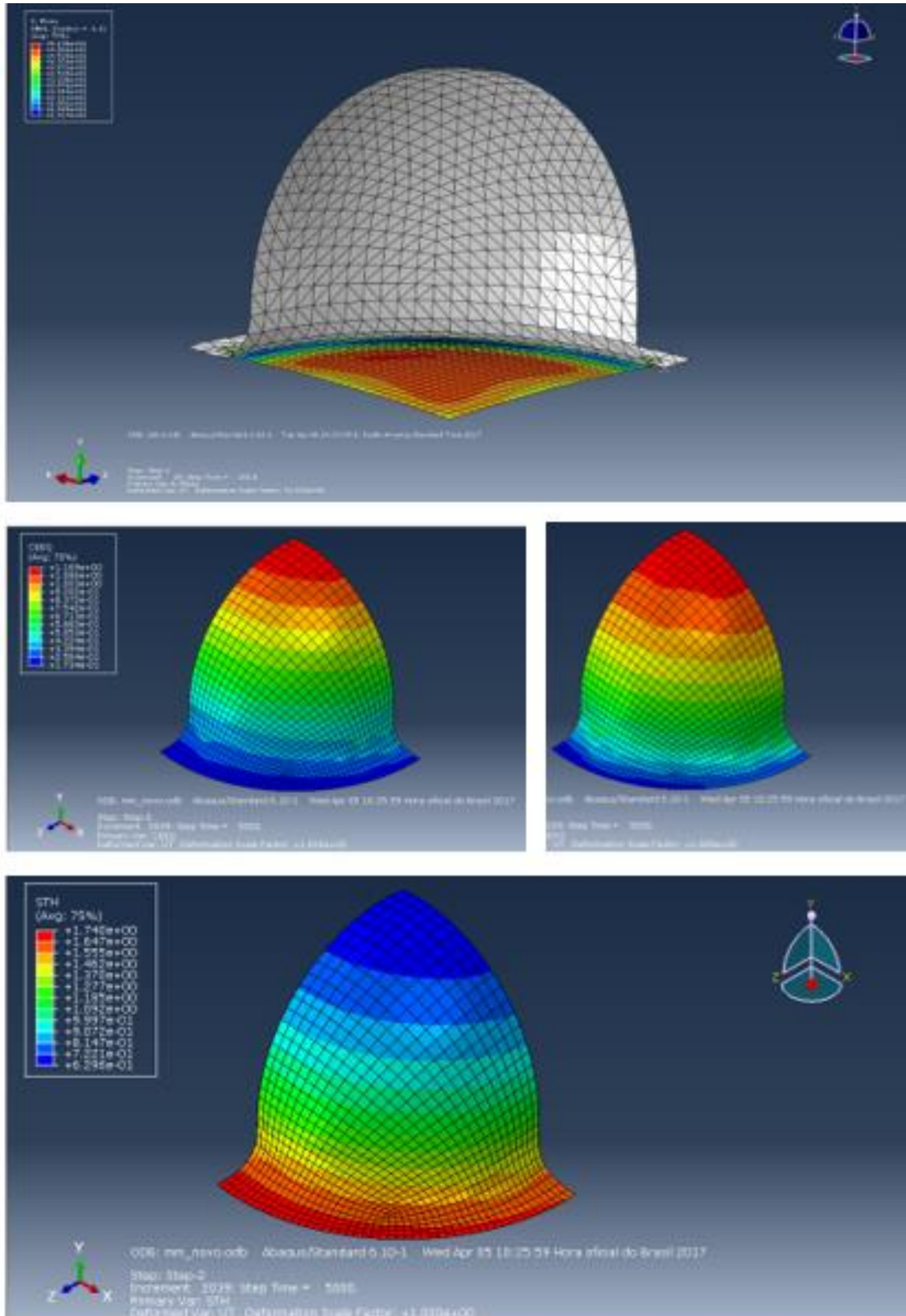


Figure 6-8 – Numerical simulation results of behaviour law with ABAQUS software

### 6.3. MEASUREMENT THICKNESS ANALYSIS

The main goal this analysis is to compare and discuss the variation of thickness during forming process sheet. For that, thickness measurements employed two different methods, a non-contact optical 3D measuring system by ATOS ScanBox®<sup>2</sup> and a second one by ultrasonic thickness measurement seen in Figure 6-9 and Figure 6-10.

#### 6.3.1. ATOS ScanBox®

The equipment used is ATOS ScanBox systems which is the ATOS 3D scanner. The ATOS sensors provide full-field 3D coordinates for each individual measurement. Up to 16 million independent measuring points are captured within 1 to 2 seconds. The measuring data is characterized by very high detailed reproduction, thus also enabling very small component features to be measured (GOM, 2017).

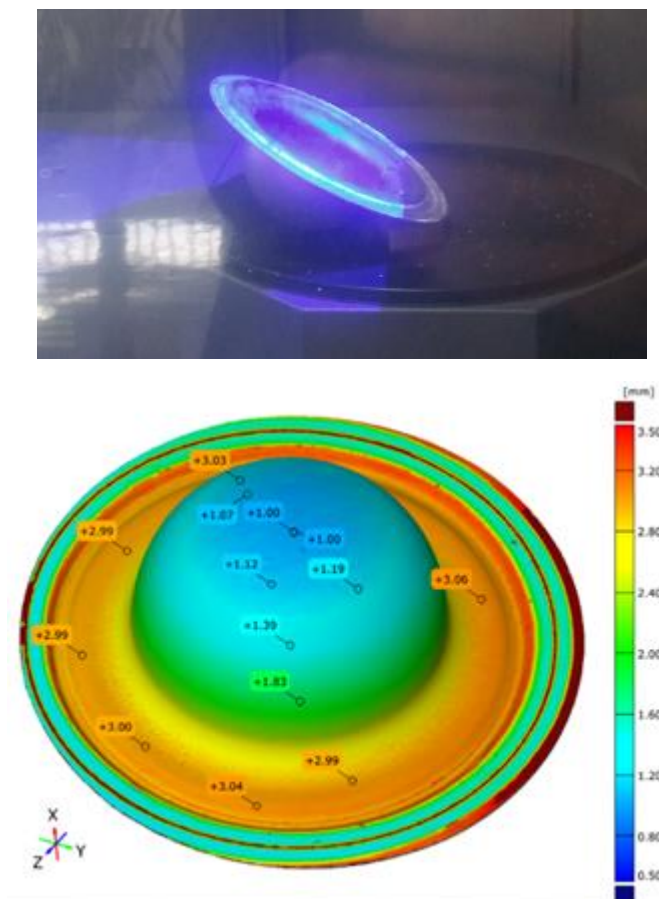


Figure 6-9 – Thickness measurement by digital image correlation

<sup>2</sup> Website: <http://www.gom.com/metrology-systems/atos-scanbox.html>

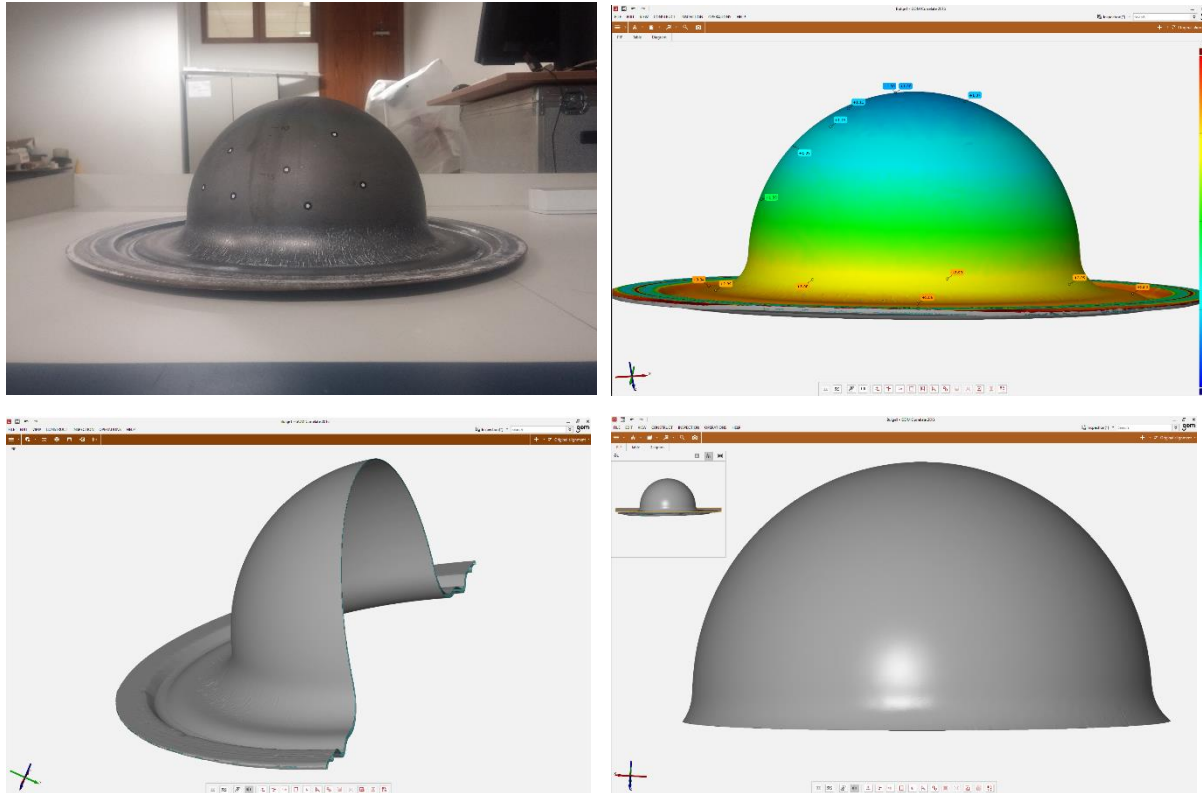


Figure 6-10 – Position of tool measure for thickness evaluation.

### 6.3.2. Ultra Sound Inspection

The superplastic formed part was inspected with ultrasonic scanning to verify if the process guaranteed homogeneous thickness reduction. The equipment used was an Olympus Omniscan SX: type UT, mode pulse-echo, sound velocity of 6172.8 m/s, 27 dB Gain; the transducer generated longitudinal waves at 5MHz. 10 points were measured over its half cross-section in four different meridians.

Position 1 ( $x = 0$  mm) is the top of the dome and position 10 ( $x = -105$  mm) is its base, just before the smaller radius.

The observed deviation between the numerical and experimental results increases as the  $x$  position decreases, showing that the model represents the top part of the dome with lower accuracy.

The error bar, on the other hand, has the opposite behaviour, decreasing as the position in  $x$  decreases.

The Figure 6-11 illustrates schematically a sample which were inspected at IPT laboratory with ultrasonic scanning to verify the thickness distribution on the dome. For this, the equipment used was an Olympus Omniscan SX: type UT, mode pulse-echo, sound velocity of 6172.8 m/s, 27 dB Gain and transducer generates longitudinal waves at 5MHz. The measurements consist in 18 points over its cross-section.

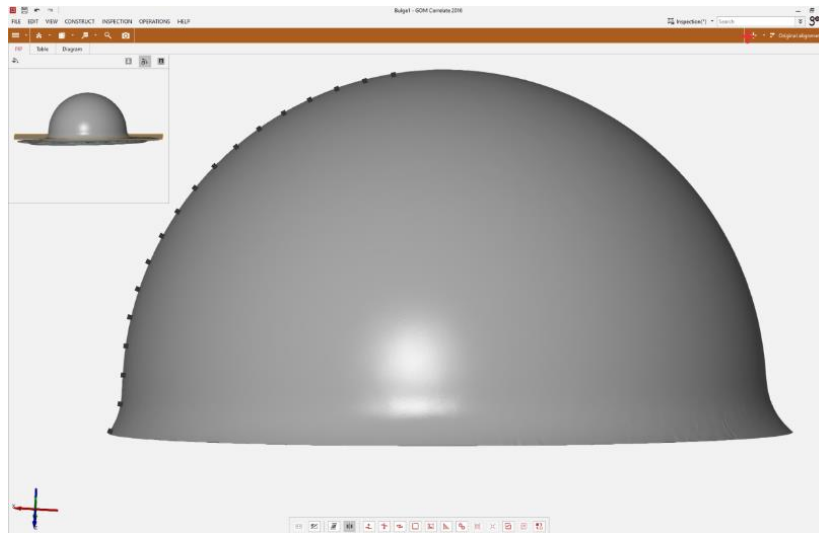


Figure 6-11 - Ultrasound inspection equipment and measured points in detail.

The Figure 6-12 shows the measurement process and the results, with a comparison obtained by finite element calculation

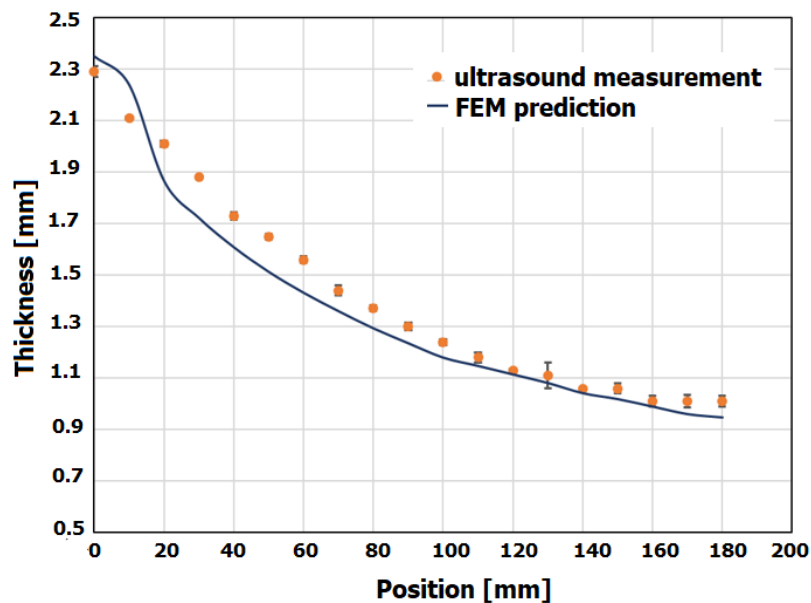


Figure 6-12 - Ultrasound inspection (a) results, and comparison with numerical data (b).

#### 6.4. EXPERIMENTAL GRAIN SIZE DISTRIBUTION

A statistical approach was employed to carry out the analysis of the grain size distribution and its grain evolution, aiming to see where the most common values fall in a measurement scale, and how much variation occurred in the superplastic microstructure of the superplasticity deformed (Figure 6-13 and Figure 6-14).

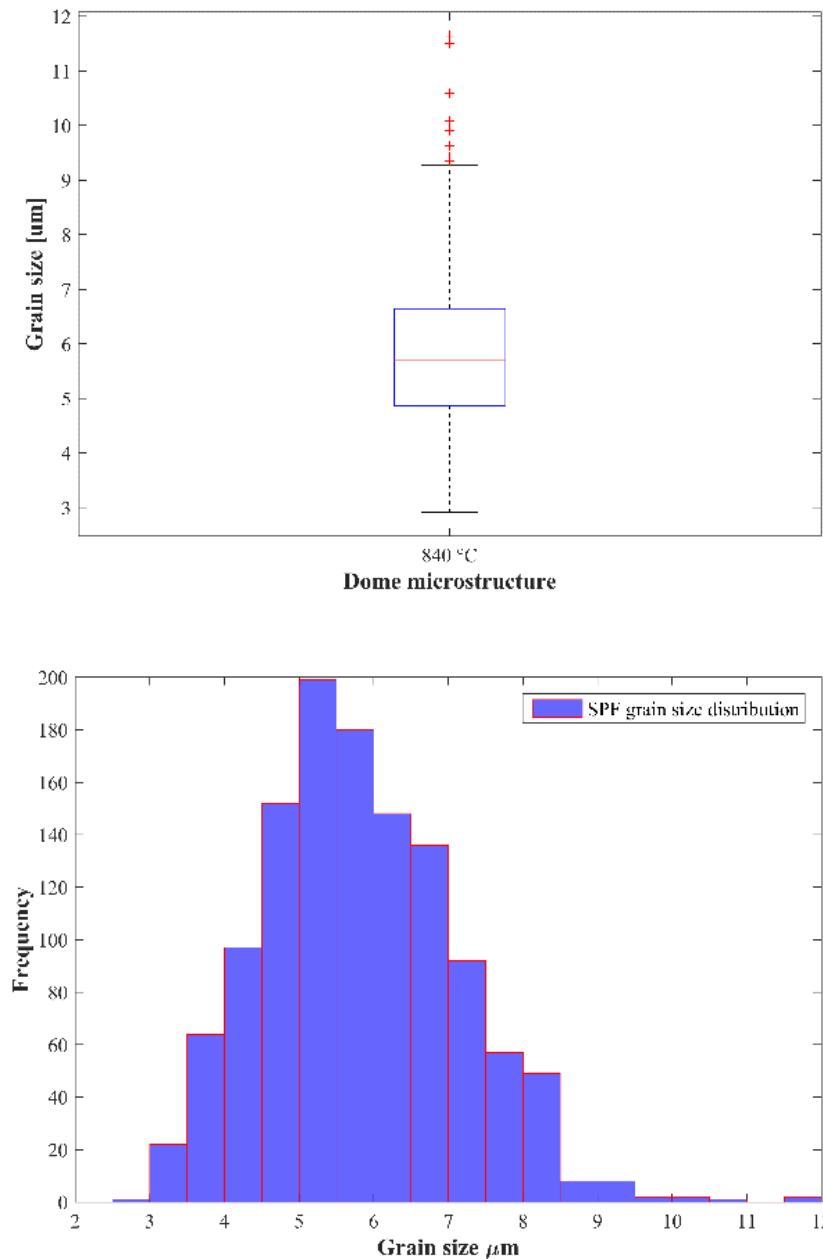


Figure 6-13 – The average value of grain growth size distribution at 840 in the superplastic bulge forming °C was about  $6.0 \pm 0.35 \mu\text{m}$

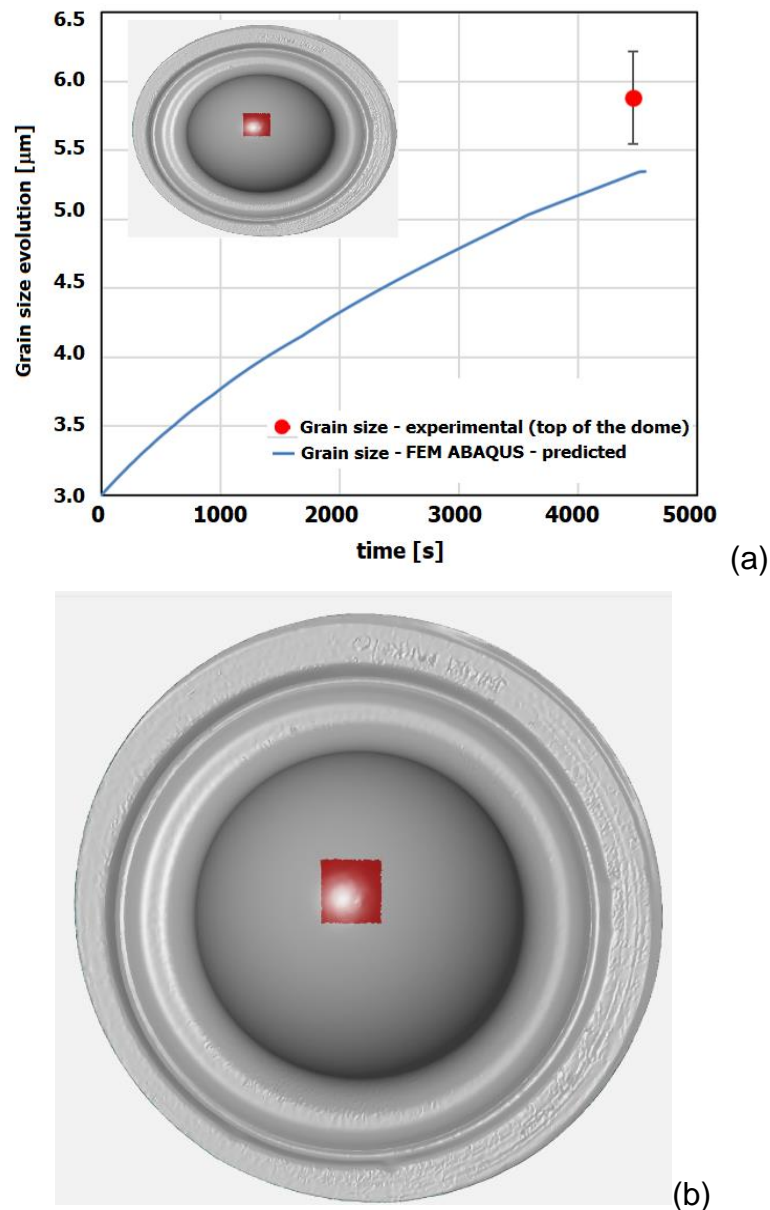


Figure 6-14 – Comparison between experiment and numerical simulation at 840 °C  
 (a) and in red, region where the shows measurement is performed region on piece  
 (b)

The metallographic examination of the microstructure formed at 840 °C after superplastic forming (Figure 6-15) test as seen the detail (Figure 6-15c) a  $\alpha$ -grain which was probably, was transformed during the forming temperature which it imposed a change of microstructure. The deformation of the material caused the refinement of  $\alpha$ -phase lamellae distributed within the  $\alpha$ - $\beta$ -phase matrix (Figure 6-15d). That effects might have occurred during the rapid cold process above at 840 °C which promoting the change of  $\alpha$ -grain and also the lamellae in the colony structure indicated by arrow as seen in detail in Figure 6-15.

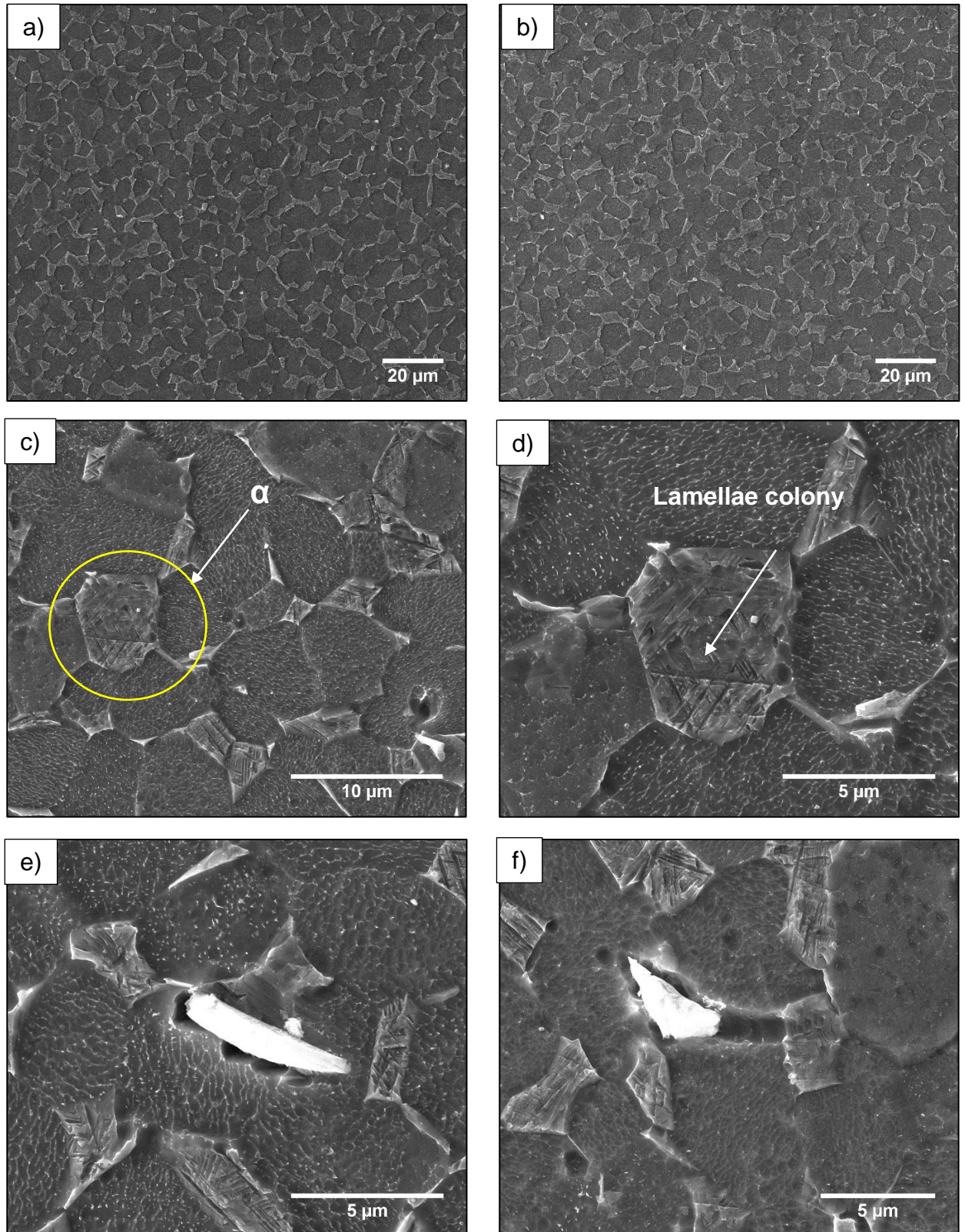


Figure 6-15 – FEGSEM BSE mode micrographs of Ti-6Al-4V alloy microstructure post-mortem samples experimental test at 840 °C: microstructure aspect showing equiaxed grains after bulge test (a) and (b); in detail can see ultra fine lamellae structure formed during colling (c) and (d); The white structure deposited by metallographic procedure (e) and (f).

## 7. CONCLUSIONS AND PERSPECTIVES

The approach of the “dynamic” condition by Gleeble 3800 physical simulator and MTS machine for tensile test allowed assessed the mechanical behaviour in a hot forming and superplastic process was developed through that method allowed to consider, several strain rate and wide temperature range.

The results showed that highest strain rate i.e.:  $0.1 \text{ s}^{-1}$  and  $10^{-2} \text{ s}^{-1}$  had a significant influence on the time of fracture of the material studied while lowest the strain rate was much better for sheet forming because it improved the ductility of the material. Temperature also had a significant influence on formability. In general, the material was the better performed at higher the temperature. Hence in that study point that slow strain rate associated at higher temperature improve the behavioral material.

The thermomechanical tensile test on the Gleeble 3800 and MTS machine allowed to notice a microstructural evolution for initial average grain size  $4.9 \mu\text{m}$  when used in elevated temperature (850 to 950 °C) and slow strain rate ( $10^{-3} \text{ s}^{-1}$   $10^{-4} \text{ s}^{-1}$ ). That set up conditions led to formation of more elongated and refined  $\alpha$  grains in the microstructure of material resulting in considerable rise of elongation.

The tensile test on MTS machine and Gleeble 3800 allowed to be assessed the mechanical behaviour in the “dynamic” condition and find out the parameters such as viscosity, hardening flow stress introduced in the constitutive equations as part of the behaviour law studied.

The superplastic tests on the MTS machine of materials with initial average grain size of 0.5; 3.0 and  $4.9 \mu\text{m}$  showed a grain boundary sliding as mechanism of deformation predominant when exposed at high temperature and slow strain rate as showed on the microstructural observations by SEM analysis.

The superplastic behaviour of Ti–6Al–4V Titanium alloy was investigated under hot forming conditions regarding different starting microstructures with an average grain size of  $0.5 \mu\text{m}$  and  $3.0 \mu\text{m}$  and  $4.9 \mu\text{m}$ . A temperature ranges from 700 to 950 °C and strain rates between  $10^{-4} \text{ s}^{-1}$  and  $10^{-2} \text{ s}^{-1}$  were considered.

The “static” test carried out by ageing thermal treatment allowed to investigate the microstructural behaviour of the materials when exposed to thermal energy similar to tensile tests. The results observed from microstructural analysis by SEM showed a coarsening for all initial grain size (0.5; 3.0; 4.9  $\mu\text{m}$ ). Beyond “static” test assessed to find out the parameters microstructural related to behaviour law studied.

The modelling behaviour indicated that the strain-stress response exhibits a viscous flow dependent on the test temperature and that had affected into the initial microstructure and in the grain growth for a microstructure of initial grain size of 4.9  $\mu\text{m}$  causing a strain hardening which was observed for the long-time period test. The parameters of a grain growth model were identified, it successfully describes the evolutions predicted for measurements performed in the present study.

A non-isothermal formulation of the model allows to accurately predict test conditions not considered in the identification process. Moreover, some predictions with different initial grain sizes are addressed.

The internal variable related to grain growth was introduced into the mechanical model through the viscous flow and the hardening. The stability of the constitutive equations was investigated under uniaxial conditions by the prediction of the necking and by the analysis of the shrinkage rate against the normalized cross-sectional area.

Compared to visco-plastic and Semiatin models, the new constitutive model can predict the accurately superplastic deformation behaviour due to the consideration of the microstructural evolution of Ti-6Al-4V alloy.

The analysis of pressure curve and tensile test on the press machine allowed to find the ideal conditions for superplastic forming dome and modelling behaviour mechanical aimed to predict the thickness of the formed part.

The forming of the titanium dome by superplastic condition and analysis of the process was carried out to obtain the ideal pressure curve and to predict the thickness of the formed part; an ultrasound inspection was used to compare the formed part with the numerical data.

The forming process resulted in a dome with the desired geometry, but the thickness was below the predicted value. Boron nitride shows to be an efficient technique to prevent the formed part from sticking to the tool. When the press was

opened after the forming process, the part was already detached from the die. Furthermore, the cooling system using a water tank prevented oxidation, although microstructural changes or residual stresses were not studied.

A Finite Element analysis of superplastic gas-blow forming was carried out using a modified microstructure-based constitutive model. Extension of the model to more practical loading conditions and applying it to material are currently under investigations.

The material constant  $c$  also increases as temperature increases, which means strain rate has larger effect on hardening rate of large strain stage at higher temperature. The strain rate sensitive exponent  $m$  increases as temperature increases from 870 to 950 °C, which indicates that the Ti-6Al-4V has better necking resistance at 950 °C.

## FUTURE WORKS

The present dissertation has demonstrated that using accurate modelling behaviour SPF forming and hot work can predict mechanical the behaviour for Ti-6Al-4V. Based-on this research can be indicate the following future woks:

- To improve the physical content of the constitutive equations, it should be interesting to determine a phenomenological equation for each mechanism, like dislocation, glide, diffusion creep, grain boundary sliding and for each test condition try to fit the curves using a combination of these equations. The influence of the different mechanisms in the new equation will be determined by weight factors.
- To apply this approach about microstructure evolution for different models proposed in a finite element code and comparison between experimental results and a 3D biaxial model.
- To study the influence of a microstructural evolution on the compression and/or torsion deformation mode regarding the initial microstructure.

## PUBLICATIONS LIST

### CONFERENCE

**COBEF 2017 - July 26th - 29th - Joinville - Brazil.**

**SANTOS, MARCIO**; BATALHA, GILMAR . MECHANICAL BEHAVIOR OF THE Ti-6Al-4V TITANIUM ALLOY WITH MICROSTRUCTURAL EVOLUTION MODELING UNDER HOT AND SUPERPLASTIC CONDITIONS. In: Congresso Brasileiro de Engenharia de Fabricação, 2017, Joinville. Anais do IX Congresso Brasileiro de Engenharia de Fabricação, 2017. doi://10.26678/ABCM.COBEF2017-0395

### EUROSPF 2016

**SANTOS, M.**, VELAY, V.; VIDAL, V; BERNHART, G; BATALHA, G; MATSUMOTO, H. Mechanical behavior of Ti-6Al-4V titanium alloy with microstructural evolution modeling under hot and superplastic conditions.

[https://eurospf2016.sciencesconf.org/data/pages/Book\\_of\\_Abstratcs\\_1.pdf](https://eurospf2016.sciencesconf.org/data/pages/Book_of_Abstratcs_1.pdf)

### AMPT 2015

M.W.B. Santos, V. Velay, G. Bernhart, M. Stipkovic Filho and G.F. Batalha. **The influence of low strain rate and high temperature on microstructural evolution of ti-6al-4v titanium alloy.** Advances in Materials and Processing Technologies – AMPT – Madrid

[http://www.ampt2015.org/contxt/programme/default\\_session.asp?node=&day=tuesday&sessionID=39](http://www.ampt2015.org/contxt/programme/default_session.asp?node=&day=tuesday&sessionID=39)

### PERIODIC REVIEW

#### Material Science and Engineering Technology

**DOS SANTOS, M. W.**; VELAY, V. ; VIDAL, V. ; BERNHART, G. ; BATALHA, G. F. ; MATSUMOTO, H. . Mechanical behavior of a Ti-6Al-4-V titanium alloy with microstructural evolution modeling under hot and superplastic conditions. MATERIALWISSENSCHAFT UND WERKSTOFFTECHNIK, v. 48, p. 952-961, 2017. DOI: 10.1002/mawe.201700040

CARUNCHIO, A. F. ; BATALHA, M. H. F. ; PEREIRA, D. A. ; RESENDE, H. B. ; BATALHA, A. E. F. ; TOLOCZKO, F. R. ; **SANTOS, M. W. B.** ; BATALHA, G. F. . Numerical and experimental integration in analysis of a superplastic forming. MATERIALWISSENSCHAFT UND WERKSTOFFTECHNIK, v. 48, p. 962-968, 2017. DOI: 10.1002/mawe.201700032

## REFERENCES

AKSENOV, S.; CHUMACHENKO, E.; LOGASHIMA, I. **Experimental Investigation of Ti-Al-V Alloy Superplastic Behavior**. 21st International Conference on Metallurgy and Materials Proceedings. **Anais...Brno**: 2012

ALABORT, E.; PUTMAN, D.; REED, R. C. Superplasticity in Ti-6Al-4V: Characterisation, modelling and applications. **Acta Materialia**, v. 95, p. 428–442, 2015.

ARIELI, A.; ROSEN, A. Superplastic deformation of Ti-6Al-4V alloy. **Metallurgical Transactions A**, v. 8A, p. 1591–1596, 1976.

AKSENOV, S.; CHUMACHENKO, E.; LOGASHIMA, I. **Experimental Investigation of Ti-Al-V Alloy Superplastic Behavior**. 21st International Conference on Metallurgy and Materials Proceedings. **Anais...Brno**: 2012

ALABORT, E.; PUTMAN, D.; REED, R. C. Superplasticity in Ti-6Al-4V: Characterisation, modelling and applications. **Acta Materialia**, v. 95, p. 428–442, 2015.

AMBROGIO, G.; FILICE, L.; GAGLIARDI, F. Formability of lightweight alloys by hot incremental sheet forming. **Materials and Design**, v. 34, p. 501–508, 2012.

ARIELI, A.; ROSEN, A. Superplastic deformation of Ti-6Al-4V alloy. **Metallurgical Transactions A**, v. 8A, p. 1591–1596, 1976.

BABU, B. **Physically Based Model for Plasticity and Creep of Ti-6Al-4V**. 2008. 94 p. Doctoral Thesis. Luleå University of Technology. Mechanical Engineering Division of Material Mechanics, Luleå Sweden, 2008.

BACKOFEN, W. A.; TURNER, I. R.; AVERY, D. H. Superplasticity in an Al-Zn Alloy. **Transactions ASM**, v. 57, n. 57, p. 9914–9919, 1962.

BALL, A.; HUTCHISON, M. M. Superplasticity in the aluminum-zinc eutectoid. **Material Science Journal**, v. 3, p. 1–7, 1969.

BARNES, A. J. Superplastic Forming 40 Years and Still Growing. **Journal of Materials Engineering and Performance**, v. 16, n. 4, p. 440–454, 12 Jun. 2007.

BELLET, M. et al. **Modelisation Numerique du Formage Superplastique de Toles**. Doctoral thesis. Ecole nationale suprieure des mines de Paris, 2010.

BHATTACHARYYA, D. et al. A study of the mechanism of  $\alpha$  to  $\beta$  phase transformation by tracking texture evolution with temperature in Ti-6Al-4V using neutron diffraction. **Scripta Materialia**, 2006.

BONET, J. et al. Simulating superplastic forming. **Computer Methods in Applied Mechanics and Engineering**, v. 195, n. 48–49, p. 6580–6603, 2006.

BRUSCHI, S. et al. Testing and modelling of material behaviour and formability in sheet metal forming. **CIRP Annals - Manufacturing Technology**, v. 63, n. 2, p. 727–749, Jul. 2014.

BUFFA, G.; FRATINI, L.; MICARI, F. Mechanical and microstructural properties prediction by artificial neural networks in FSW processes of dual phase titanium alloys. **Journal of Manufacturing Processes**, v. 14, n. 3, p. 289–296, 2012.

CAO, J.; LIN, J. A study on formulation of objective functions for determining material models. **International Journal of Mechanical Sciences**, v. 50, n. 2, p. 193–204, Feb. 2008.

CHANDRA, N. Constitutive behavior of superplastic materials. **International journal of non-linear mechanics**, v. 37, n. 3, p. 461–484, Apr. 2002.

CHEONG, B. H.; LIN, J.; BALL, A. A. Modelling of hardening due to grain growth for a superplastic alloy. **Journal of Materials Processing Technology**, v. 119, p. 361–365, 2001.

CHEONG, B. H.; LIN, J.; BALL, A. A. Modelling the effects of grain-size gradients on necking in superplastic forming. **Journal of Materials Processing Technology**, v. 134, n. 1, p. 10–18, Mar. 2003.

COMLEY, P. Multi-rate Superplastic Forming of Fine Grain Ti-6Al-4V Titanium Alloy. **Journal of Materials Engineering and Performance**, v. 16, n. 2, p. 150–154, 1 Mar. 2007a.

COMLEY, P. N. ASTM E2448—A Unified Test for Determining SPF Properties. **Journal of Materials Engineering and Performance**, v. 17, n. 2, p. 183–186, 12 Dec. 2007b.

DANG, P.; CHANDRA, N. A MICROMECHANICAL MODEL FOR DUAL-PHASE SUPERPLASTIC MATERIALS. **Acta Materialia**, v. 46, n. 8, p. 2851–2857, 1998.

DEARNALEY, G.; WATKINS, R. **Titanium and its alloys. US Patent 4,465,524**, 1984.

DEHGHAN-MANSHADI, A. Effect of microstructural morphology on the mechanical properties of titanium alloys. **Journal of Physics: Conference Series** **240**, v. 12022, n. ICSMA-15, p. 1–5, 2010.

DESHMUKH, P. V. **Study of superplastic forming process using finite element analysis**. 2003. p 96. Doctoral Thesis. University of Kentucky, Kentucky, 2003.

DNPM 2015, Departamento Nacional de Produção Mineral. Sumário Mineral 2015. Technical report. Brasília. DNPM. 2015. v. 35, p. 135, 2015 Available in: <http://www.dnpm.gov.br/dnpm/sumarios/sumario-mineral-2015>

DOMKIN, K. **Constitutive models based on dislocation density: formulation and implementation into finite element codes**. 2005. p. 168, Doctoral Thesis. Luleå University of Technology. Mechanical Engineering Division of Material Mechanics, Luleå Sweden, 2005.

DONACHIE, M. J. Titanium: A Technical Guide. In: ASM METALS PARK (Ed.). . 2nd. ed. **ASM International**, 2000. p. 512.

FARIAS, A. D. E. **Avaliação do processamento por atrito linear em chapas da liga de titânio Ti-6Al-4V**. 2015. p 250. Doctoral Thesis. Escola Politécnica da Universidade de São Paulo, São Paulo, 2015.

GAO, F. et al. Rheological law and constitutive model for superplastic deformation of Ti-6Al-4V. **Journal of Alloys and Compounds**, v. 701, n. 37, p. 177–185, 2017.

GIBBS, G. B. Mém. Scient. Revue Metall. **Materials Science and Engineering**, v. 2, p. 269–273, 1967.

GIFKINS, R. C. Grain-boundary sliding and its accommodation during creep and superplasticity. **Metallurgical Transactions**, v. 7A, p. 1275, 1976.

GOM. **ATOS ScanBox - Optical 3D Coordinate Measuring Machine**. Available in: <http://www.gom.com/metrology-systems/atos-scanbox.html>. Access at: 28 mar. 2017.

GUANABARA JUNIOR, P.; BATALHA, G. F. Superplastic deformation and material parameters optimization: A BRIEF REVIEW. **64<sup>th</sup> ABM Annual Congress**. Belo Horizonte, 2009.

HAMILTON, C. H. Superplasticity in titanium alloys. **Superplast. Form.**, v. 24, n. 1, p. 123–130, 1984.

HART, E. W. Theory for flow of polycrystals. **Acta Metallurgica**, v. 15, p. 1545–1549, 1970.

INGELBRECHT, C. **Superplastic Deformation of Titanium Alloys**. 1985. p 151. Doctoral Thesis. University of Surrey, Materials and Structures Departement, Hampshire, 1985.

JOSHI, V. A. **Titanium alloys: an atlas of structures and fracture features**. 3<sup>th</sup> ed. v. 59. CRC press, 2006. ISBN 0-8493-5010-7

LANGDON, T. G. Grain boundary sliding as a deformation mechanism during creep. **Philosophical Magazine**, v. 22, p. 689–700, 1970.

LEYENS, C.; PETERS, M. **Titanium and Titanium Alloys: Fundamentals and Applications**. In Weinheim: 1st. ed. Wiley-VCH GmbH & Co. KGaA, Institute of Materials Research, 2003. ISBN: 3-527-30534-3

LI, G. Y.; TAN, M. J.; LIEW, K. M. Three-dimensional modeling and simulation of superplastic forming. **Journal of Materials Processing Technology**, v. 150, n. 1–2, p. 76–83, 2004.

LIN, J. Selection of material models for predicting necking in superplastic forming. **International Journal of Plasticity**, v. 19, n. 4, p. 469–481, 2003.

LIN, J.; DEAN, T. A. Modelling of microstructure evolution in hot forming using unified constitutive equations. **Journal of Materials Processing Technology**, v. 167, n. 2–3, p. 354–362, 2005.

LIN, Y. C.; CHEN, X.-M. A critical review of experimental results and constitutive descriptions for metals and alloys in hot working. **Materials & Design**, v. 32, n. 4, p. 1733–1759, Apr. 2011.

LIU, Y. et al. Assessment of the diffusional mobilities in bcc Ti-V alloys. **Journal of Alloys and Compounds**, v. 470, n. 1–2, p. 176–182, 2009.

MARTINEZ, N. O. **Optimization of superplastic forming production of Al-5083-SPF parts via finite element analysis**. 2012. p 178. Doctoral Thesis. Mondragon Unibertsitatea . Mechanical and Manufacturing Department, 2012

MATSUMOTO, H.; VELAY, V.; CHIBA, A. Flow behavior and microstructure in Ti–6Al–4V alloy with an ultrafine-grained  $\alpha$ -single phase microstructure during low-temperature-high-strain-rate superplasticity. **Materials & Design**, v. 66, Part B, n. 0, p. 611–617, 2015.

MAY, L. **Mechanical properties of ultrafine-grained Ti-6Al-4V ELI alloy processed by severe plastic deformation**. 2009. Doctoral Thesis. Universität Erlangen-Nürnberg, 2009.

MOTYKA, M. et al. Hot Plasticity of Alpha Beta Alloys. **Titanium Alloys - Towards Achieving Enhanced Properties for Diversified Applications**, p. 87–116, 2007.

MUKHERJEE, A. K. The rate controlling mechanism in superplasticity. **Materials Science and Engineering**, v. 8, n. 2, p. 83–89, 1971.

MUKHERJEE, A. K. Grain boundaries in engineering materials. **Walter J. L. et al**, v. 93, 1975.

MUKHERJEE, A. K. An examination of the constitutive equation for elevated temperature plasticity. **Materials Science and Engineering A**, v. A322, p. 1–22, 2002.

MUKHERJEE, A. K.; ZELIN, M. **Cooperative Grain Boundary Processes in Superplastic Flow**. Superplasticity in Advanced Materials - ICSAM 2003. **Anais...: Materials Science Forum**. Trans Tech Publications, 2004

SHERBY, O. D.; WADSWORTH, J. Superplasticity and superplastic forming processes. **Materials Science and Technology**, v. 1, n. November, 1985.

OBASI, G. C. et al. Effect of  $\beta$  grain growth on variant selection and texture memory effect during  $\alpha \rightarrow \beta \rightarrow \alpha$  phase transformation in Ti-6 Al-4 V. **Acta Materialia**, v. 60, n. 3, p. 1048–1058, 2012.

ODENBERGER, E.-L. et al. Thermo-mechanical sheet metal forming of aero engine components in Ti-6Al-4V - PART 1: Material characterization. **International Journal Material Forming**, 2012.

PAN, W. et al. A Sigmoidal Model for Superplastic Deformation. **Proceedings of the Institution of Mechanical Engineers, Part L: Journal of Materials: Design and Applications**, v. 219, n. 3, p. 149–162, 2005.

PEARSON, C. The viscous properties of extruded eutectic alloys of lead- tin and bismuth-tin. **Journal of the Institute of Metals**, v. 54, n. 1, p. 111–124, 1934.

PHAM, H.-T. **Manual superplastic forming simulation with ABAQUS 6 . 4-1**. Chung Hsing. Institute of Precision Engineering \*RIGID, 2007.

REVIL-BAUDARD, B. **Simulation du comportement mécanique des alliages de titane pour les procédés de mise en forme à froid**. 2010. p 247. Doctoral Thesis. Ecole nationale supérieure des Mines de Paris, Mécanique Numérique. Paris, 2010.

RHAIPU, S. The effect of microstructural gradients on superplastic forming of Ti-6Al-4V. **Journal of Materials Processing Technology**, v. 80–81, n. June 2000, p. 90–95, 1998.

RHAIPU, S. **The effect of microstructural gradients on superplastic forming of Ti-6Al-4V**. 2000. p 343. Doctoral Thesis. University of Birmingham, Birmingham , 2000.

ROSSERD, C. Characteristic of strain rate strength and superplastic forming. **Review of Metallurgy**, v. 63, 1966.

ROY, S.; SUWAS, S. The influence of temperature and strain rate on the deformation response and microstructural evolution during hot compression of a titanium alloy Ti-6Al-4V-0.1B. **Journal of Alloys and Compounds**, v. 548, p. 110–125, 2013.

RTI INTERNATIONAL METALS, I. C. **Titanium Alloy Guide**. . p. 43–74, 2013. Available in: [www.rmititanium.com](http://www.rmititanium.com)

SABLIK, M. J. et al. Modeling of sharp change in magnetic hysteresis behavior of electrical steel at small plastic deformation. **Journal of Applied Physics**, v. 97, n. 10, p. 10E518, 15 May 2005.

SEMIATIN, S. .; SEETHARAMAN, V.; WEISS, I. Flow behavior and globularization kinetics during hot working of Ti–6Al–4V with a colony alpha microstructure. **Materials Science and Engineering: A**, v. 263, p. 257–271, 1999.

SEMIATIN, S. L. et al. Plastic Flow and Microstructure Evolution during Low-Temperature Superplasticity of Ultrafine Ti-6Al-4V Sheet Material. **Metallurgical and Materials Transactions A**, v. 41, n. 2, p. 499–512, 2010.

SEMIATIN, S. L.; SARGENT, G. A. Constitutive Modeling of Low-Temperature Superplastic Flow of Ultrafine Ti-6Al-4V Sheet Material. **Key Engineering Materials**, v. 433, p. 235–240, 2010.

SESHACHARYULU, T. et al. Hot deformation mechanisms in ELI Grade Ti-6a1-4V. **Scripta Materialia**, v. 41, n. 3, p. 283–288, Jul. 1999.

SIEGERT, K.; WERLE, T. **Physical Mechanism of Superplasticity Physical Mechanism of Superplasticity**. Stuttgart, 1994.

SIENIAWSKI, J.; MOTYKA, M. Superplasticity in titanium alloys. **Journal of Achievements in Materials and Manufacturing Engineering**, v. 24, n. 1, p. 123–130, 2007.

THURAMALLA, N. V; DESHMUKH, P. V; KHRAISHEH, M. K. Multi-scale analysis of failure during superplastic deformation. **Materials Science Forum**, v. 447–448, p. 105–110, 2004.

TILEY, J. S. **Modeling of Microstructure Property Relationships in Ti-6Al-4V**. 2002. p 208. Doctoral Thesis. The Ohio State University, Ohio, 2002.

VAIRIS, A. et al. Applying Superplastic Forming Principles to Titanium Sheet Metal Forming Problems. **Material Science Forum**, v. 447, n. 12, p. 239–246, 2008.

VANDERHASTEN, M. **Ti-6Al-4V: Deformation map and modelisation of tensile behavior**. 2008. Doctoral Thesis. Katholieke Universiteit Leuven, 2008.

VANDERHASTEN, M.; RABET, L.; VERLINDEN, B. Ti-6Al-4V: Deformation map and modelisation of tensile behaviour. **Materials & Design.**, v. 29, n. 6, p. 1090–1098, 2008.

VELAY, V. et al. Behavior modeling and microstructural evolutions of Ti-6Al-4V alloy under hot forming conditions. **International Journal of Mechanical Sciences**, v. 108–109, p. 1–13, 2016.

VILANE, V. N. **Grain refinement in cast titanium 6-aluminium 4-vanadium by hydrogenation, deformation and recrystallisation**. 2012. p 143. Doctoral Thesis. University of Cape Town. 2012.

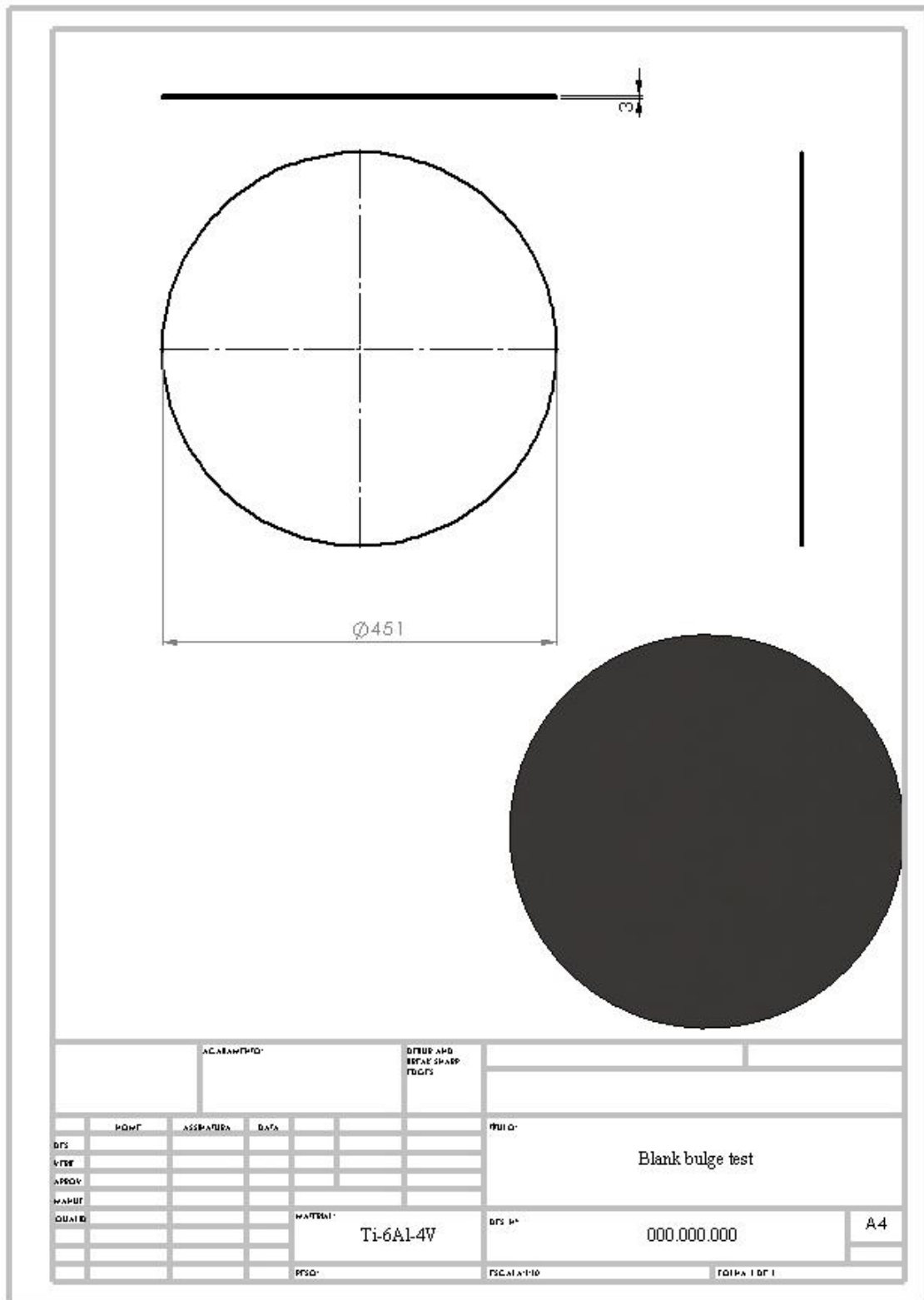
XING, H. Recent development in the mechanics of superplasticity and its applications. **Journal of Materials Processing Technology**, v. 151, p. 196–202, Jun. 2004.

YANG, L. et al. Unified constitutive modelling for two-phase lamellar titanium alloys at hot forming conditions. **Manufacturing Review**, v. 3, p. 14, 2016.

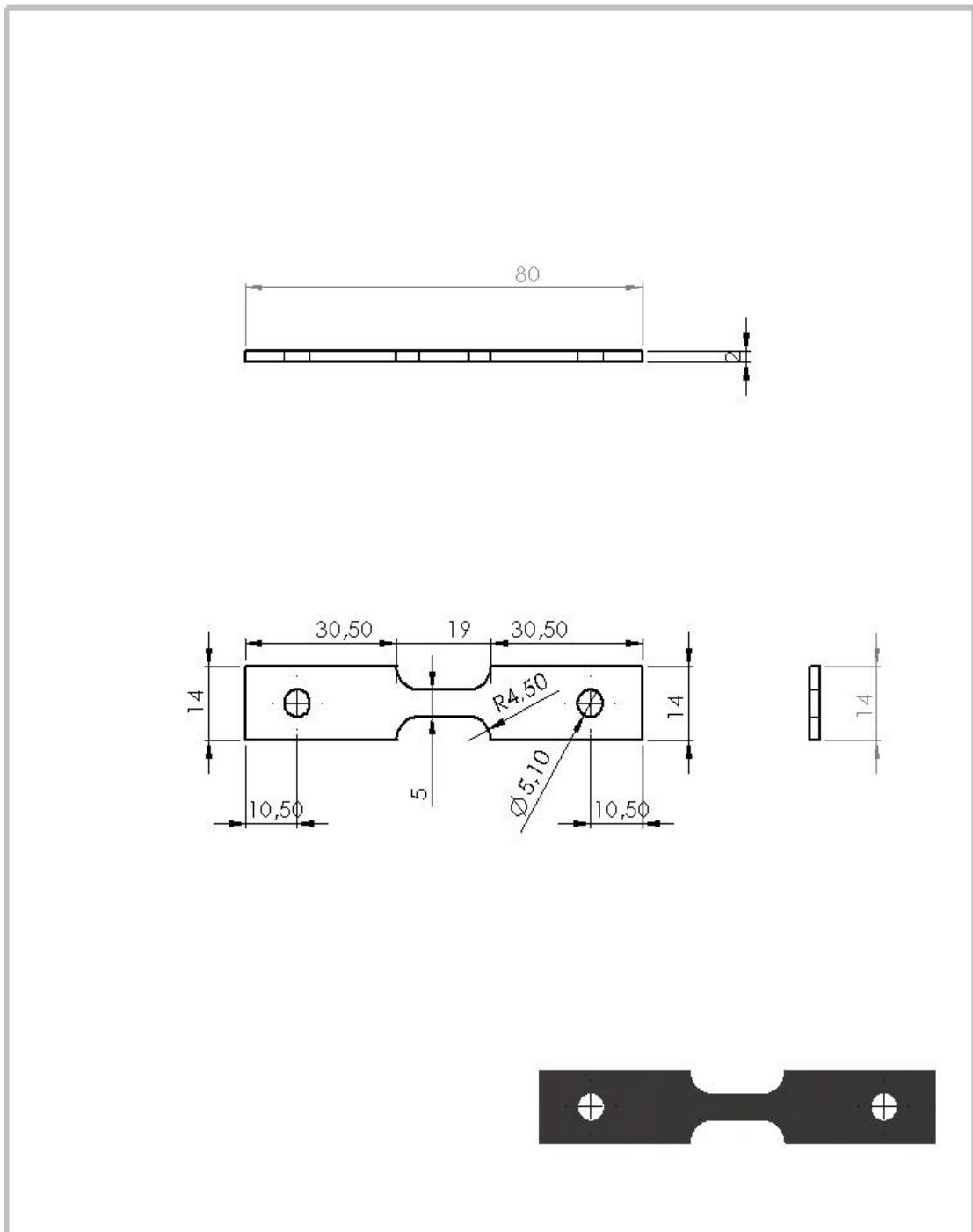
8. APPENDIX

APPENDICE A - Specimen types

A1 - Technical draw: Ti-6Al-4V Bulge test specimen

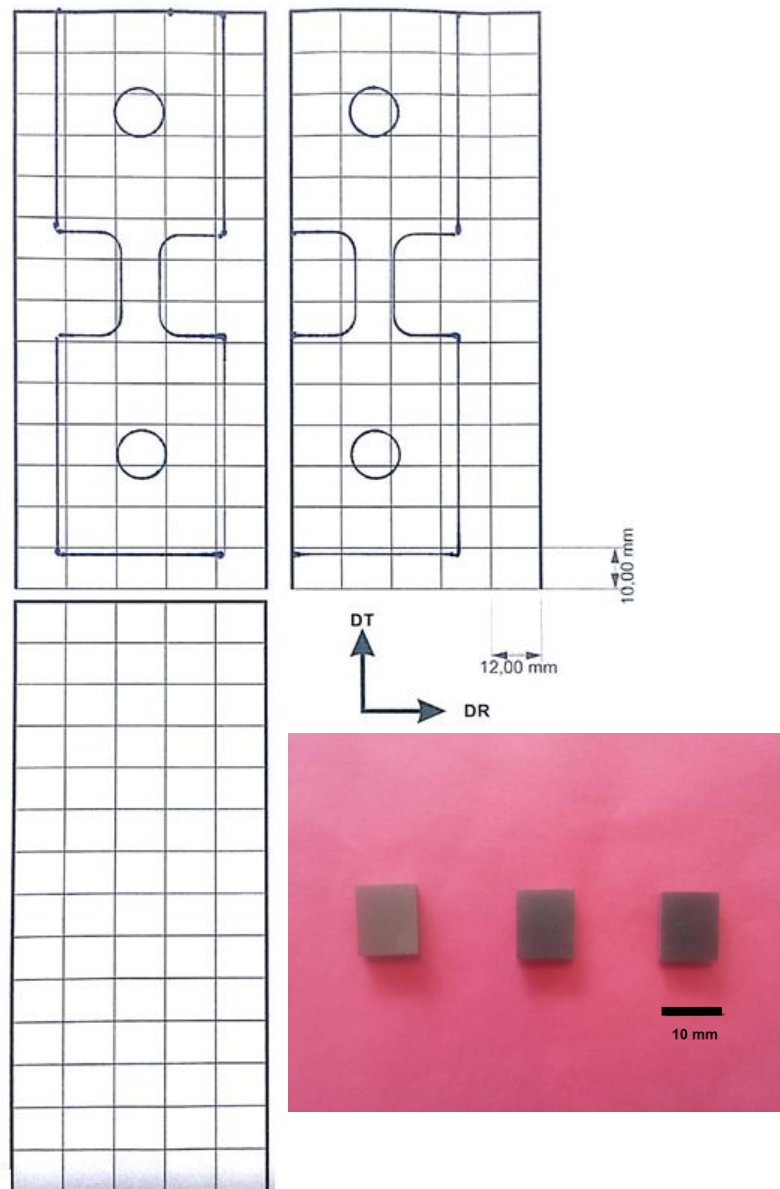


A2 – Technical draw thermo-simulator for Gleeble 3800 tensile test



SE NÃO ESPECIFICADO: DIMENSÕES EM MILÍMETROS ACABAM. SUPERFÍCIE: TOLERÂNCIAS: LINHA F: ANOTAÇÃO:		ACABAMENTO:		DEBUR AND BREA (SHARP EDGES)		NÃO MUDAR A ESCALA DO DESENHO		REVEÃO	
NOME		ASSINATURA		DATA		RUBRICADO			
DES.									
VERIF.									
APROV.									
MATERIAL									

## A3 - Schema for ageing test sample



In detail, the ageing test sample prepared

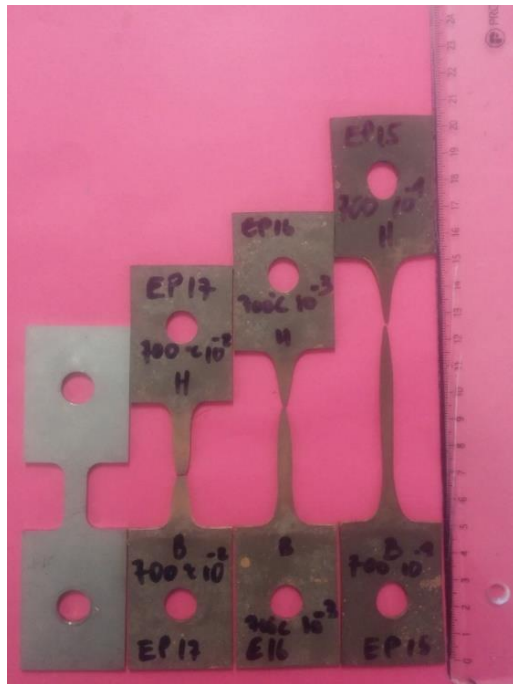
## APPENDIX B – Tensile tests

B1 Table of conditions of superplastic tested at servo hydraulic machine

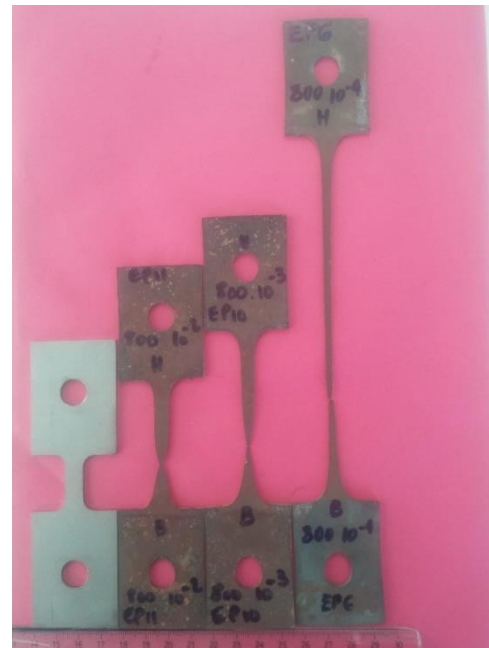
Strain rate	N° specimen	Surface	F <sub>máx</sub>	σ <sub>máx.</sub>	time of deformation
(s <sup>-1</sup> )		(mm <sup>2</sup> )	(N)	(MPa)	(hh:mm:ss)
10 <sup>-2</sup>	1	16.863	1.6448	97.5390	00:02:12
10 <sup>-3</sup>	3	16.9011	0.4307	25.4842	00:29:01
10 <sup>-4</sup>	5	17.2056	0.2547	14.8054	05:54:09
10 <sup>-2</sup>	11	17.1891	2.4022	140.6223	00:02:06
10 <sup>-3</sup>	10	16.8589	0.8777	52.0627	00:26:36
10 <sup>-4</sup>	6	17.1121	0.3800	22.4834	06:34:22
10 <sup>-2</sup>	8	16.9974	1.8216	107.1670	00:02:21
10 <sup>-3</sup>	7	16.8483	0.6434	38.3042	0:33:20
10 <sup>-4</sup>	9	17.0772	0.2983	17.4661	06:35:22
10 <sup>-2</sup>	14	17.028	1.3848	81.3266	00:02:16
10 <sup>-3</sup>	13	17.0856	0.4759	27.8514	00:33:20
10 <sup>-4</sup>	12	16.8328	0.2447	14.5371	05:56:20
10 <sup>-2</sup>	17	17.1084	4.9029	286.5782	00:01:40
10 <sup>-3</sup>	16	17.1039	2.6885	157.1864	00:23:12
10 <sup>-4</sup>	15	17.0024	1.2313	72.4192	05:07:26
10 <sup>-4</sup>	23	19.019	1.4122	74.2521	05:36:37
10 <sup>-4</sup>	24	17.0826	0.3291	19.2652	06:13:11
10 <sup>-4</sup>	25	18.9528	0.4101	21.6380	05:46:46
10 <sup>-4</sup>	26	18.9689	0.2658	14.0124	06:15:12
10 <sup>-4</sup>	27	20.7024	0.3422	16.5295	05:54:36
10 <sup>-3</sup>	28	17.76	0.6562	36.9482	00:33:20
10 <sup>-3</sup>	18	16.758	0.1702	10.1563	00:33:20
10 <sup>-3</sup>	21	17.172	0.1522	8.8633	00:33:20
10 <sup>-4</sup>	22	17.2368	0.1607	9.3231	06:19:22

## B2: Image of tensile test deformed specimen

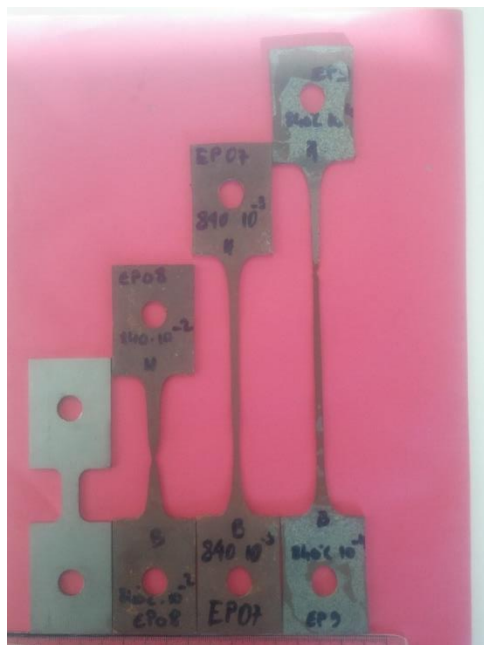
@700 °C



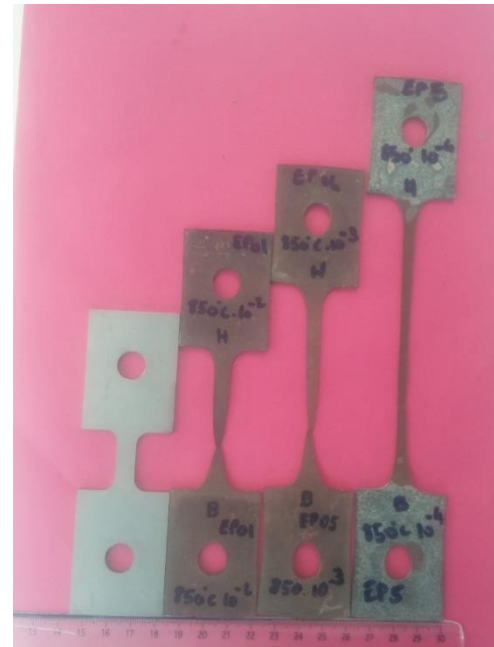
@800 °C



@840 °C

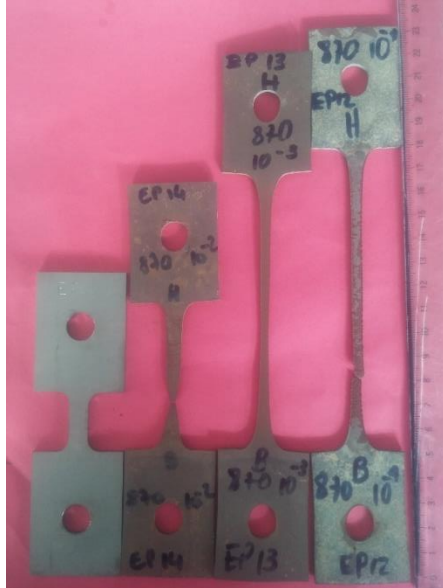


@850 °C



@870 °C

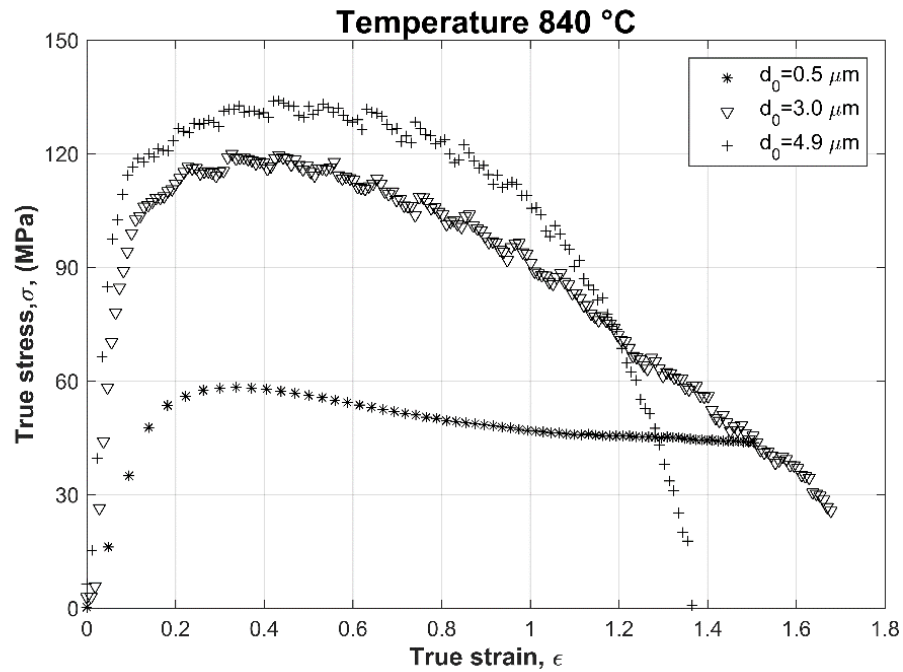
Mechanical test specimen after 950 °C at  $10^{-3}$  and  $10^{-4}$  s $^{-1}$



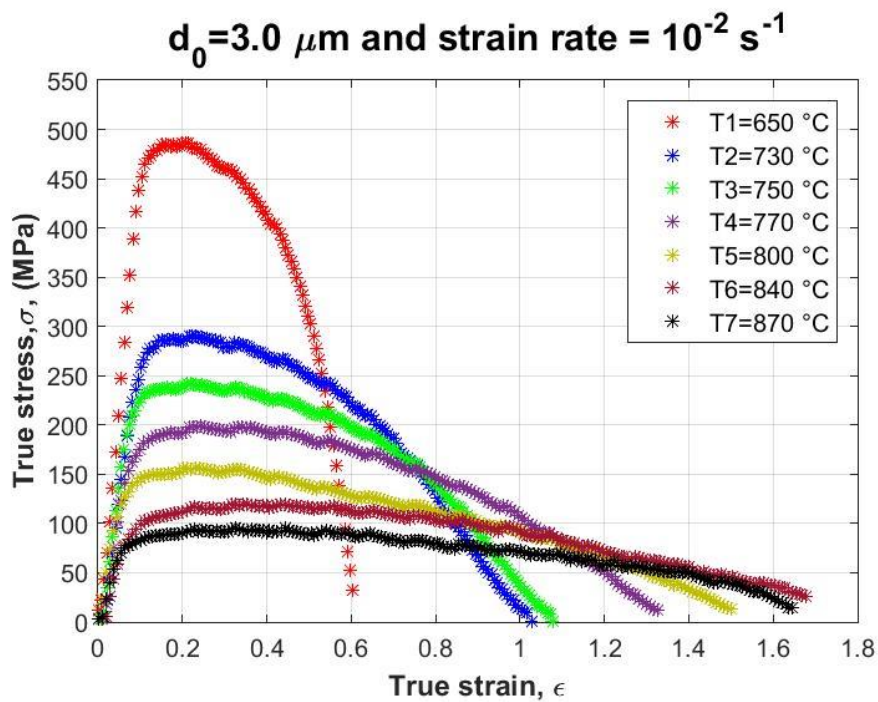
Tensile tests images of deformed specimens at temperature [700, 800, 840 and 850, 870 and 950] °C as indicated in the figure table

### B3: STRAIN-STRESS CURVES

True stress-true plastic strain curve of a Ti-6Al-4V flat specimen tested at 840°C with a strain rate of  $5 \cdot 10^{-2} \text{ s}^{-1}$ .

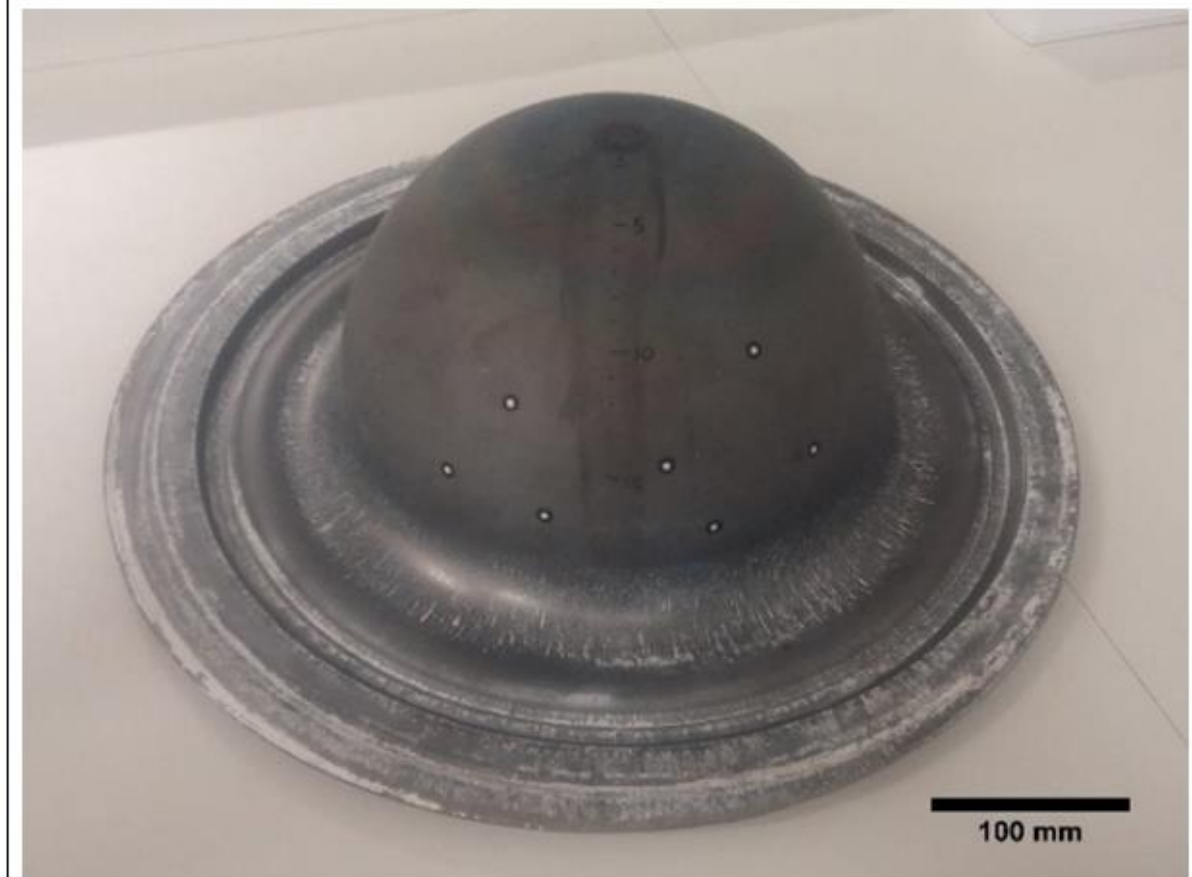
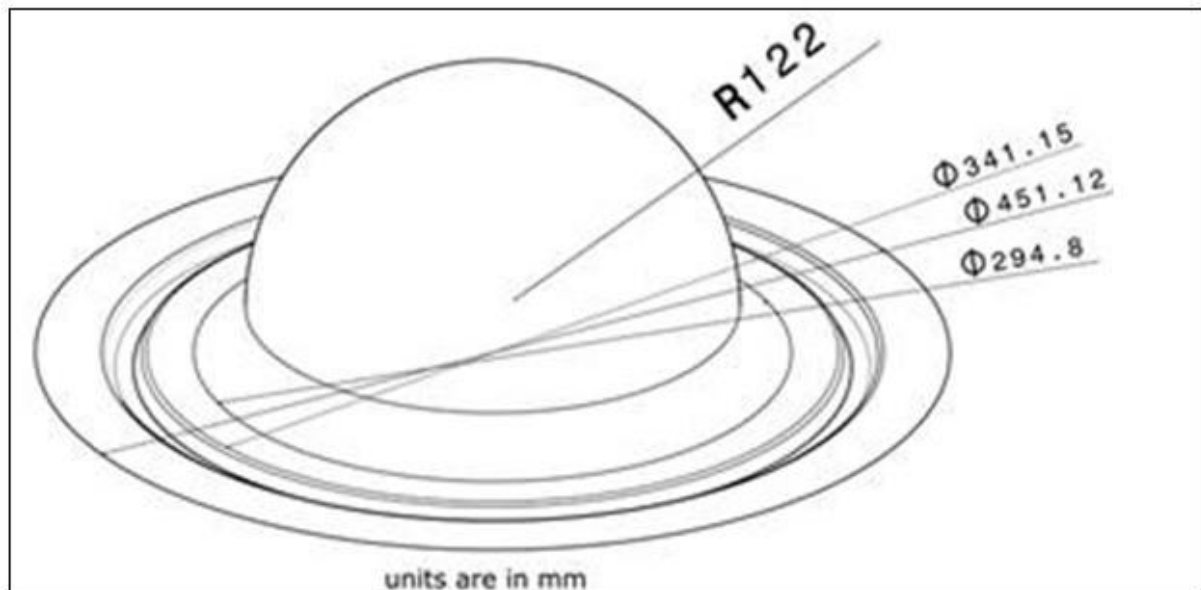


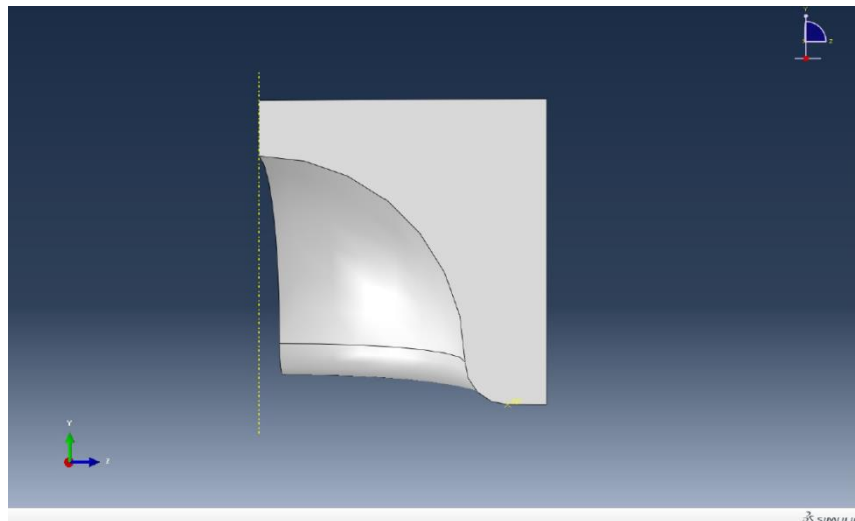
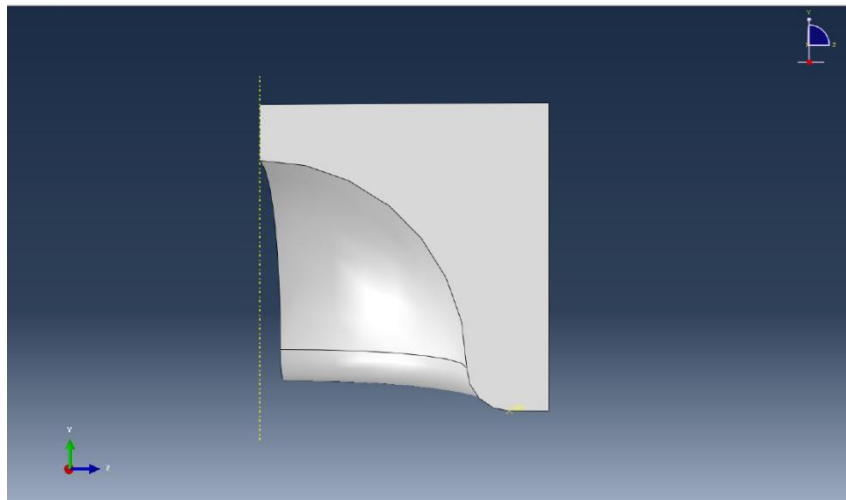
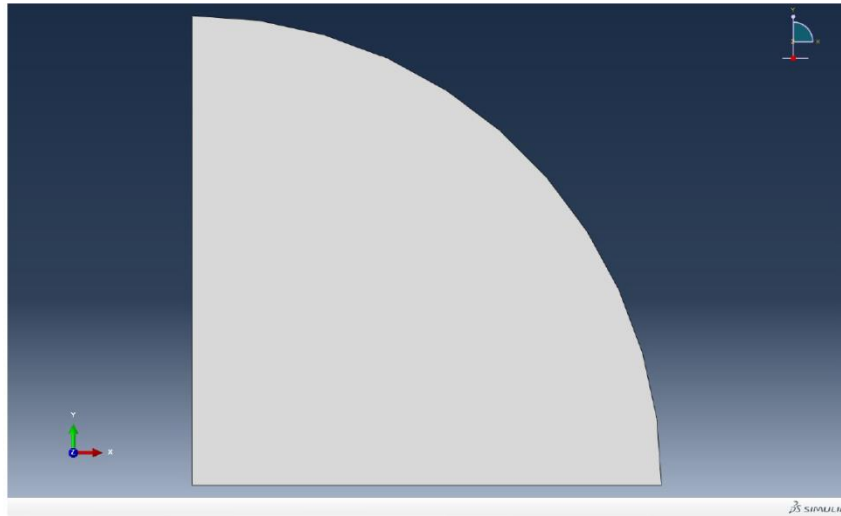
Mechanical behaviour at 840 °C and grain size 0.5; 3.0 and 4.9  $\mu\text{m}$



Influence of the test temperature

## APPENDIX A: BULGE DATA



**APPENDIX B: ABAQUS SIMULATE FORMING PARTS**

## **APPENDIX F: FINITE ELEMENT FORMULATION OF THE SHEET METAL FORMING PROBLEM**

ABAQUS (Deshmukh 2003; Wang 2007), a general purpose finite element program is used to carry out the computational analysis of SPF. ABAQUS includes direct, implicit time integration, using the Hilber-Hughes operator (the Newmark's method with controllable numerical damping). This implicit software is specifically chosen for the superplastic analysis since it enables a full static solution of deformation problem with convergence control and the time increment size can be defined within practical limits. Fully integrated quadrilateral membrane elements present in the ABAQUS element library are used to mesh the die and the sheet assembly model.

A user defined subroutine is used to model the superplastic material behaviour. It is based on a failure criterion, which considers strain hardening, grain size and void growth during superplastic forming. A macro present in ABAQUS is used to control the pressure at each time step to limit the maximum strain rate, during SPF, within a predefined optimum region.

### **8.1.1. IMPLICIT AND EXPLICIT ANALYSIS**

Implicit and Explicit solvers are two common numerical techniques currently used in FE simulation industry. From the physical point of view the kinetic energy plays an important role in selecting the type of FE technique to be used for the analysis. We can broadly classify the metal forming processes into two types.

- I. In quasi-static problem, the kinematic energy is insignificant of the total energy.

Superplastic forming falls into this category.

- II. In high strain rate phenomena, or purely dynamic processes, the kinetic energy is overwhelmingly dominant. This is the case of processes with a high energetic impact.

## Numerical Integration in time

The Equation (8-1) express the relation the global stiffness, mass and force matrices in a mechanical system:

$$\{F(t)\} = [K]\{d\} + [M]\{\ddot{d}\} \quad (8-1)$$

where  $[K]$ ,  $[M]$  and  $[F]$  are the, respectively. dare the nodal displacements and  $\ddot{d}$  are the nodal accelerations.

Upon discretization of the above equation with respect to time, we can determine the nodal displacements at different time increment for a given system. The general method used is direct integration. There are two classifications of direct integration: explicit and implicit. The common explicit and implicit methods are known as the central difference method (Deshmukh 2003) and Newmark's method respectively.

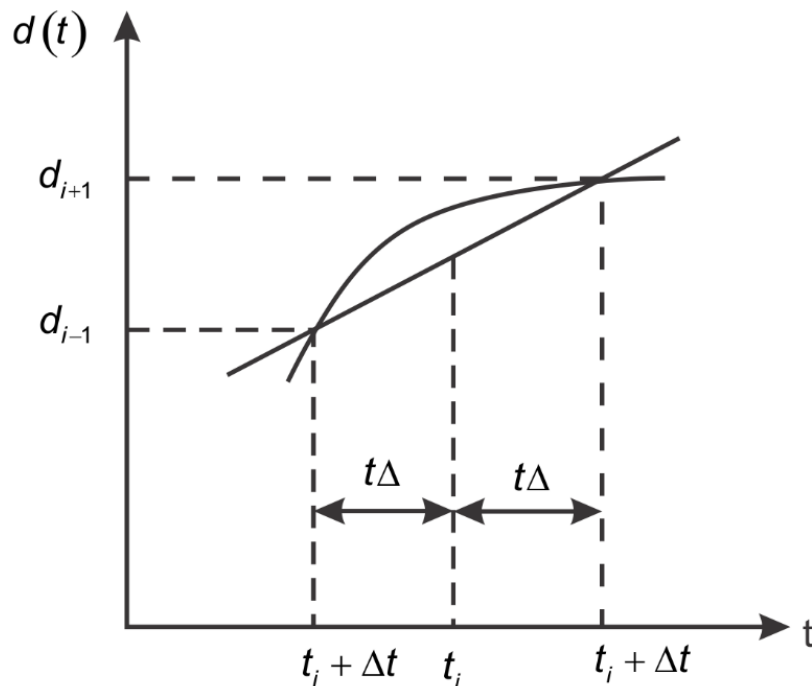


Figure 8-1 – Numerical integration

## Explicit Element Method

The central difference method is based on finite difference expression in time for velocity and acceleration at time  $t$  given by

$$\dot{d}_i = \frac{d_{i+1} - d_{i-1}}{2(\Delta t)} \quad (8-2)$$

$$\ddot{d}_i = \frac{d_{i+1} - 2d_i + d_{i-1}}{2(\Delta t)^2} \quad (8-3)$$

$$d_{i+1} = 2d_i - d_{i-1} + \ddot{d}_i (\Delta t)^2 \quad (8-4)$$

From Equation (8-1) we can express acceleration as

$$\ddot{d}_i = M^{-1}(F_i - Kd_i) \quad (8-5)$$

From Equations (8-4) and (8-5) we have

$$Md_{i+1} = (\Delta t)^2 F_i + [2M - (\Delta t)^2 K]d_i - Md_{i-1} \quad (8-6)$$

Using the displacement  $d_{i-1}$ , we can use the above equations to determine  $d_{i+1}$ ,  $\dot{d}_{i+1}$ ,  $\ddot{d}_{i+1}$ .

The major advantage of using this process is that the matrix inversion of the global mass matrix [M] is not required. However, this process is conditionally stable, i.e. the time step for the time integration is subjected to limitation via Equation (8-7).

$$\Delta t \leq 2 \left[ (1 + \xi^2)^{0.5} - \xi \right] / \omega_{\max} \quad (8-7)$$

where  $\omega_{\max}$  is the maximum eigen frequency of the system and  $\xi$  is the fraction of the critical damping of the highest mode.

Thus, to increase the time step by artificially increasing the punch speed or by artificially increasing the mass density. However, such attempts at improving the analysis efficiency result in an increase of inertial effects which affects the accuracy of the solution (Deshmukh 2003) .

### Implicit Finite Element Method

ABAQUS, implicit analysis software, used the Newmark's direct integration method. Newmark's equations are given by:

$$\dot{d}_{i+1} = \dot{d}_i + (\Delta t) \left[ (1 - \gamma) \ddot{d}_i + \gamma \ddot{d}_{i+1} \right] \quad (8-8)$$

$$d_{i+1} = d_i + (\Delta t) \dot{d}_i + (\Delta t)^2 \left[ \left( \frac{1}{2} - \beta \right) \ddot{d}_i + \beta \ddot{d}_{i+1} \right] \quad (8-9)$$

where  $\beta$  and  $\gamma$  are, parameters chosen by the user. By multiplying Equations 3.9 by mass matrix M and then substituting Equation (8-5) we obtain

$$K' d_{i+1} = F'_{i+1} \quad (8-10)$$

Where

$$K' = K + \frac{1}{\beta(\Delta t)^2} M \quad (8-11)$$

$$F_{i+1} = F_{i+1} + \frac{M}{\beta(\Delta t)^2} \left[ d_i + (\Delta t) \dot{d}_i + \left( \frac{1}{2} - \beta \right) (\Delta t)^2 \ddot{d}_i \right] \quad (8-12)$$

Using the above equations, we can determine the values of  $d_{i+1}$ ,  $\dot{d}_{i+1}$  and  $\ddot{d}_{i+1}$ . Due to the iterative nature of the solution procedure, a successful solution requires the satisfaction of convergence criterion at each step. Generally, the convergence speeds quite problem dependent and failure to converge results in premature termination of the analysis.

Thus, it can be seen that the dynamic explicit method is advantageous for analysis of sheet metal forming where the real time is just a few seconds. It has the characteristic of less memory requirement and greater computer efficiency since the need for consistent stiffness matrix is obviated. However, for process such as superplastic forming, this method reveals its inability to reduce the calculations time because of stability requirements on the size of the time step, thus requiring larger number of incremental steps. In addition, when rate sensitive materials are involved, accurate results are extremely difficult to obtain unless a large number of steps are used (DESHMUKH, 2003; THURAMALLA; DESHMUKH; KHRAISHEH, 2004; VAIRIS et al., 2008; WANG, 2007).

### 8.1.2. SURFACE MODELING AND MESH GENERATION

SPF involves modelling complex shaped structural components. It is essential to accurately define an intricate shaped die surface and generate a quality finite element mesh over it, into which the flat sheet metal is deformed.

In most cases die surfaces are often topographically irregular and the regular assembly of rectangular patches for modelling these surfaces leaves some non-four-sided-holes. Using a consistent expression to represent the non-four-sided surface areas, and

generating a quality FE mesh over the regions, are crucial for carrying out FE simulations of SPF process.

Taking advantage of the symmetry only a quarter of the assembly is considered for the analysis. Usually different types of symmetry may exist in an assembly. These include reflective or mirror, skew, axial and cyclic.

Symmetry means correspondence in size, shape, and position of loads; material properties; and boundary conditions that are opposite sides of a dividing line or plane. The use of symmetry allows us to consider a reduced problem instead of the actual problem and the computational time required for the analysis is substantially decreased. One important aspect to be considered during symmetric analysis is to model more than quarter of the die surface. This avoids the elements and nodes on the deformable sheet from sliding off the die.

### **Superplastic Modelling sheet Ti-6Al-4V alloy**

The superplastic sheet is meshed using in this work is quadrilateral membrane elements, of the type 894 S4R present in the ABAQUS element library<sup>3</sup>. S4R for most analyses the standard large-strain shell elements are appropriate in a term used for 3-Dimensional, 4 node membrane elements. S4R is a robust, general-purpose element that is suitable for a wide range of applications.

Computer simulations of three-dimensional superplastic sheet forming process can be carried out by the finite element method with a membrane element or a shell element. A membrane element is regarded as preferable rather than a shell element because of the computing efficiency and the easy contact treatment. Membrane elements are sheets in space that carry membrane force but do not have any bending or transverse shear stiffness, so the only nonzero stress component in the membrane are those components parallel to the middle surface of the membrane: the membrane is in a state of plane stress.

---

<sup>3</sup><https://www.sharcnet.ca/Software/Abaqus/6.14.2/v6.14/books/bmk/default.htm?startat=ch02s03ach148.html>

### Conventional shell element

- Uniformly reduced integration to avoid shear and membrane locking.
- The element has several hourglass modes that may propagate over the mesh.
- Converges to shear flexible theory for thick shells and classical theory for thin shells.

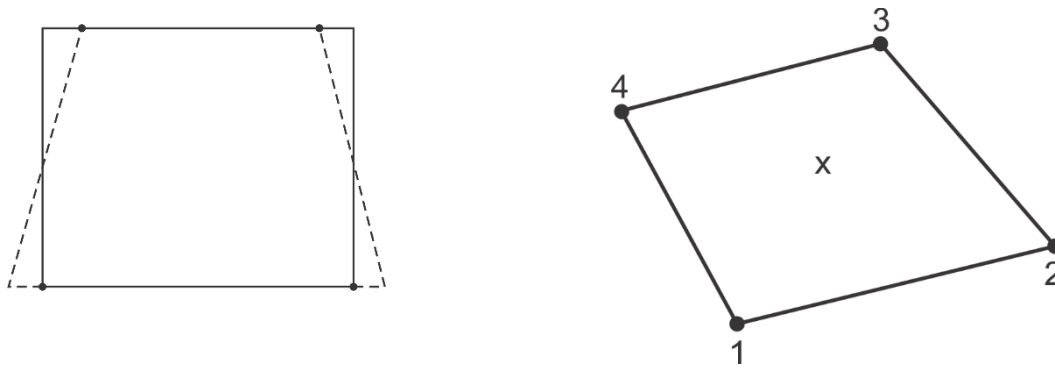


Figure 8-2 – Type shell membrane S4R nodes reduced integration element

### The die surfaces

To obtain optimum and reliable convergence, it is essential that the rigid surface representation is smooth. ABAQUS allows for re-constructing complex shaped 3D rigid surface with Bezier triangular patches based on triangular elements generated over the surface. The number of patches required to define the die surface can be reduced by specifying the normal at every vortex point of the mesh.

An extended version of classical isotropic Coulomb friction model provided in ABAQUS is used during the present SPF analysis. ABAQUS defines contact between two bodies in terms of two surfaces that may interact; these surfaces are called a “contact pair”. For each node on the first surface (the “slave” surface) ABAQUS attempts to find the closest point on the second surface (the “master” surface) of the contact pair where the master surface’s normal passes through the node on the slave surface (Deshmukh 2003). If during iteration a slave node is found to have penetrated the master surface by more than a specific distance, ABAQUS abandons the increment and tries again with a smaller increment size. This distance is known as HCRIT. The default value of HCRIT is the radius of the sphere that circumscribes a characteristic surface element face.

### 8.1.3. Loading and Boundary conditions

Superplasticity is exhibited by materials only in a narrow strain rate range with an optimum value unique to each material. This factor makes it essential to determine the pressure loading history to maintain the maximum strain rate near the optimum value throughout the whole forming process.

This control formulation is implemented in ABAQUS by means of solution-dependent amplitude. The applied pressure  $P$  is to be varied throughout the simulation to maintain the strain rate ( $\dot{\epsilon}$ ) a predetermined value  $\dot{\epsilon}_{op}$ . During an increment, ABAQUS calculates  $\gamma_{max}$ , the ratio of the equivalent strain rate to the target optimal strain rate for any integration point in a specified element set. This element set is selected on the basis of the control scheme used i.e. constant strain rate control in the free forming region, constant strain rate control in the die entry region, maximum variable strain rate control or strain rate gradient control.

$$\gamma_{max} = \frac{\dot{\epsilon}}{\dot{\epsilon}_{max}} \quad (8-13)$$

### WRITING USER SUBROUTINES WITH ABAQUS

ABAQUS provides users with an array of user subroutines that allows them to adapt ABAQUS with some analysis requirements. The constitutive equations discussed in Chapter 5 are implemented into the FE solver ABAQUS through user defined subroutine CREEP.

Figure 8-3 shows the basic flow of data and actions from the start of an ABAQUS analysis to the end of a step. From CREEP subroutine was adapted to define time dependent viscoplastic material behaviour. The user subroutine must define the increment of inelastic strain, as a function of stress and the time increment.

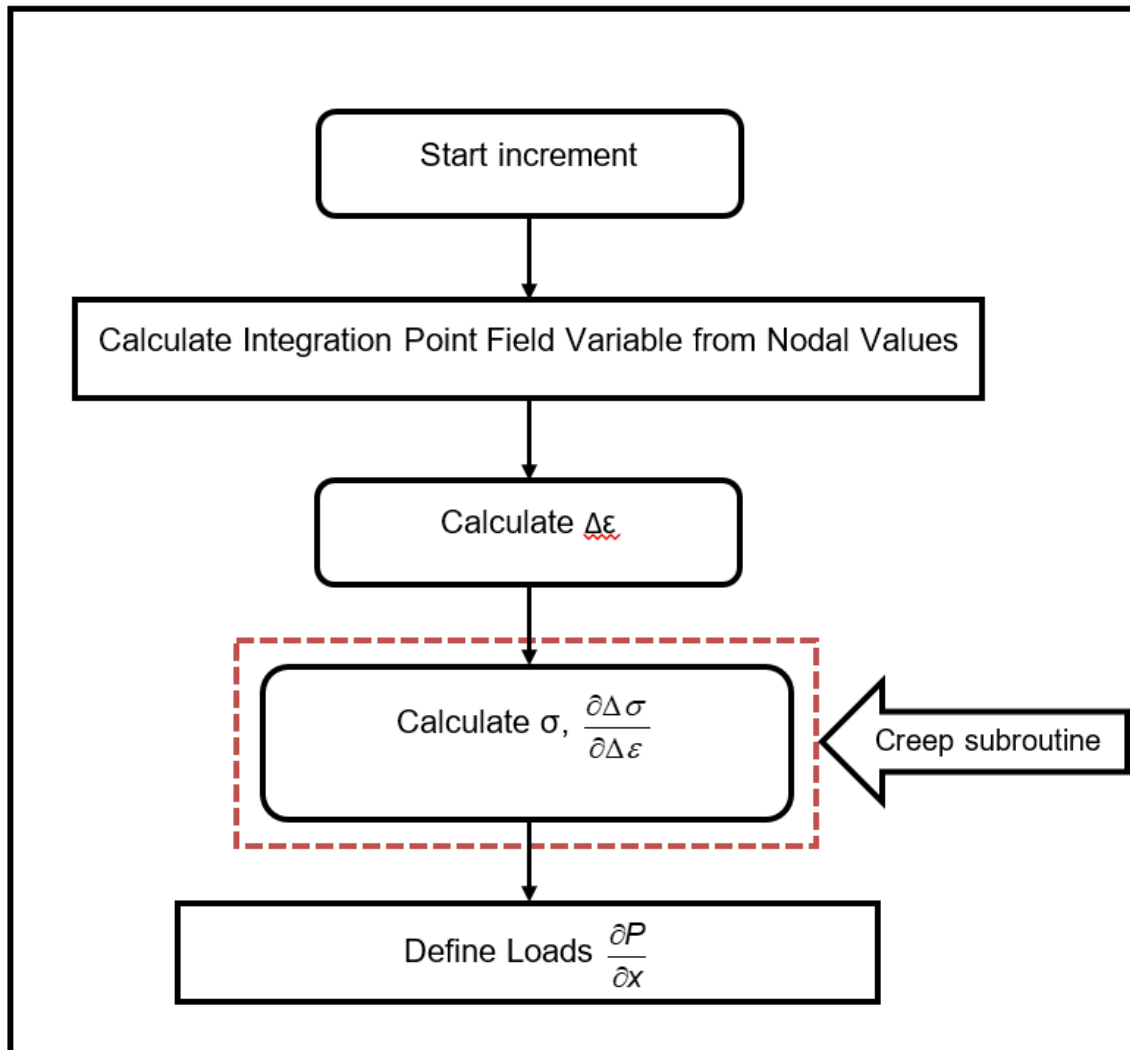


Figure 8-3 - Detailed flow of ABAQUS/Standard (PHAM, 2007).

Other variables such as grain growth and cavitation are defined as solution dependent state variables (SDV). SDV's are values that can be defined to evolve with the solution of the analysis. The SDV's are initialized using the SDVINI subroutine and its evolution is calculated within the CREEP subroutine. The interface to user subroutine CREEP is presented in the Figure 8-4.

```

SUBROUTINE CREEP (DECRA, DESWA, STATEV, SERD, EC, ESW, P, QTILD,
  1 TEMP, DTEMP, PREDEF, DPRED, TIME, DTIME, CMNAME, LEXIMP, LEND,
  2 COORDS, NSTATV, NOEL, NPT, LAYER, KSPT, KSTEP, KINC)
C
  INCLUDE 'ABA_PARAM.INC'
C
  CHARACTER*80 CMNAME
C
  DIMENSION DECRA (5), DESWA (5), STATEV (*), PREDEF (*), DPRED (*),
  1 TIME (2), COORDS (*), EC (2), ESW (2)
...
user code to define stress strain relationship
...
  RETURN
  END

```

Figure 8-4 - The interface to user subroutine CREEP

The variables to be defined are:

- DECRA (1): Deviatoric creep strain increment.
- DESWA (1): Volumetric strain increment.
- DECRA (5):  $\frac{\partial \Delta \bar{\epsilon}}{\partial \Delta \bar{\sigma}}$

The variables passed in for information are:

- QTILD: Effective stress
- TIME (1): Value of step time at the end of the increment.
- TIME (2): Value of total time at the end of the increment.
- DTIME: Time Increment.
- NOEL: Element number.
- NPT: Integration point number.
- KSTEP: Step number.
- KINC: Increment number